Moisture and Temperature Effects on the Dielectric Spectrum of Transformer Insulation Materials

by

Yanqing Du

B.S.E.E., Northwestern Polytechnical University, Xi'an, China (1993)
M.S.E.E., Northwestern Polytechnical University, Xi'an, China (1994)

Submitted to the Department of Electrical Engineering and Computer Science
in Partial Fulfillment of the Requirements for the Degrees of

Master of Science in Electrical Engineering
and
Electrical Engineer

at the

Massachusetts Institute of Technology
February 1999

© 1999 Massachusetts Institute of Technology
All rights reserved

Signature of Author .....
Department of Electrical Engineering and Computer Science
January 21, 1999

Certified by .....
Markus Zahn
Professor of Electrical Engineering
Thesis Supervisor

Certified by .....
Bernard C. Lesieutre
Associate Professor of Electrical Engineering
Thesis Co-Supervisor

Accepted by .....
Arthur C. Smith
Chairman, Committee on Graduate Students
Department of Electrical Engineering and Computer Science

MASSACHUSETTS INSTITUTE OF TECHNOLOGY
MAR 0 5 1999
LIBRARIES
ARCHIVES

To my parents:

Du Zhonghai

and

Ye Lian'e

Moisture and Temperature Effects on the Dielectric Spectrum of Transformer Insulation Materials

by
Yanqing Du

Submitted to the Department of Electrical Engineering and Computer Science on January 21, 1999 in partial fulfillment of the requirements for the Degrees of Master of Science and Electrical Engineer.

Abstract

The presence of moisture in a transformer deteriorates the transformer insulation by decreasing its electrical, mechanical, and thermal strength. Therefore it is of great importance to monitor the moisture condition in both liquid and solid insulation to assure transformer performance. There are commercially available sensors to measure the moisture in oil. When the transformer system is in equilibrium, existing moisture partitioning curves for oil-paper system can be used to find the moisture in paper from the oil measurement. A comprehensive study of the moisture equilibrium curves are given for an overview of the classic curves and their history, and providing useful information on the relationships among them and their validity. Solubility tests for differently conditioned oil are performed. Results show the solubility of moisture in oil increases significantly only in severely aged transformer oil.

When the system is not in equilibrium, the moisture curves are not applicable and the three-wavelength interdigital dielectrometry sensor developed at the MIT Laboratory for Electromagnetic and Electronic Systems is a unique way to measure the spatial profile of the moisture distribution in transformer pressboard. Preliminary measurements of oil and oil-impregnated pressboard are given in this thesis. A joint research group effort led to development of an improved design of the three-wavelength sensor which reduces the problems associated with the previous design and simplifies the inversion algorithm to convert the electrical signal to dielectric properties. The thesis focuses on the design and implementation of experimental studies based on interdigital dielectrometry using the new three-wavelength sensor.

As a first step to relate measurable dielectric properties to absorbed moisture, the moisture and temperature effects on the dielectric spectrum of oil-free pressboard are measured using a parallel-plate geometry sensor for nine moisture levels and five temperature levels. A dielectric model for biological tissue is adopted here for cellulose structured pressboard. A universal curve is found relating dielectric properties to moisture concentration and temperature by fitting the data to the model. Preliminary measurements of oil-impregnated pressboard show similar characteristics.

The moisture diffusion process of oil-free transformer pressboard is monitored using the new interdigital dielectrometry three-wavelength sensor in a specially constructed

bench-top apparatus. Experiments are performed for five different temperatures at various moisture levels. The time evolution of the moisture spatial profile in transformer pressboard is estimated non-destructively. Experimental results have a good agreement with theoretical analysis on the effects of pressboard thickness and temperature on the diffusion process.

The diffusion coefficient for oil-free pressboard as a function of temperature and moisture concentration is estimated and compared with literature values. Numerical methods of solving the diffusion equation are developed.

Thesis Supervisor: Markus Zahn
Title: Professor of Electrical Engineering

Thesis Co-Supervisor: Bernard C. Lesieutre
Title: Associate Professor of Electrical Engineering

Acknowledgments

It has been a great joy and privilege to have Professor Markus Zahn as my primary research advisor. His insight and love for research have been a great inspiration to me. His encouragement has meant much to me, especially during those hard times at MIT.

I am grateful to my co-supervisor, Professor Bernard C. Lesieutre, who has made important contributions to the project, especially in the modeling and numerical parts.

My colleagues at the MIT High Voltage Research Lab are a wonderful group of people who are more than extra hands for the experiments: Tza-Jing Gung, Robert Lyons, Afsin Ustundag, and Julio Castrillon. Darrell Schlicker deserves special thanks for being always there to help me and share with me his great ideas without any reservation, without which my path to completion would be much longer and difficult. I thank Alex Mamishev for his constructive criticism of my technical approach which greatly stimulated me to strive for perfection. Yanko Sheiretov and Dr. Philip von Guggenberg provided much help at the early stage of the research.

The experiments in Chapter 4 were done by undergraduate students, Madhu Sarda and Noemi Altamirano with my supervision and participation, as a part of their Undergraduate Research Opportunities Program and Advanced Undergraduate Projects at MIT. I also thank visiting professor Seong-hwa Kang from Korea for his contributions.

I want to thank all the supporting staff at the Laboratory of Electromagnetic and Electronic Systems, in particular Wayne Ryan who made all the tough heavy experimental efforts possible. I would like to thank the departmental graduate administrative officers, in particular, Peggy Carney and Marilyn Pierce, for their encouragement and support toward my graduate study at MIT.

I want to thank the following scientists for valuable discussions, inputs, and document and material supply: Dr. T. V. Oommen from ABB-ETI, Paul Griffin from Doble Engineering, Thomas Prevost from EHV-Weidmann, and Dr. Giuessepie Urbani from Haefely Trench. I would like to thank my academic advisor Professor Jin Au Kong for his encouragement and support. Thanks to my previous advisors in China, Professors Junfeng Ma, Lao Ji, and Xiaobin Zhang who built my foundations for research and prepared my way to the US.

The research projects covered in this thesis were mainly supported by the Electric Power Research Institute, grant number WO 8619-01, managed by Mr. Stan Lindgren, and the National Science Foundation, grant no. ECS-9523128. My first year study at MIT was supported by a Wang Tiwu Fellowship sponsored by the late Mr. Wang Tiwu. I thank him for his generosity and vision to support education. I am also thankful for the financial support from the American Public Power Association through the Demonstration of Energy-Efficient Developments Scholarships.

I want to thank my friends in the MIT Chinese Bible Study Group: Paul & Betty, Guangyu & Weiran, Leslie, Jeff, and many others. I thank Haiyan & Jiyong, Yinan & Pei, and Yunfei for their sustaining care and help to me, for being there when I need them. My thanks also go to my host family, Alberta and Roger Lipson, for the wonderful time they spent with me and the moral support they gave to me.

I am deeply grateful to Yanwu for all the unforgettable teaching, support, and love.

I am blessed with the persevering and sacrificial love of my family, my parents Du Zhonghai and Ye Lian'e, and my sister Qian, who made this all worthwhile. This thesis is dedicated to them!

Contents

List of Figures

List of Tables

Chapter 1

Introduction

1.1 Background of Thesis

This thesis work is a continuing research on interdigital dielectrometry and its application to measurements of the dynamics of moisture diffusion in transformer insulation materials; extending previous studies by degree candidates at the MIT Laboratory for Electromagnetic and Electronic Systems [1–3].

According to the concepts of frequency-wavenumber dielectrometry, commonly denoted as "$\omega - k$" dielectrometry, application of a spatially periodic potential with fundamental wavelength $\lambda = 2\pi/k$ and angular frequency $\omega = 2\pi f$ to the surface of a test dielectric generates an electric field which penetrates into the volume of the test material to a depth proportional to λ [1]. Consequently, the conduction and displacement currents, which flow into the sensing electrodes, depend on the dielectric properties of the sample.

The measured dielectric properties can be directly related to other physical properties of the material, such as moisture content and temperature, by a calibrated mapping. This thesis focuses on the application of "$\omega - k$" dielectrometry for monitoring the moisture content and spatial profile in transformer insulation.

Moisture dynamics between oil and transformer pressboard as a function of temperature is very important in power transformer operation. For example, if the tempera-

ture were to drop too quickly before the moisture in the oil could diffuse into pressboard, oil moisture would exceed the saturation value at this temperature, resulting in free water in the oil. Such free water in the high voltage region of the transformer could result in catastrophic electric breakdown and transformer failure. Another transformer failure mode dependent on moisture dynamics is flow electrification, which often arises when a transformer that has been out of service is being recommissioned. A plausible scenario is that as the transformer heats up, moisture is driven out of the pressboard insulation into the oil. The moisture first comes from near the pressboard interface, leaving a very dry interface that is also highly insulating. Any accumulating surface charge has no leakage and thus the surface charge density can increase until spark tracking discharges occur. These sparks cause gas formation, which can rise into the high electric field region causing a high-energy discharge that causes transformer failure. If failure does not occur during the early times of the recommissioning process, the moisture deeper in the pressboard diffuses to the surface reaching equilibrium with the oil moisture. The moisture diffusion time can easily be a few weeks, but once there is no longer an interfacial dry zone, there is a leakage path for interfacial surface charge so that the surface charge density cannot rise to electric field strengths beyond the breakdown strength of oil and pressboard. Thus, once the transformer is in moisture equilibrium, this flow electrification hazard is minimized. A typical pressboard surface tracking discharge pattern from a failed transformer is shown in Figure 1.1.

1.2 Scope of Thesis

The main objectives of this thesis research are:

1. Design and perform experiments in a bench-top apparatus using a three-wavelength interdigital dielectrometry sensor; and to improve the hardware design including sensor, experimental setup, feed-through for the sensor signal, and electronics for the interface circuitry.

2. Understand the physics of moisture partitioning in air-paper-oil systems and

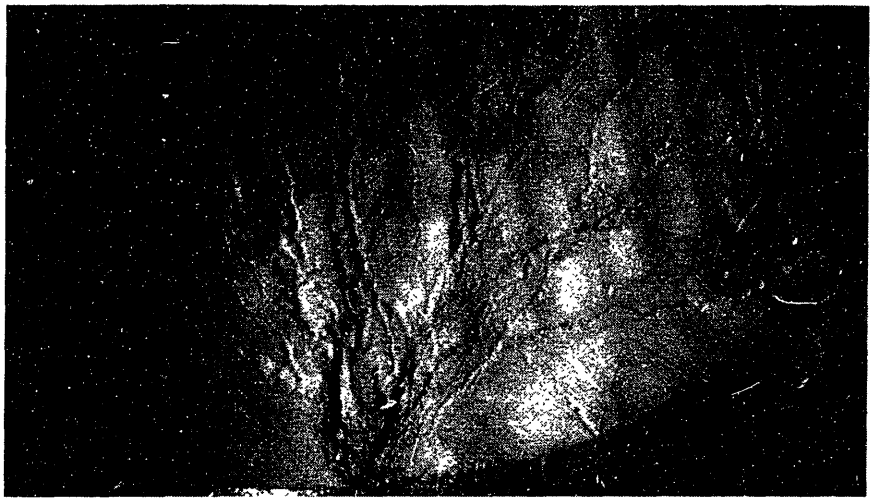

Figure 1.1: A typical surface tracking discharge pattern on pressboard due to flow electrification in a failed transformer.

survey available methods for transformer moisture monitoring.

3. Perform moisture diffusion measurements in a bench-top apparatus with the improved sensor design at various temperature and moisture levels.

4. Experimentally determine the correlation between moisture and temperature and complex permittivity in tested materials.

5. Study the mathematics of nonlinear diffusion processes, and analyze the measured data from the moisture diffusion process.

Chapter 2

Theoretical Background

2.1 Interdigital Dielectrometry

The generic schematic of an interdigital dielectrometry sensor is shown in Figure 2.1. This electroquasistatic system has an electric scalar potential Φ obeying Laplace's equation. Neglecting variations in the y direction, the solution for each wavelength can be written as an infinite series of sinusoidal Fourier modes of fundamental spatial wavelength λ in the x direction that decays exponentially in the z direction:

$$\Phi(x,z) = \sum_{n=0}^{\infty} \Phi_n e^{-k_n z}(A_n \sin k_n x + B_n \cos k_n x), \tag{2.1}$$

where $k_n = 2\pi n/\lambda$ is the wavenumber of each spatial mode. As extensively studied in [1, 3], the electric field distribution can be solved by defining a complex surface capacitance density $\hat{C}_n$, which relates $\varepsilon^* \hat{E}_{zn}$ at a planar surface $z = constant$ to the potential $\hat{\Phi}_n$ at that surface for every Fourier mode n as:

$$\hat{C}_n = \frac{\varepsilon^* \hat{E}_{zn}}{\hat{\Phi}_n} \tag{2.2}$$

where the complex permittivity ε^* in 2.2 is defined as

$$\varepsilon^* = \varepsilon - j\frac{\sigma}{\omega} \tag{2.3}$$

where ε is the real part of dielectric permittivity, and σ is the conductivity of the media. Knowing $\hat{C}_n$ at the electrode surface will let us calculate the terminal currents due to

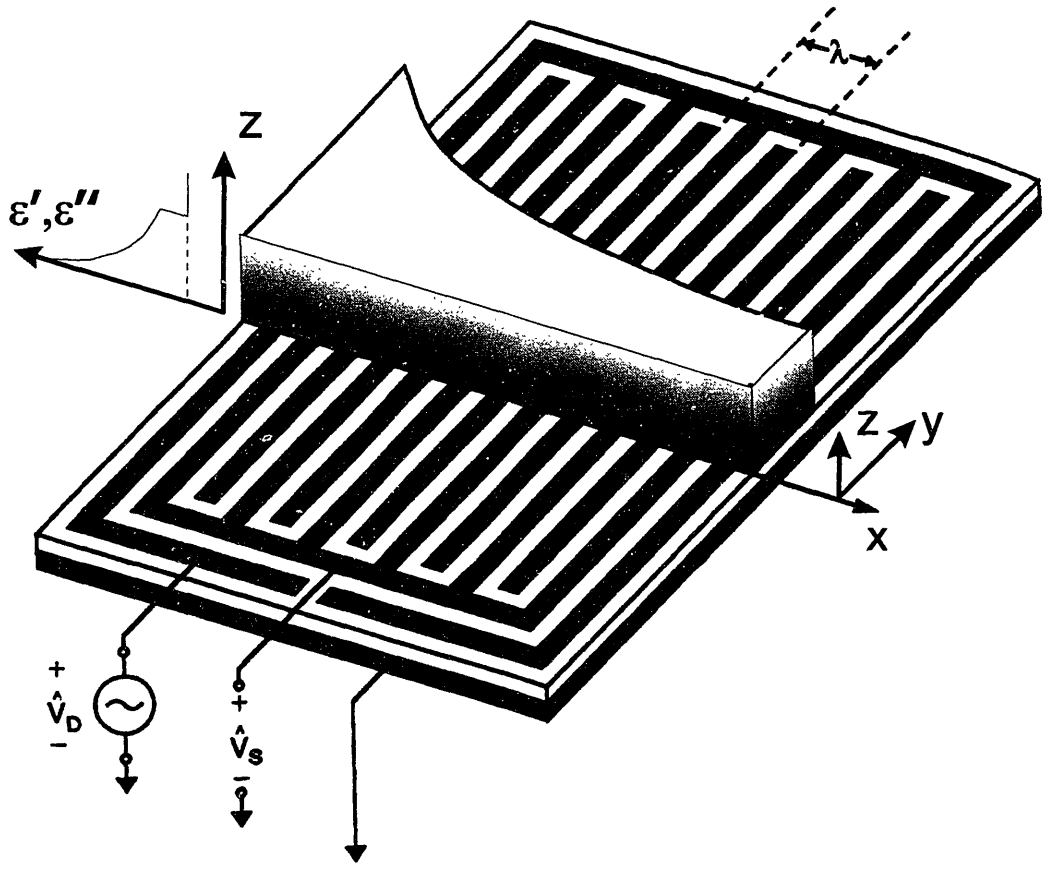

Figure 2.1: Imposed $\omega - k$ interdigital dielectrometry [4].

the sum of conduction and displacement currents from the potential distribution at that surface, which is practically equivalent to forward-solving (2.1).

For heterogeneous media, spatial profiles of dielectric properties can be determined using multiple-wavelength sensors with each wavelength having a different penetration depth into the dielectric in contact with the sensor. Equation 2.1 shows that the electric field decays away in the z direction proportional to the spatial wavelength λ, i.e. the longer the wavelength, the farther the field can penetrate into the material, and the farther the dielectric properties can be measured. This concept is the key ingredient of this profiling technology.

2.2 Moisture Measurement for Transformer Insulation

The presence of moisture in transformer insulation directly affects the system performance, so it is desirable to monitor its moisture content. For the oil, there are commercially available sensors to measure the moisture directly, and in equilibrium, the moisture content in the pressboard can be obtained using the partitioning curves between paper and oil. Those curves have been widely used by many utilities and transformer and test equipment manufacturers, and a thorough study on this topic is helpful for people to use this tool correctly and effectively.

For solids there are no commercially available instruments to continuously monitor the moisture distribution under non-equilibrium conditions. The multiple-wavelength interdigital dielectrometry sensor developed at the Laboratory for Electromagnetic and Electronic Systems, Massachusetts Institute of Technology is a unique way to monitor the moisture profile in transformer board in real time.

The sensor measures the change of the dielectric properties during the moisture diffusion process and by a calibrated mapping that relates the dielectric properties to the moisture content, the spatial profile of moisture can be resolved using an inverse algorithm.

Chapter 3

Moisture Equilibrium in Transformer Oil-Paper Systems

3.1 Introduction

The presence of moisture in transformers deteriorates transformer solid and liquid insulation by decreasing both the electrical and mechanical strength. In general, the mechanical life of pressboard insulation is reduced by half for each doubling in water content [5]; the rate of thermal deterioration of the paper is proportional to its water content [6]. Electrical discharges can occur in a high voltage region due to a disturbance of the moisture equilibrium causing a low partial discharge inception voltage and higher partial discharge intensity [7]. The migration of a small amount of moisture has been associated with flow electrification at paper/oil interfaces and is presumed to be due to charge accumulation on highly insulating interfacial dry zones where moisture has been desorbed [8,9]. Water in mineral oil transformers also increases the risk of bubble formation when desorption of water from the cellulose increases the local concentration of gases in the oil [10]. The importance of monitoring the presence of moisture in paper and oil systems has been recognized since the 1920's. Therefore, it is important to monitor moisture content in transformer solid and liquid insulation.

3.2 Off-line Methods to Measure Moisture in Transformer Insulation

There are two types of off-line methods: the Karl Fisher reaction method and the pressure gauge method.

The standard test method for measuring water in transformer oil is the ASTM D 1533 test known as the Karl Fischer reaction test. It is based on the reaction of halogens with water in the presence of anhydrous sulphur dioxide. It is widely used because of its high selectivity and sensitivity. There are commercial instruments such as the Mitsubishi Moisture Meter to accomplish the Karl Fischer titration automatically. With these instruments, an oil sample can be directly injected into the reaction unit and the moisture content will be given at the end of the reaction. In the case that the liquid samples contain interfering substances reacting with the reagents, the oil samples are placed in a water vaporizer and then the water vapor is circulated to the reaction unit to be measured.

The standard test method for moisture content of oil-impregnated cellulosic insulation is described in ASTM D 3277. The major difference is that the moisture needs to be first extracted from the cellulose. It can be done by solvent extraction or by vaporizing. In order to thoroughly extract the moisture in the paper, the paper insulation needs to be delaminated. After extraction the Karl Fischer reaction instruments can then be used the same way as for the oil to give the moisture content.

The pressure gauge method "consists of degassing and dehydrating, by extraction in a vacuum, a known quantity from the studied body, oil, paper impregnated or non-impregnated, then to separate the different volatile compounds collected either by condensation on a cold point, or by combustion." [11]. The water extraction is then heated to vapor and the vapor pressure, measured by a mercury pressure gauge, is proportional to the quantity of water content.

These direct methods require removing the moisture, so they are not practical for on-line monitoring of the transformer insulation.

3.3 On-line Methods to Measure Moisture in Transformer Insulation

For oil, there are commercially available meters that measure the relative humidity of the transformer oil in real time such as the Harley moisture sensor from J. W. Harley Inc., and Aquaoil 100 A from Syprotech. The relative humidity can be converted to absolute moisture content by multiplying the relative humidity with the saturation moisture (solubility) of transformer oil at the measured temperature.

The recovery voltage method has been used for transformer diagnostics for years. It is based on the observation that the dielectric polarization spectrum of the paper insulation is directly related to conditions like aging and moisture content. A voltage pulse is first applied to the test specimen, which is then short circuited for a certain period of time. Then the specimen is open circuited and the return voltage is measured which can be related to the polarization spectrum. With a calibration, it can non-destructively provide the moisture content. One such commercial product is the Tettex Automatic Recovery Voltage Meter from the Tettex Instruments Division of the Haefely Trench AG. An application of this method is given in [12].

The recovery voltage time-domain measurement is currently a unique way to measure moisture on-line. However it only gives the average moisture content of the measured paper insulation. The three-wavelength frequency-domain interdigital dielectrometry sensor investigated in this project uses the same principle that the dielectric properties of the insulating material are directly related to the moisture content, but by having multiple wavelengths, the sensor can also measure the moisture spatial profile. Since the moisture distribution can cause a DC charge redistribution due to flow electrification induced charge separation of the electrical double layer by greatly affecting electrical leakage through the pressboard, this information is very critical to study the mechanism of flow electrification induced transformer failure.

3.4 Moisture Equilibrium Curves

It is useful to know the moisture partitioning curves between oil and paper under equilibrium conditions. When the transformer is in equilibrium operation, this provides a quick way of examining the moisture content in paper to predict future failure by measuring the moisture in oil. Over the years, many scientists have reported such a set of curves, but there has not been a comprehensive review and comparison for different curve sets. The research spans over several decades and is an important resource for electric utilities and insulation and testing equipment manufacturers. This chapter gives an overview of the classic moisture equilibrium curves and their history, and provides useful information on the relationships among them and their validity. Measurement results for oil solubility are also given.

3.4.1 Background

An excellent review of the basic concepts that are used in this section is given in [13]. A brief introduction is given here.

Transformer Oil

Transformer oil is made by refining crude oil. It is mainly a mixture of hydrocarbon compounds of three classes: alkanes, naphthenes, and aromatic hydrocarbons. These molecules have little or no polarity. A minor part of the constituents is that of polar and ionic species, which may greatly influence the chemical and electrical properties of the oil. "Polar compounds found in transformer oil usually contain oxygen, nitrogen, or sulfur. Ionic compounds would typically be organic salts found only in trace quantities" [13]. For a more complete review on transformer oil, refer to [14].

Water in Oil

Insulating oils, such as transformer oil, have a low affinity for water. However, the solubility increases markedly with temperature for normally refined naphthenic transformer

oil. This will be discussed more quantitatively later in this paper. Water can exist in transformer oil in three states: in practical cases, most water in oil is found in the dissolved state; certain discrepancies in examining the moisture content using different measurement techniques suggests that water also exists in the oil tightly bound to oil molecules, especially in deteriorated oil; when moisture in oil exceeds the saturation value, there will be free water precipitated from oil in suspension or drops. Moisture in oil is measured in parts per million (PPM) using the weight of moisture divided by the weight of oil (μg/g).

Relative Humidity

Relative humidity can be defined in terms of the moisture mixing ratio r versus the saturation mixing ratio r_s, $R.H.\% = 100r/r_s$, which is a dimensionless percentage. Relative humidity for air is the water vapor content of the air relative to its content at saturation. Relative humidity for oil is the dissolved water content of the oil relative to the maximum capacity of moisture that the oil can hold at that temperature. Because the saturation mixing ratio is a function of pressure, and especially of temperature, the relative humidity is a combined index of the environment and reflects more than water content [9].

Paper

The following four terms are often used interchangeably in the context of solid transformer insulation: pressboard, paper (or Kraft paper), Transformerboard, and cellulose. Although in the context of particular transformer insulation, they may indicate different parts, e.g. paper tape, paper cylinders, transformerboard cylinders, angle rings, blocks, etc., in the context of moisture equilibrium, they all in general refer to electrical grade paper insulation manufactured from unbleached sulfate cellulose, consisting of a more or less long chain of glucose rings. Pressboard has been well known in the textile and paper processing industries for more than a hundred years and was used in the first electric machines. Transformerboard resulting from the ef-

forts of Hans Tschudi-Faude of H. Weidmann Limited in the late 1920's [7] is a better type of pressboard meeting the requirements of large power transformers. It is made with high-grade sulfate cellulose, and consists solely of pure cellulose fibers without any binder. It can be completely dried, degassed, and oil impregnated. Insulation paper can be manufactured to different density, shape, and other properties for different applications.

Water in Paper

Water in paper may be found in four states: be adsorbed to surfaces, as vapor, as free water in capillaries, and as bound water. The paper can contain much more moisture than oil. For example, a 150 MVA, 400 kV transformer with about 7 tons of paper can contain as much as 223 kg of water [15]. The oil volume in a typical power transformer is about 80,000 liters. Assuming a 20 PPM moisture concentration in oil, the total mass of moisture is about 2 kg, much less than in the paper. The unit for moisture concentration in paper is typically expressed in %, which is the weight of the moisture divided by the weight of the dry oil-free pressboard.

Water Vapor Pressure

Water vapor pressure is the partial pressure exerted by water vapor. When a gas is in contact with a reservoir of water, in equilibrium it reaches the saturation water vapor pressure. Saturation vapor pressure is a measure of the tendency of a material to change into the gaseous or vapor state, and it increases with temperature. At the boiling point of water, the saturation water vapor pressure at the surface of water becomes equal to atmospheric pressure.

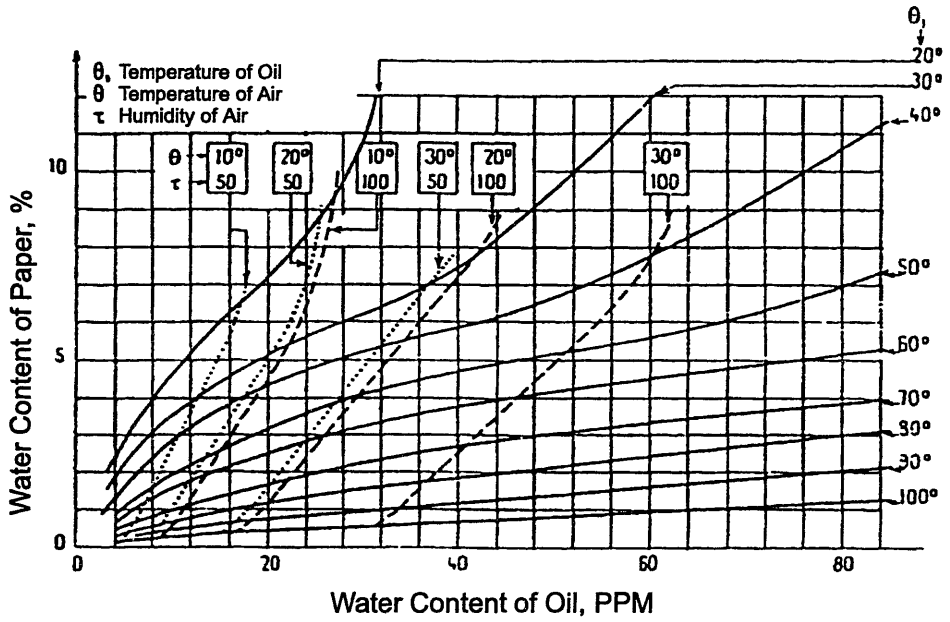

Figure 3.1: Fabre-Pichon Curves for moisture equilibrium of the air-oil-paper complex as a function of the air and oil surrounding the paper. Figure is taken from [6] except labels are translated into English.

3.4.2 Overview

Fabre-Pichon Curves

The moisture-equilibrium curve for an oil-paper complex was first reported by Fabre and Pichon [6] in 1960 and is shown in Figure 3.1. It is the most widely cited set of curves. The paper used was Kraft paper and an air-paper-oil complex was studied. A later summary of the work carried out at the same laboratory by Fallou [11], states that the moisture content of the oil and oil-impregnated pressboard were directly measured by the Karl Fischer reaction method.

The paper emphasized the equilibrium law which is similar to the principle that Oommen used in [16] to indirectly obtain the moisture equilibrium curves for oil-paper systems: "The relative humidity (that is to say referred to saturation value) is the same in the oil and in the air in contact with one another at the same temperature [17]." This was proved to be true within the limits of the experimental procedures by General

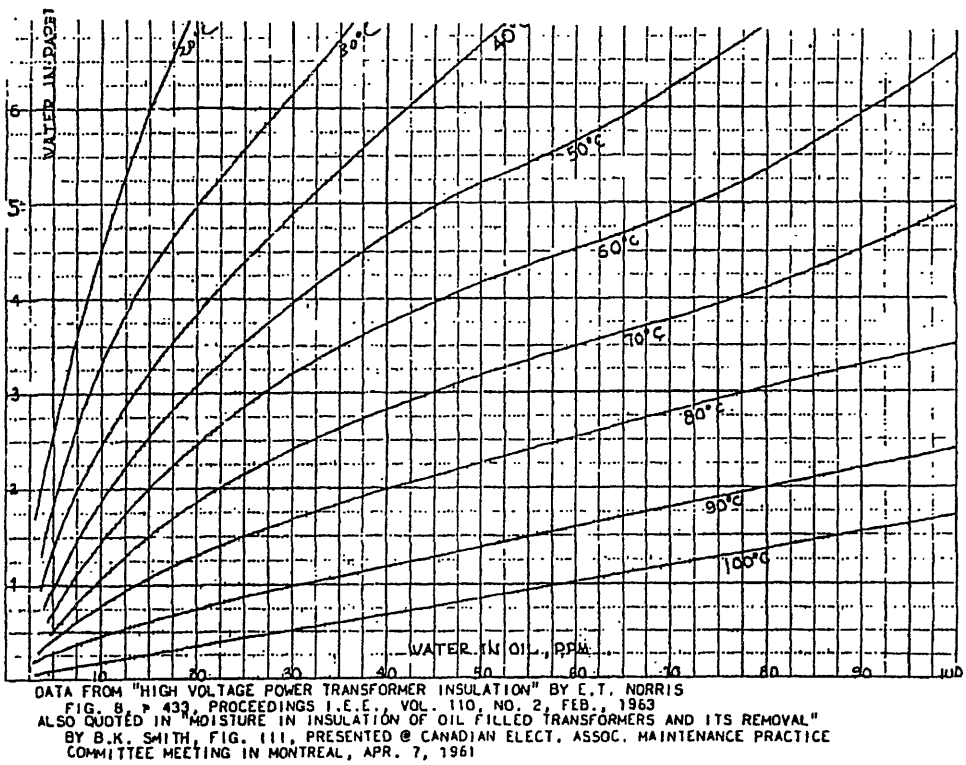

Figure 3.2: Curves redrawn by EHV-Weidmann for moisture equilibrium of the air-oil-paper complex as a function of the air and oil surrounding the paper.

Electric in 1960 [18].

In 1963, Norris referred to the Fabre-Pichon curves in Figure 8 of his paper [19]. Thus these curves became "affectionately" known as the "Norris Curves" even though they were originally published in Fabre-Pichon's paper [6]. EHV-Weidmann Industries, Inc., St. Johnsbury, Vt., a company specializing in Transformerboard manufacturing, redrew the curves shown in Figure 3.2 and credited Norris by noting data from [19]. Similarly, they are noted as "Norris Curves" in Figure 3 of [20], and Figure 5.4 of [21].

One possible reason for these historical mistakes is that Norris was perhaps the earliest exponent of the moisture transient processes in transformers. The other cause might be that Fabre-Pichon's paper [6] was published in CIGRE which is not a document that can be easily publicly accessed, and the original paper was in French—even the English translated paper still has French labels in all the figures. Many other

people redrew the curves in a different format and the true source got lost.

Oommen Curves

In 1983 Oommen developed a set of moisture equilibrium curves, published in [16] and shown in Figure 3.3. Oommen's method is based on the principle that the equilibrium curves represent the same relative saturation for the oil and for the paper at the same temperature. He combined the Moisture in Oil versus Relative Humidity Curves in air with Moisture in Paper versus Relative Humidity curves in air to make the Moisture in Paper versus Moisture in Oil equilibrium curves.

The Moisture in Oil versus Relative Humidity curves are straight lines with the relationship

$$x_w = x_w^s \times R.H., \tag{3.1}$$

where x_w is the moisture in oil in PPM, x_w^s is the water solubility in oil in PPM, and $R.H.$ is the relative humidity of oil.

Oommen used the oil equilibrium curves along with the Moisture in Wood Pulp versus Relative Humidity Curves made from Jeffries' Data [22] shown in Figure 3.4 and generated the moisture equilibrium curves for a paper-oil system shown in Figure 3.3. The dashed lines indicate desorption curves (diffusion of moisture out of cellulose), whereas the solid lines indicate the adsorption curves (diffusion of moisture into cellulose). For the same relative humidity, the moisture content of the desorption curves is slightly higher than that of the adsorption curves.

As pointed out by Reason in [23], if the relative humidity of the oil is measured by commercially available sensors, Jeffries' data in Figure 3.4 can be directly used to estimate the equilibrium moisture concentration in the pressboard.

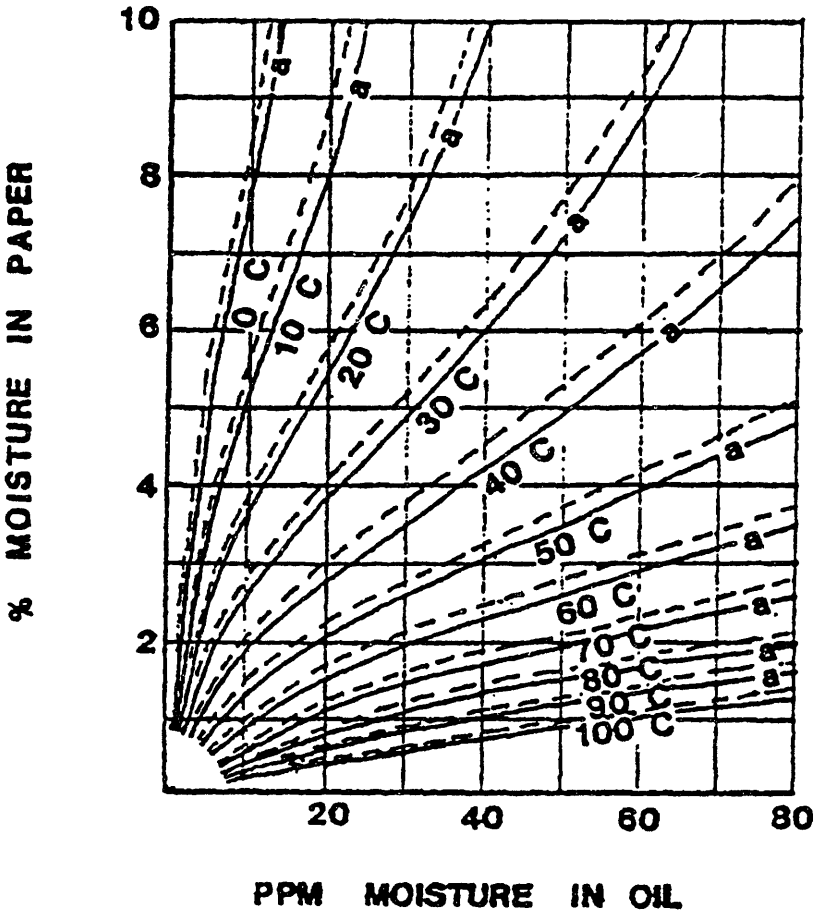

Figure 3.3: Oommen's Curves for moisture equilibrium for a paper-oil system [16].

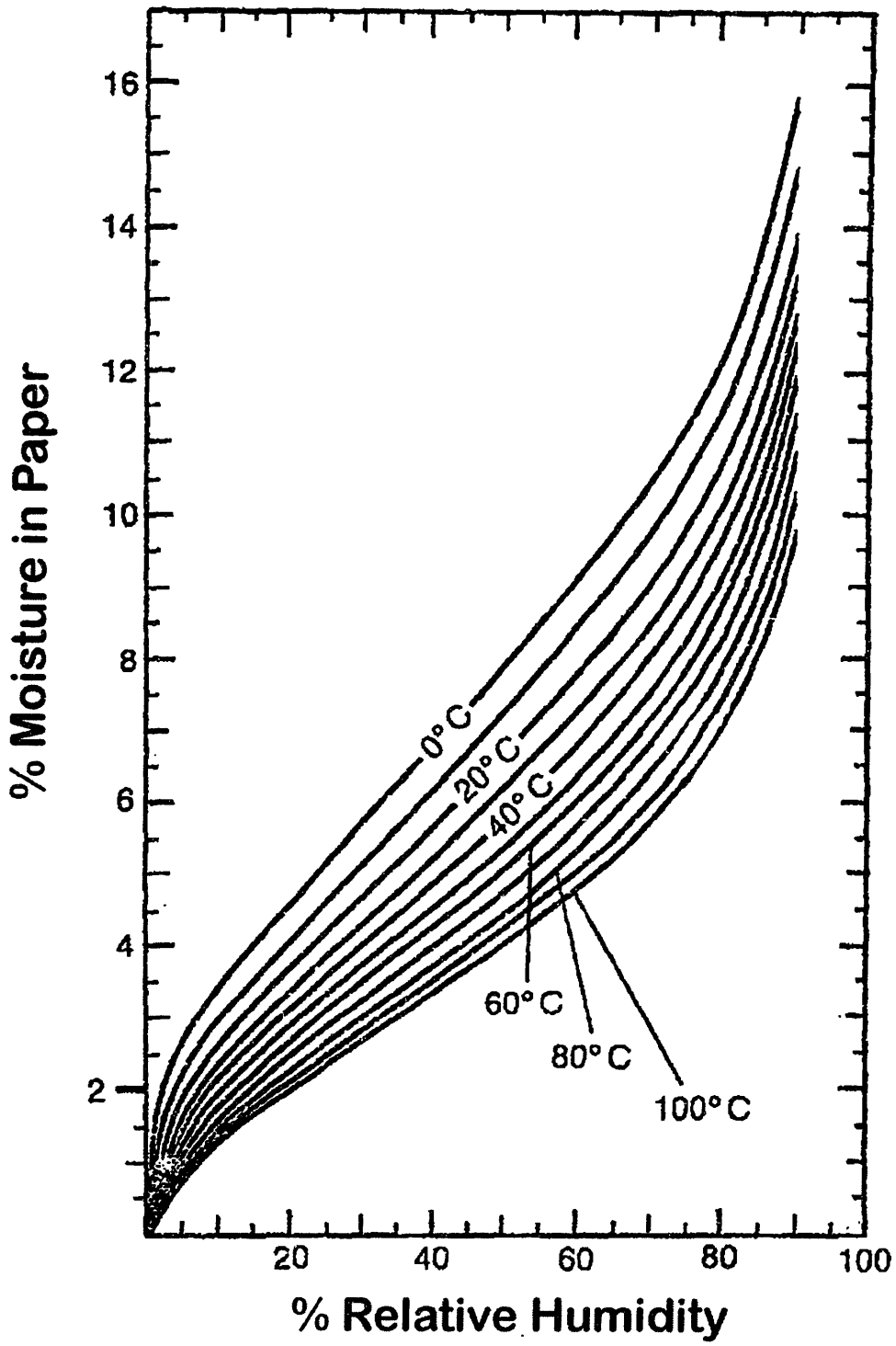

Figure 3.4: Moisture in wood pulp as a function of relative humidity of the ambient by Jeffries [22]. Figure supplied by Oommen at ABB-ETI who redrew Jeffries' data.

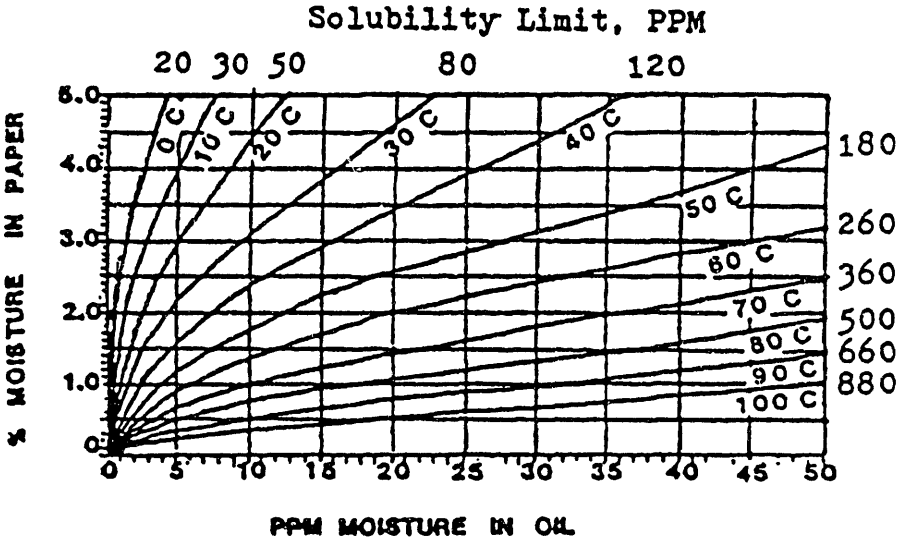

Figure 3.5: Oommen Curves for low moisture region of moisture equilibrium for a paper-oil system [16].

Figure 3.3 is not very reliable in the low moisture range due to the impractical conditioning of paper below 10% relative humidity. Hence, Oommen used the data of the vapor pressure of water in the gas space above the sample in a sealed system reported by Beer et. al. in 1966 [15] and converted to relative humidity by the relationship

$$\%R.H. = \left(\frac{p}{p_0}\right) \times 100, \tag{3.2}$$

where p_0 is the saturated water vapor pressure [24] and p is the water vapor pressure.

Combining the sorption curves for paper and oil again, Oommen constructed the sorption curves for the low moisture region as shown in Figure 3.5.

Equilibrium Curves for Water Vapor Pressure and Moisture Content

From both Fabre-Pichon and Oommen's statements, we see that the equilibrium curves for water vapor pressure and moisture content in paper can be used to derive the partition curves between oil and paper. Thus it is worthwhile to look at the evolution of this set of curves.

Piper (1946)

Among the families of equilibrium curves for water vapor pressure and moisture concentration of oil-free paper curves, the early and most widely used by manufacturers and utilities was reported by Piper [25] in 1946. Piper combined four groups of data from the literature to get a full set of curves: 1) data for cotton in high moisture concentration from Urquhart and Williams [26]; 2) data for cotton of low moisture content from Neale and Stringfellow [27]; 3) data for Kraft paper of low moisture content at elevated temperatures from Houtz and McLean [28]; and 4) data for spruce wood of high moisture content from Pidgeon and Maass [29]. By interpolation and extrapolation of experimental data, Piper derived that for the same vapor pressure, the moisture in Kraft paper is 1.7 times that of cotton.

Jeffries (1960)

This factor of 1.7 was then considered to be too high by Jeffries in 1960 compared with his data [22].

Beer et. al. (1966)

In 1966, Beer et. al. measured the water vapor adsorption curves for Kraft paper by a modified Edwards' apparatus [15]. In the sense of completeness, Beer's curve is apparently improved over Piper's because all Beer's data were obtained for Kraft paper directly.

Ewart (1974)

A paper by Guidi and Fullerton [30] covered the work performed by Ewart. Ewart's data also suggested that the paper water contents derived from cotton by Piper are too high.

Oommen (1984)

Beer's charts were not widely adopted, partly because it is not in a form that can be conveniently used. Oommen in 1984 [31] reconstructed similar charts using the data from Beer et. al. By comparison, he found the new charts will give slightly lower estimates of the moisture content for a given vapor pressure and temperature than the Piper chart.

Fessler et. al. (1987)

Fessler et. al. needed an accurate formula to build a model for bubble formation in transformers. Noticing the differences in the literature, they directly measured the moisture in paper and the moisture vapor pressure and did a comparison with existing reports [10]. Their results showed that the Piper database tends to be higher than any of the other databases and all of the other data is in reasonably good agreement. Fessler et. al. combined the data from Houtz, Ewart, Oommen and their own experiments and determined a water-paper equilibrium formula:

$$C = 2.173 \times 10^{-7} \times P_v^{0.6685} \times e^{(4725.6/T)}, \tag{3.3}$$

where P_v is the vapor pressure of water in atmospheres, C is the concentration of water in paper ($gH_2O/gPaper$), and T is the absolute temperature in ° Kelvin. The water vapor pressure as a function of water concentration and temperature is also given in the report:

$$P_v = 5.8869 \times 10^9 \times C^{1.4495} \times e^{(-6996.7/T)}. \tag{3.4}$$

However, from algebraic inversion of (3.3), the correct pressure relation is:

$$P_v = 9.2683 \times 10^9 \times C^{1.4959} \times e^{(-7069.0/T)}, \tag{3.5}$$

which significantly differs from (3.4). It appears that the derivation of (3.4) from (3.3) had an algebraic error. The difference between the two types of curves is shown in Figure 3.6.

Figure 3.6 further demonstrates that (3.4) is not the inverse of (3.3) because the calculated P_v at the highest concentration at 100°C should be one atmosphere.

Using (3.2), we can also construct curves for Moisture in Paper versus Relative Humidity shown in Figure 3.7 for formulas (3.4) and (3.5). There are large differences for the high relative humidity levels between the experimental data in Figure 3.4 and the fitted data in Figure 3.7. Oommen in [16] pointed out that the sorption curves cannot be fitted exactly by any mathematical relationship for the entire range. A multi-layer adsorption model predicts a sharp rise in moisture adsorption after 50%

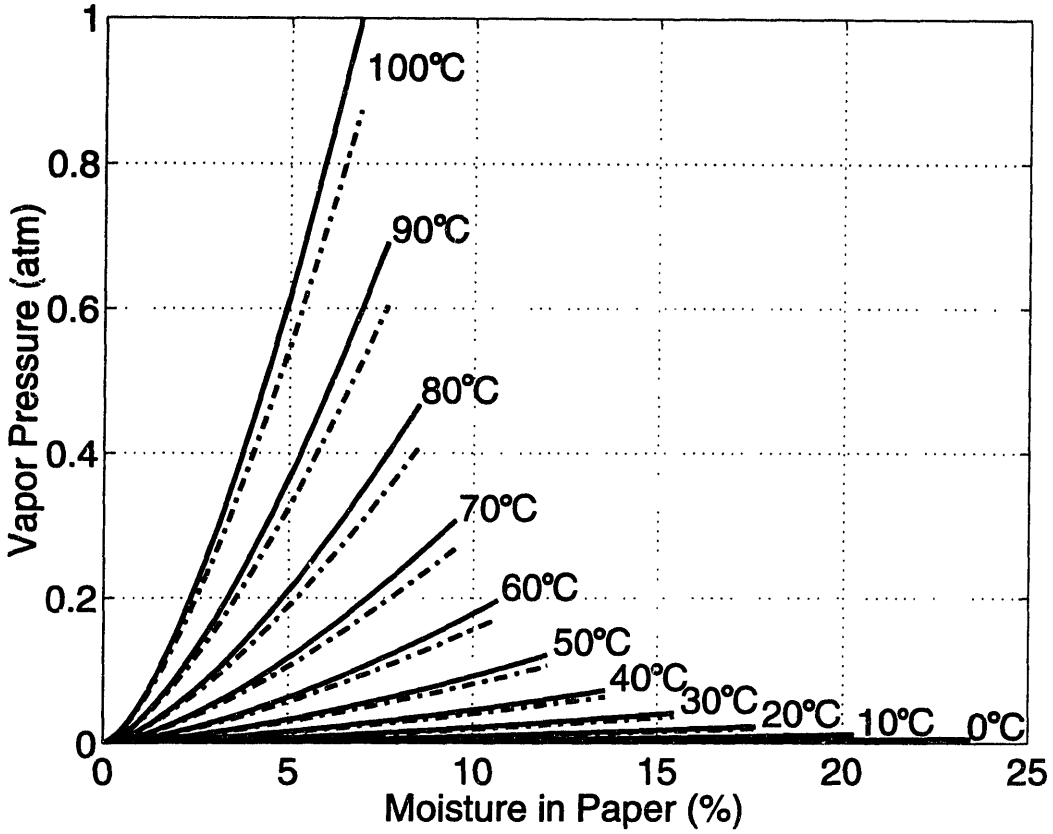

Figure 3.6: Vapor pressure versus moisture in paper comparing the erroneous formula of Equation (3.4) (dashed line) and the correct formula of Equation (3.5) (solid line).

RH [32]. Both Jeffries curves in Figure 3.4 and the Moisture in Paper versus Relative Humidity curve in Figure 1 of Ewart's report [18] show that the slope increases at high relative humidity level. Fessler et al's curves flatten out at the high end, which indicates possible error of the model for the high relative humidity region.

Oommen [33] also found out that the prediction of bubble evolution temperature using the mathematical model developed in [10] is off by 50 degrees in gas saturated systems. His study [33] gave the correct experimental results.

Griffin Curves

Griffin et al. at Doble Engineering in 1988 made similar curves for mineral oil and paper using Oommen's method [34]. The mineral oil refers to a typical naphthenic-based electrical insulating mineral oil.

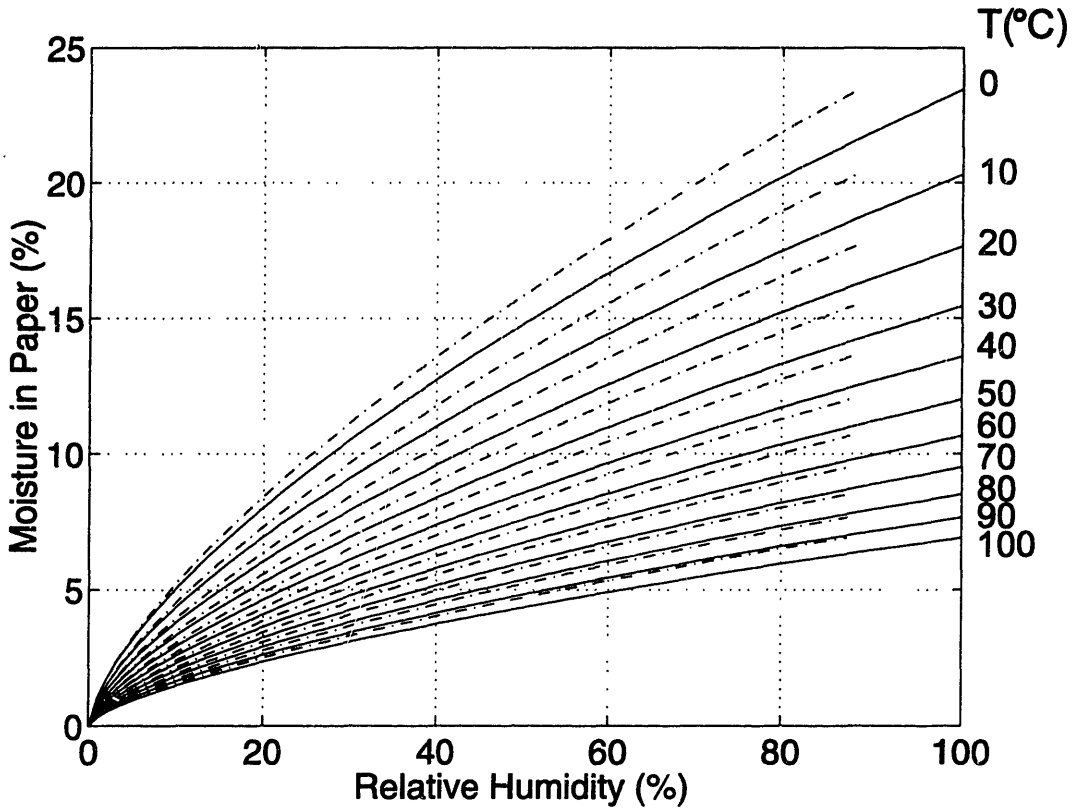

Figure 3.7: Moisture in Paper versus ambient Relative Humidity curves comparing erroneous Equation (3.4) (dashed line) and correct Equation (3.5) (solid line).

They used Fessler's formula (3.4) for vapor pressure and then converted to relative humidity using (3.2). Their original curves are shown in Figure 3.8. A comparison is given in Figure 3.9 for using (3.4) and (3.5).

MIT Curves

All of the above curves available in the literature are up to at most 100 PPM moisture in oil because the primary concern of moisture concentration in the transformer environment is within that range. However, our laboratory experiments that operate at high moisture concentrations require the curves to cover a wider range. Using Oommen's method and Jeffries' curves, we generated a wider range of equilibrium curves from 0°C to 100°C and moisture in oil up to 800 PPM shown in Figure 3.10. For water in paper below 1%, we use Oommen's curves in Figure 3.5.

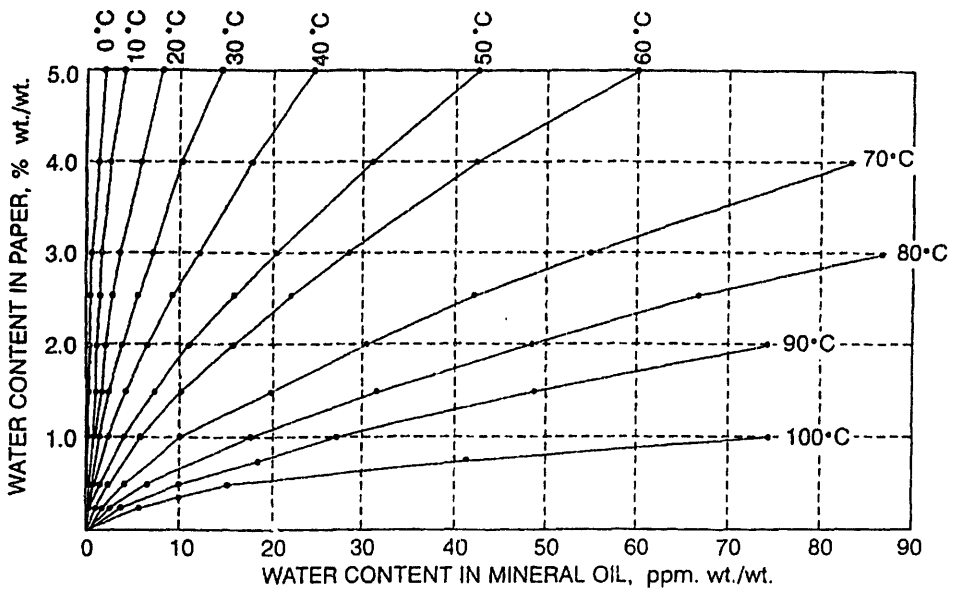

Figure 3.8: Griffin Curves for water equilibrium in cellulose/mineral oil systems [34].

3.4.3 Comparison

Direct Measurement versus Indirect Measurement

The advantage of Oommen's method is that it is much easier to determine the water equilibrium between the gas space and paper without the presence of the liquid insulation, as the moisture diffusion coefficients of oil-impregnated pressboard are about two orders of magnitude smaller than those of oil-free pressboard.

In 1974 Guidi and Fullerton in their paper [30] gave an empirical fit for diffusion coefficients of oil-impregnated Kraft paper from data studied by Ewart:

$$D(C,T) = D_0 e^{kC+E_a(1/T_0-1/T)}, \tag{3.6}$$

where $D_0 = 6.44 \times 10^{-14}$ m^2/s , $k = 0.5$, C is the moisture concentration in weight percent per unit weight dry cellulose, $E_a = 7700°K$, and T is the absolute Kelvin temperature. They didn't specify T_0; however, from Foss's work in 1987 [35], it appears that $T_0 = 298°K$.

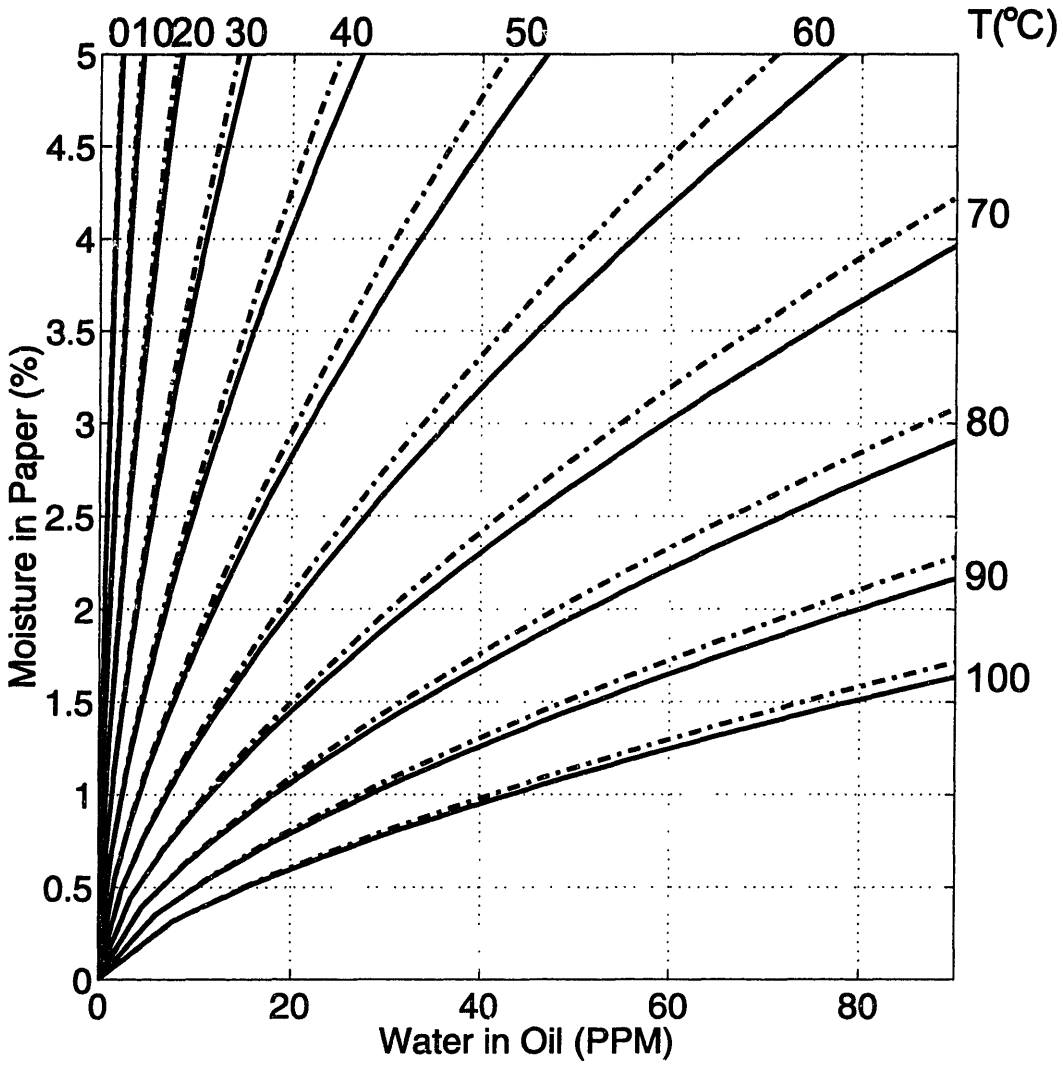

Figure 3.9: Regenerated curves following Griffin's procedure using erroneous Equation (3.4) (dashed line) and correct Equation (3.5) (solid line).

Foss in 1987 [35] generalized the empirical work by Ast [36] and Steele [37] at General Electric and fitted a diffusion coefficient for both oil-free and oil-impregnated paper into the same form as Guidi and Fullerton in (3.6) with $T_0 = 298°K$, $k = 0.5$, and moisture concentration C in percent by weight, and D_0 and E_a are shown in Table 3.1.

A comparison of diffusion coefficients D and the diffusion time τ for a piece of 1 mm thick pressboard with typical moisture concentration after drying of 0.5% are given in Table 3.2 using Foss' coefficients for (3.6). The diffusion time constant for moisture

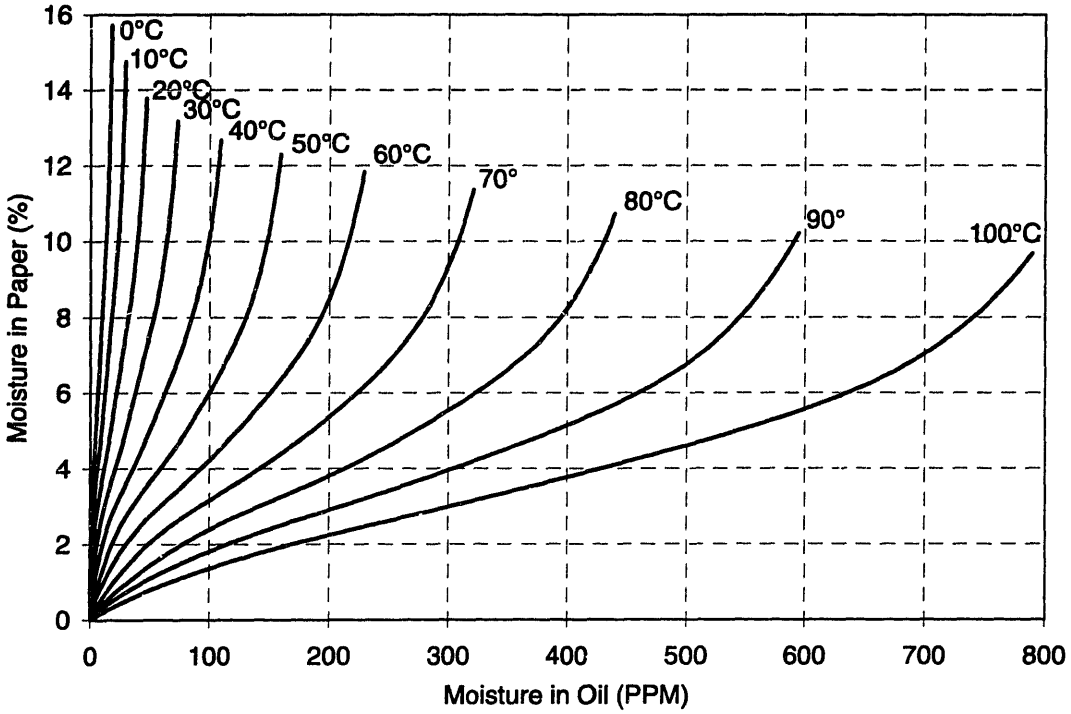

Figure 3.10: MIT developed curves for water equilibrium in cellulose/mineral oil systems for a wide range of moisture concentrations.

	D_0	E_a
Oil-free	2.62×10^{-11} m^2/s	8140 °K
Oil-impregnated	1.34×10^{-13} m^2/s	8074 °K

Table 3.1: Diffusion coefficient parameters estimated by Foss [35].

diffusing from both sides is calculated as

$$\tau = \frac{d^2}{\pi^2 D}, \tag{3.7}$$

where d is the thickness of pressboard. The diffusion time constant for moisture diffusing from one side is

$$\tau = \frac{4d^2}{\pi^2 D}. \tag{3.8}$$

This shows that the measurement for oil-impregnated pressboard with very small diffusion coefficient is much more susceptible to be in a non-equilibrium condition than that of oil-free pressboard with much large diffusion coefficient, particularly at low temperatures. That is why the direct measurement of the partitioning of the oil-paper

	Oil-Free Pressboard		Oil-Impregnated Pressboard	
T	$20°C$	$70°C$	$20°C$	$70°C$
$D(m^2/s)$	1.7×10^{-11}	9.5×10^{-10}	8.5×10^{-10}	4.7×10^{-12}
$\tau = d^2/(\pi^2 D)$ (hours)	1.7	0.03	333	6

Table 3.2: Comparison of diffusion coefficients by Foss [35] and double sided diffusion time for 1 mm thick oil-free and oil-impregnated pressboard using (3.6) and (3.7) with C=0.5%.

	Oommen [16]	Griffin [34]	Shell [38]
A	7.42	7.09	7.3
B	1670	1567	1630

Table 3.3: Comparison of estimated parameters for the Arrhenius form in (3.9) of the solubility of water in transformer oil.

system is not practical.

Water Solubility in Oil

The water solubility for oil can be expressed in Arrhenius form as

$$\log x_w^s = A - \frac{B}{T}, \tag{3.9}$$

where x_w^s is the saturation solubility of water in oil in PPM and T is the temperature in ° Kelvin. Different coefficients A and B by different authors are shown in Table 3.3, and the calculated oil solubility at different temperatures is given in Table 3.4.

The Shell and Oommen's data agree very well over the entire temperature range. Griffin's data differs from the Shell and Oommen data at high temperatures, perhaps due to difficulty of achieving saturation at high temperature with moist bubbles.

$T°C$	Oommen	Griffin	Shell
0	20	23	22
10	33	36	35
20	53	56	55
30	82	83	84
40	122	122	124
50	179	174	180
60	255	243	255
70	358	334	355
80	491	450	484
90	663	596	648
100	880	777	855

Table 3.4: Water saturation solubility in oil by different investigators.

3.4.4 Measurements of Moisture Solubility for Differently Conditioned Oils

It has been reported that oil with different aging conditions has different solubility. A verification was carried out as part of the thesis research. To avoid the difficulty of achieving full saturation, we utilize the linearity between the relative humidity of the oil and the moisture content of the oil to find the solubility.

The oil is contained in a 1000 ml kettle. It is mixed by a magnetic stirrer and the temperature is controlled by an Omega temperature probe and controller. The moisture is either bubbled into the kettle at low temperature or introduced using deionized water impregnated pressboard at high temperature. The calibrated Harley humidity meter measures the relative humidity of oil and the Mitsubishi Moisture Meter is used to measure the absolute moisture content in oil.

Since

$$M_c(PPM) = M_s(PPM) \times R.H.(\%)/100, \tag{3.10}$$

where M_c is the moisture concentration, and M_s is the moisture solubility at that

Oil Type	Fresh Shell Diala A [38]	Lab-Aged Shell	Texas Utility	Ramapo
Solubility (PPM)	102	104	108	142

Table 3.5: Comparison of measured water solubility at 35°C in differently conditioned oils.

temperature, by measuring the slope of the curve of *Moisture Concentration* versus *Relative Humidity*, one can find the solubility instead of trying to directly measure the moisture content at 100% relative humidity.

The measurements are taken for four types of differently conditioned oil at 35°C: Fresh Shell Diala AX oil, Lab-Aged Shell Diala A, Texas Utility transformer oil, and Ramapo transformer oil. The lab-aged oil is prepared by heating the oil at $70°C$ for two weeks with a mixture of moisture and oxygen as heat, moisture and oxygen are the major aging factors. The results are shown in Table 3.5 and the curves are shown in Figure 3.11.

The results of fresh oil, lab aged oil, and the Texas Utility oil are very close whereas the result of Ramapo oil is very different from the rest. Ramapo oil was taken from a transformer that experienced failure. By observing the oil color and transparency, we can tell that Ramapo oil is severely aged. This verifies the results of Griffin at Doble: "oils which are in serviceable condition show little change in their water solubility characteristics. Only when the oil is severely aged or contaminated would the solubility be expected to increase significantly." [34] There might be contaminants in the Ramapo oil that cause the oil moisture sensor response to be not very linear.

3.4.5 Curve Comparison

Due to the differences in the moisture solubility of oil, the moisture in paper versus relative humidity, and different measurement accuracy, the curves generated by different investigators show differences. A comparison for different moisture and temperature levels is shown in Table 3.6. Oommen curves and MIT's curves are generated from the

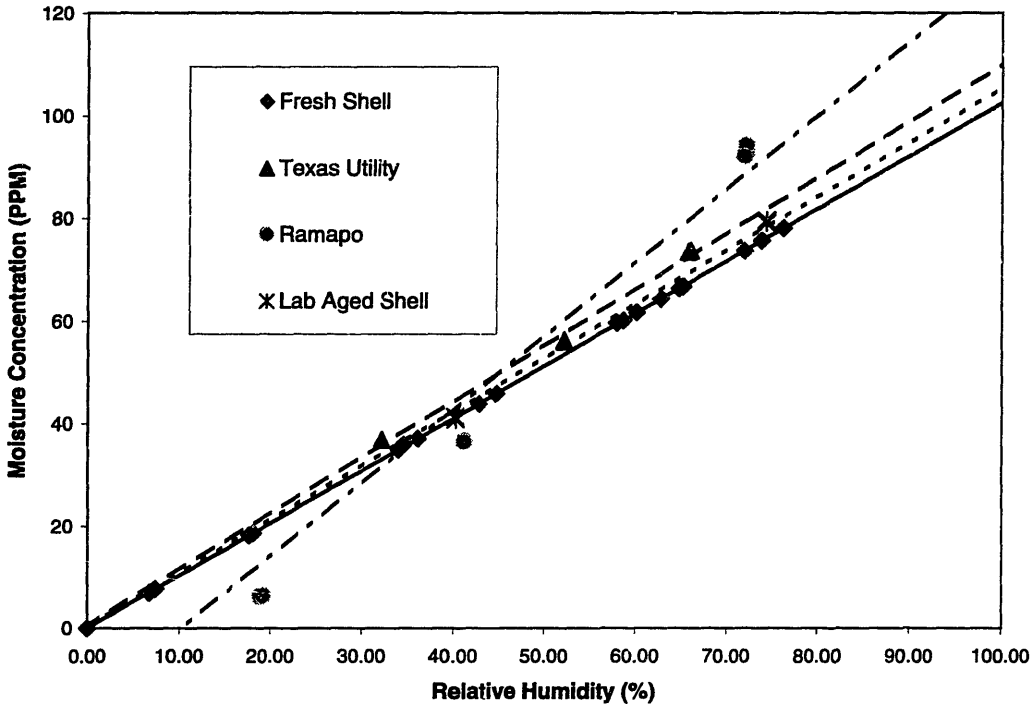

Figure 3.11: Measurements of moisture concentration versus the relative humidity for differently conditioned oil.

same source.

Authors	Fabre-Pichon [6]	Oommen [16]	Griffin [34]
10 PPM 70C	1.1 %	1.0 %	1.0 %
10 PPM 30C	3.4 %	3.1 %	4.0 %
60 PPM 60C	4.5 %	2.9 %	5.0 %
80 PPM 70C	3.8 %	2.7 %	3.8 %

Table 3.6: Equilibrium moisture in paper under various oil moisture and temperature conditions as reported by different authors.

The curves are close to each other at low moisture concentration levels in paper. The moisture content in paper in Oommen curves [16] is consistently lower than that in Fabre-Pichon [6] and Griffin [34]'s for the same moisture concentration in oil. The major differences occur at low temperature, and at high moisture concentration levels in paper with high temperature.

3.4.6 Case Study

An examination of the moisture equilibrium curves was carried out using experimental data. The paper-oil system is initially dried under vacuum and then the dry oil is removed and moist oil is introduced to the system. A three-wavelength interdigital sensor is used to monitor the moisture diffusion process [39, 40]. The final moisture content in the pressboard and oil can be calculated using mass balance either from measurement or calculation using the oil-paper equilibrium moisture curves.

Method 1: The moisture diffusion from oil to pressboard is monitored in the oil using a Harley moisture meter as shown in Figure 3.12. Since the system is sealed, the total moisture in the system is a fixed quantity, divided between oil and pressboard. By knowing the moisture in the oil at the beginning and in the end, the final moisture concentration in pressboard can be determined. Quantitative calculations are given in Table 3.7.

Method 2: We could not directly determine the amount of moisture in the pressboard in equilibrium for our test from any of the published curves, since none of them gives moisture concentration in oil greater than 100 PPM while the equilibrium concentration is 113 PPM. However, by inspection, we find the Fabre-Pichon and Griffin curves won't fit the data, because even at 80 PPM those curves already indicate about 4% moisture in paper; the value that corresponds to 113 PPM will be more than 3.5% as estimated in Method 1. Using the MIT curves of Figure 3.12, we get consistent values as illustrated in Figure 3.13.

The straight line is the mass conservation curve based on the equation:

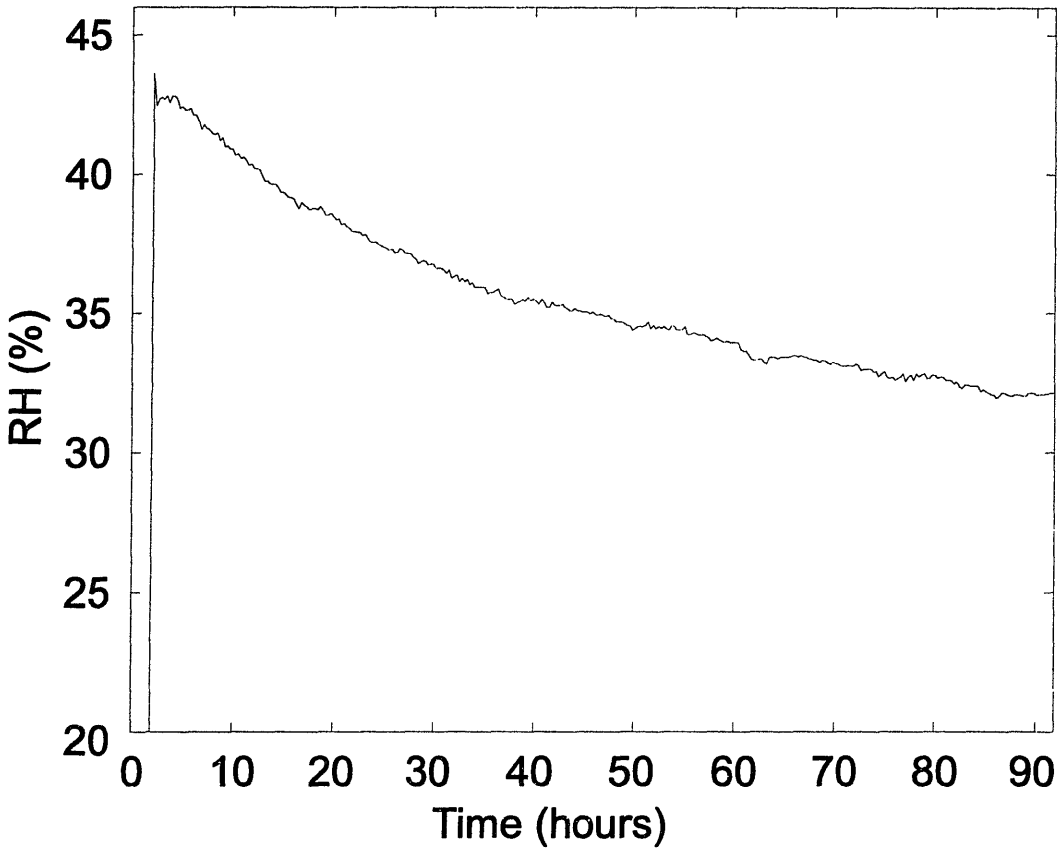

Figure 3.12: The relative humidity of the oil decreases as the moisture diffuses from oil into pressboard.

$$P_{paper}(\%) = \frac{W_{total} - W_{oil}}{M_{paper}} \times 100, \tag{3.11}$$

where W_{total} (g) is the total moisture mass in the system, which is also the moisture in the oil at the beginning since we start with very dry pressboard; W_{oil} (g) is the moisture mass in oil during the experiment, which equals the water in oil in PPM times the total oil mass; M_{paper} (g) is the mass of the pressboard, and P_{paper} (%) is the percentage of water in pressboard. Substituting our numbers in Table 3.7 to (3.11) gives:

$$P_{paper}(\%) = 14.1 - 0.093 \times W_{oil}(PPM), \tag{3.12}$$

RH of oil at beginning(after T stabilized at $70°C$)	43%
RH of oil at equilibrium:	32%
Saturated mass fraction x (PPM) at $70°C$	$x = 353PPM$
PPM moisture in oil at beginning	$P_b = RH \times 353PPM = 152PPM$
PPM moisture in oil in equilibrium	$P_e = RH \times 353PPM = 113PPM$
PPM moisture diffuses to pressboard	$\triangle P_w = P_b - P_e \approx 39PPM$
Total weight of oil	$m_{oil} \approx 5300g$
Total moisture diffused into pressboard	$\triangle m_w = m_{oil} \cdot \triangle p_w \approx 0.2g$
Total weight of dry pressboard	$M_{paper} = 5.7g$
% change of moisture in pressboard	$P_{paper} = \triangle m_w / m_p \approx 3.5\%$

Table 3.7: Quantitative calculation of moisture transfer from oil to pressboard using Method 1.

The line is completely defined by the initial condition and the system configuration, i.e. independent of the final moisture measurement. The intersection of the mass conservation line with the moisture partition curves at $70°C$ indicates the equilibrium value for the system. From this curve, the final moisture in oil is about 115 PPM and the moisture in paper is about 3.5%. This is consistent with the result derived from Method 1.

3.5 Conclusions

Several sets of classic moisture equilibrium curves are studied and a comparison is given for each method. Caution should be taken when using such curves because they differ by measurement techniques, data sources, and generating methods. An experimental case study shows that Oommen's curves match the experimental data best.

When the system is not in equilibrium, these equilibrium curves cannot be used to find the moisture in paper. A three-wavelength interdigital dielectrometry sensor developed at the MIT High Voltage Research Laboratory is able to measure the spatial profile of the moisture distribution in the pressboard [39, 40]. This provides an

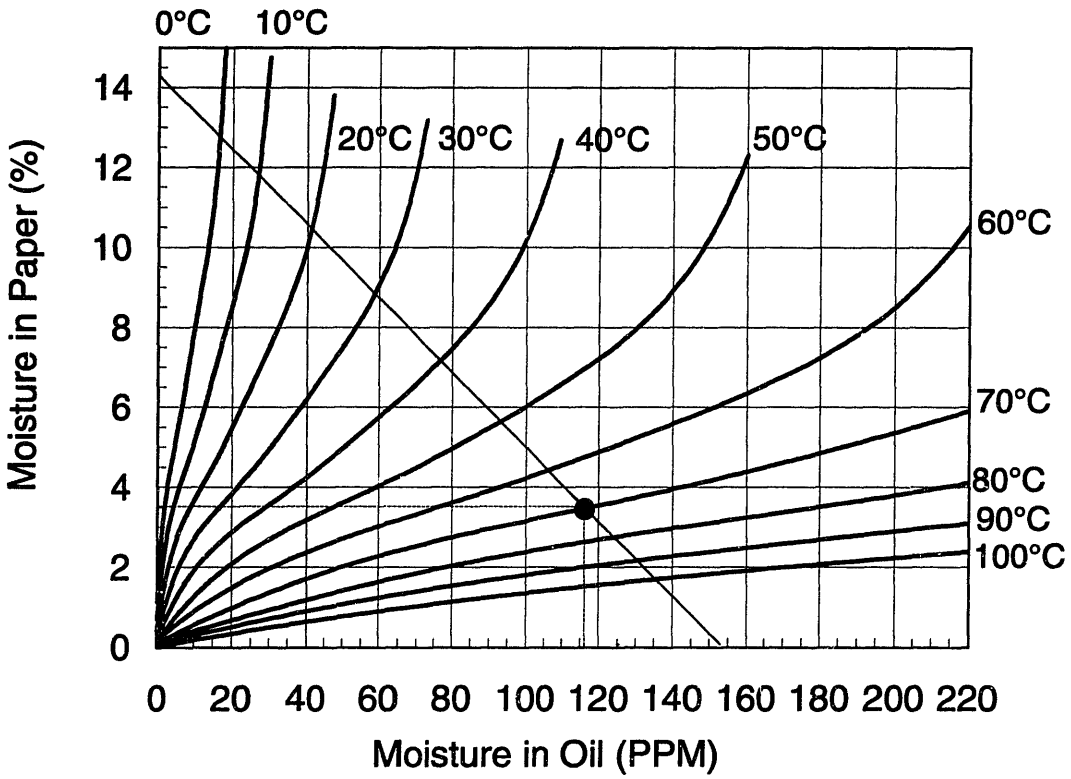

Figure 3.13: System equilibrium operating point found using the moisture equilibrium curves for oil and paper system and (3.12).

alternative method when the transient system is not in equilibrium.

Chapter 4

Universal Curves

4.1 Introduction

The dielectrometry spectrum of pressboard, $\varepsilon* = \varepsilon' - j\varepsilon''$, is a function of its temperature and moisture content. The real part of the permittivity gives the dielectric constant, while the imaginary part characterizes the power dissipation in the material. In transformer pressboard of medium and low humidity, it has been shown the dielectric spectrum does not vary in shape with temperature and moisture content, but there is a logarithmic shift in amplitude and frequency. Research conducted by Y. Sheiretov at MIT [41], Jonscher et al at Chelsea Dielectrics Group in the UK [42], and Nettelblad et al at ABB [43] suggest the existence of such a universal curve. Thus it is possible to create a universal curve, with appropriate temperature correction factors, containing information about the moisture contents from transformer pressboard dielectrometry measurements.

Extensive measurements of dielectric properties of transformer pressboard as a function of moisture and temperature were conducted in the interest to quantify effects that will allow the prediction of moisture content of insulation by measuring its dielectric spectrum, thus allowing an on-line non-destructive method. From oil-free pressboard measurements, it can be observed that a universal curve does exist. Preliminary tests for oil-impregnated pressboard show the same trend.

Such measurements were taken by MIT undergraduate students Madhu Sarda and Noemi Altamirano under my supervision as part of their MIT Undergraduate Research Opportunity Program and Advanced Undergraduate Projects [44].

Similar tests have been done by Nettelblad [43] for oil-free cellulose, but no quantitative relationship is given.

4.2 Measurements for Oil-Free Pressboard

4.2.1 Measurement Technique

The pressboard is placed in a lossy parallel-plate capacitor structure whose complex impedance is measured. The values of the complex permittivity of the material, averaged across the thickness were obtained from the complex impedances according to (4.1). Once a quantitative mapping is established for dielectric properties as a function of moisture and temperature, the interdigital dielectrometry sensors can be used to continuously monitor the moisture distribution in the transformer insulation.

$$\varepsilon* = Y_{12} \cdot d/j\omega A = (G_{12} + j\omega C_{12}) \cdot d/j\omega A = \varepsilon' - j\varepsilon''. \tag{4.1}$$

where d is the electrode gap, A is the electrode area, G_{12} is the conductance between electrodes, and C_{12} is the capacitance between electrodes.

Hi-Val transformer pressboard manufactured by EHV-Weidmann Inc. is used for all experiments. The 1.7mm thick pressboard was placed between the parallel plate sensor, shown in Figure 4.1. The parallel plate sensor was then placed in the test vessel shown in Figure 4.2.

Temperature and relative humidity were monitored in the vessel by an Omega temperature controller and a Harley relative humidity sensor. The relative humidity inside the vessel was varied in order to achieve different moisture contents of the pressboard. The moisture content in the pressboard is estimated using Jeffries' curve [22] by measuring the relative humidity in the test vessel. Oil-free measurements were taken at

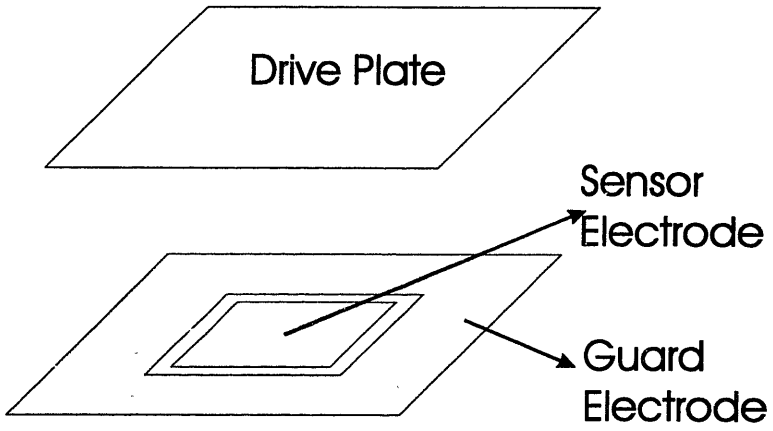

Figure 4.1: Parallel plate sensor used in this research.

Moisture Level(%)	0, 0.6, 1.1, 1.9, 2.0, 2.3, 2.6, 3.2, 5.7
Temperature (°C)	30 (35), 40, 50, 60, 70

Table 4.1: Moisture and temperature levels for measurements performed for oil-free pressboard.

the moisture and temperature levels shown in Table 4.1.

4.2.2 Measurement Results

Data was collected for the five temperatures at every moisture level in Table 4.1. Data of different moisture levels at the same temperature were also compared. Both ε' and ε'' increase as moisture is increased. All results are plotted in 3-D in Figure 4.3 and Figure 4.4. It is observed that a general shape is common to all temperatures and moisture levels.

Figure 4.5 shows the dielectric spectrum for different temperatures at 2.0% moisture content. Both ε' and ε'' increase as temperature increases, however, the shape remains the same.

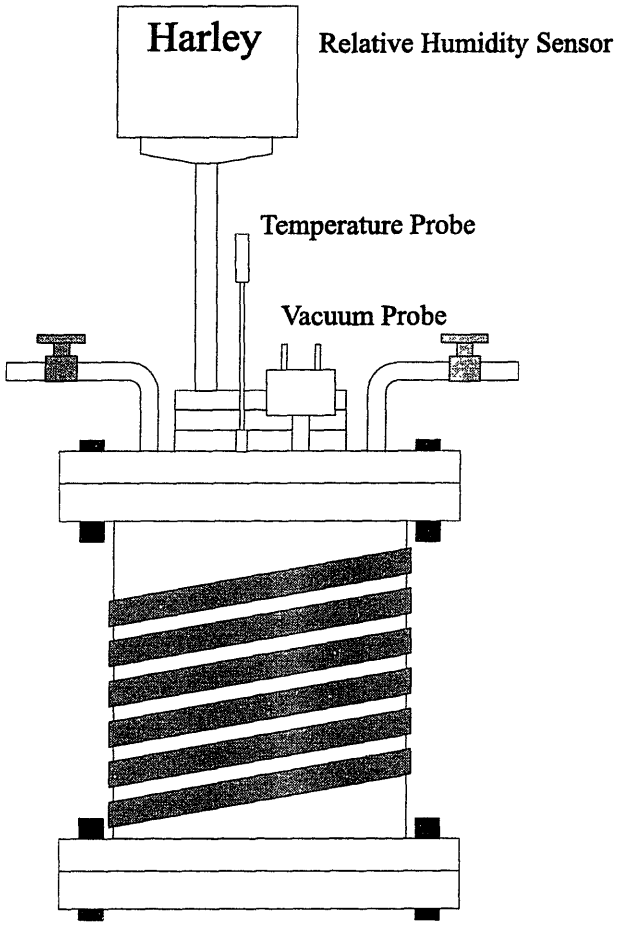

Figure 4.2: Test vessel used for oil-free measurements

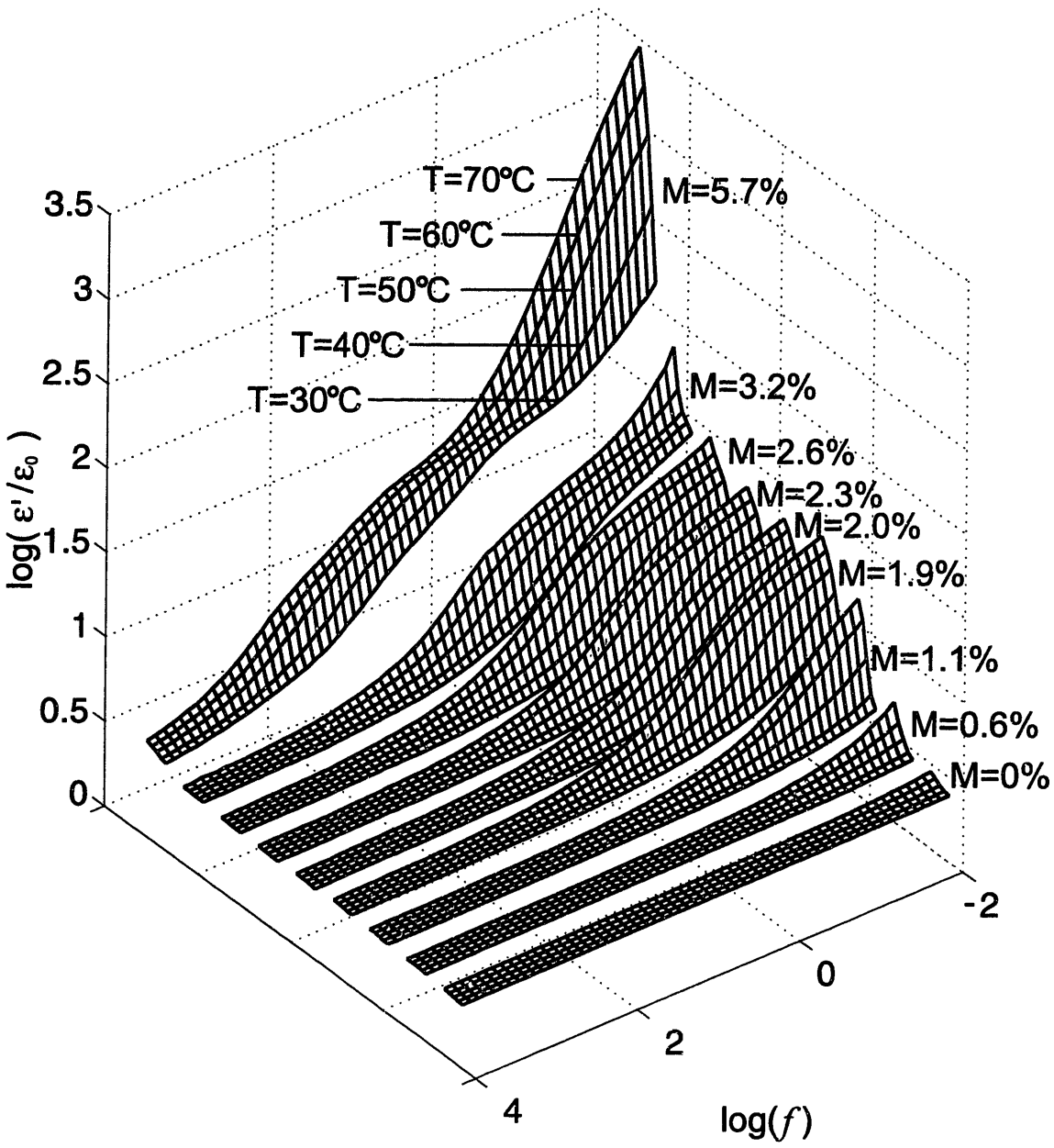

Figure 4.3: A full spectrum of ε' obtained for nine moisture levels and five temperatures.

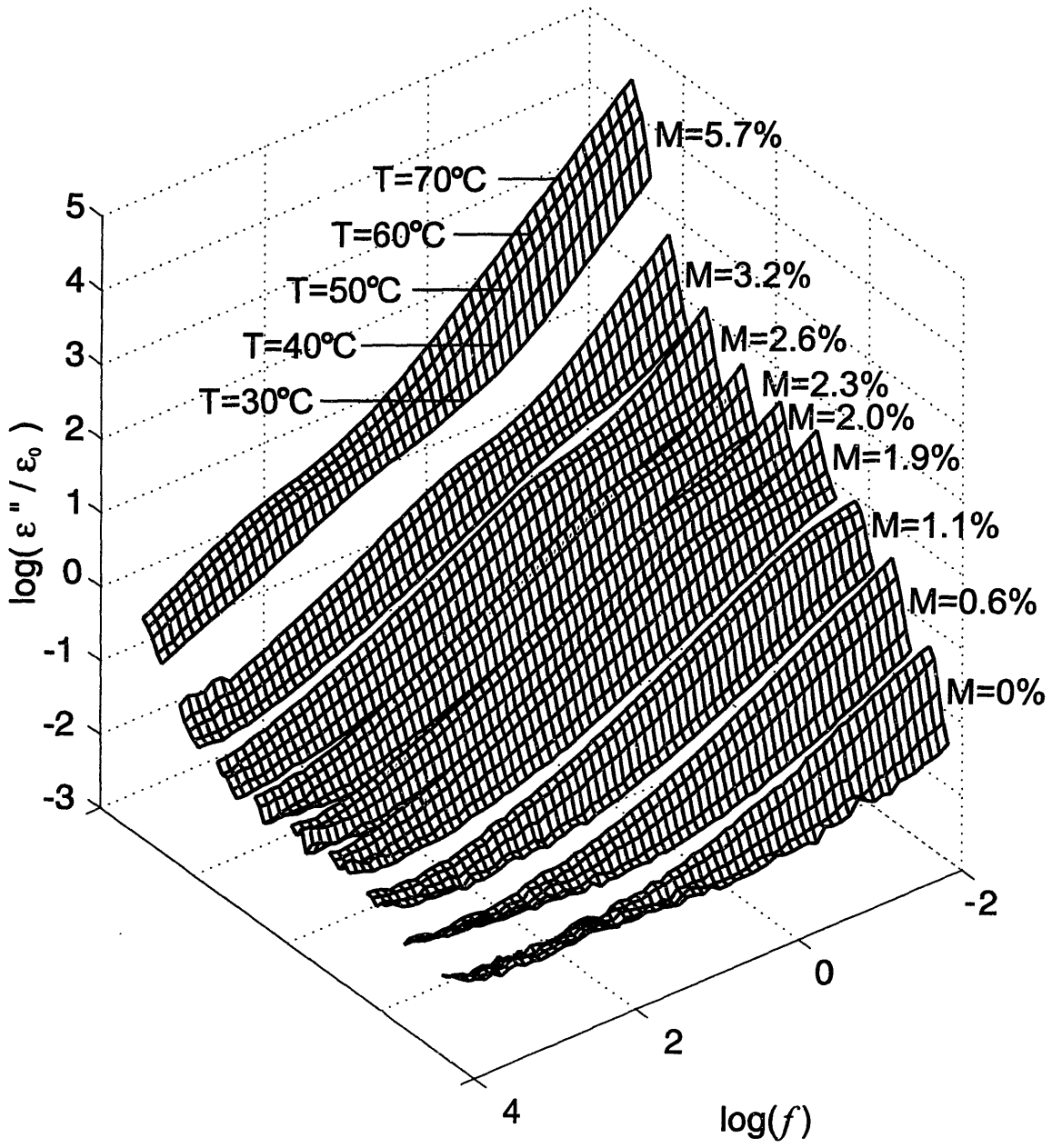

Figure 4.4: A full spectrum of ε'' obtained for nine moisture levels and five temperatures.

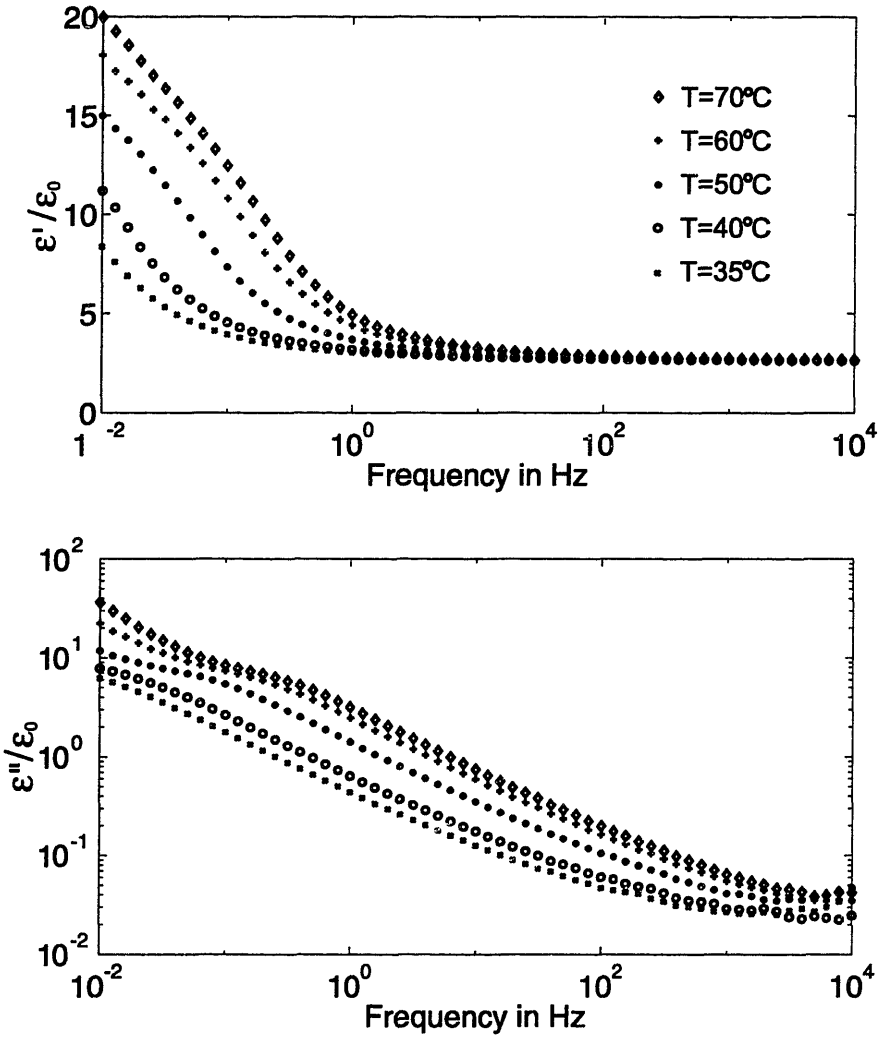

Figure 4.5: Dielectric spectrum of oil-free pressboard at 2.0% moisture content for five temperatures.

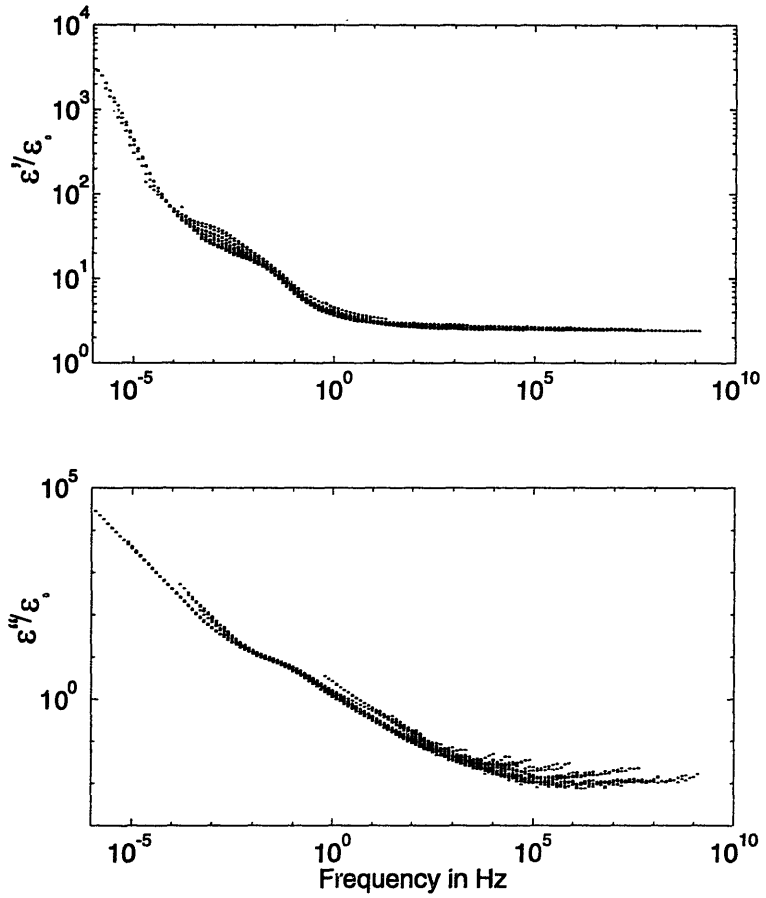

Figure 4.6: Discrete frequency shifting of the measured oil-free pressboard data to minimize least square differences suggests the existence of a universal curve.

Discrete logarithmic frequency shifting of the measured oil-free pressboard data to minimize least square differences confirm the existence of a universal curve in Figure 4.6.

4.3 Universal Curve Model and Fitting

The most important task of establishing such a universal curve was to find the proper model. A polynomial fit is the easiest and can fit the data fairly well at the measured frequency. However it blows up at high frequency, and has no physical meaning. A time invariant RC circuit model does not fit the dispersive nature of the pressboard.

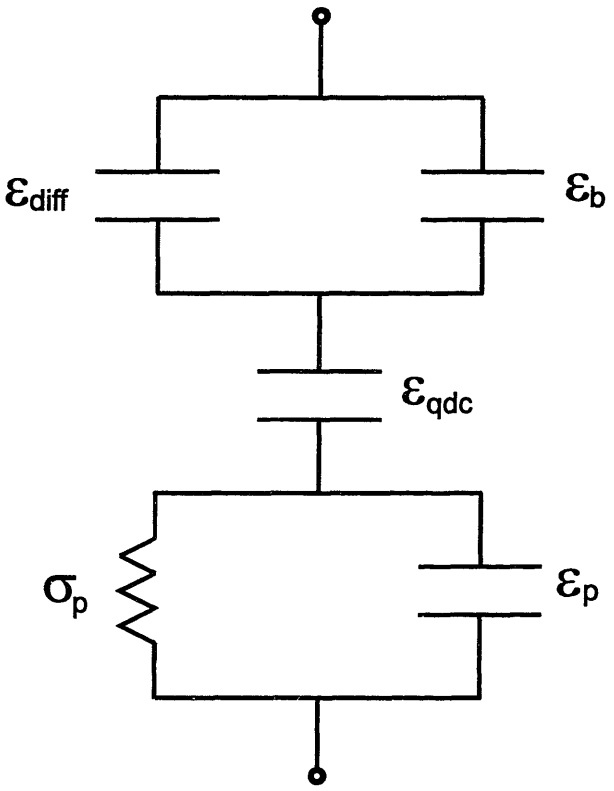

Figure 4.7: Model for the Universal Curve.

Even simple dielectric models such as the low frequency dispersion model in [45] would not account for the double inflection points in the measurements. A model developed by Hill et al. [46] for biological cell tissues was used and is shown in Figure 4.7. Hill et al.'s model consists of low frequency diffusion described by relative permittivities ϵ_{diff} and ϵ_b capacitors in parallel, low frequency dispersion for the single series capacitor described by relative permittivities ϵ_{qdc}, and a lossy bulk dielectric described by the RC parallel structure with conductivity σ_p and relative permittivity ϵ_p. The model parameters are further described by the following set of equations:

$$\varepsilon_{diff} = \varepsilon_d (j\omega/\omega_d)^{n_d - 1}, \tag{4.2}$$

$$\varepsilon_{qdc} = \varepsilon_q \left((j\omega/\omega_q)^{n_q - 1} + (j\omega/\omega_q)^{-p} \right), \tag{4.3}$$

and ϵ_b, ϵ_p, and σ_p are frequency independent.

ϵ_d	$\omega_d(rad/s)$	n_d	ϵ_b	ϵ_q	$\omega_q(rad/s)$	n_q	p	$\sigma_p(pS/m)$	ϵ_p
1.27	0.455	0.045	30.7	2.96	4.17	0.996	0.656	3.48×10^4	1.16×10^4

Table 4.2: The parameters of the universal curve model.

$E_a/\kappa(^\circ K)$	k_1	k_2	k_3
3.79×10^3	-1.23	0.218	-0.0348

Table 4.3: The parameters of the logarithmic shifting for the universal curve in Figure 4.7.

The logarithmic shifting is mathematically represented by

$$k = E_a/\kappa \cdot (1/T - 1/T_0) + k_1(M - M_0) + k_2(M - M_0)^2 + k_3(M - M_0)^3, \qquad (4.4)$$

where E_a is the thermal activation energy, κ is Boltzmann's constant, T is the temperature in Kelvin, T_0 is the reference temperature and chosen to be 323 ° K, M is the moisture concentration in percent, and M_0 is the reference moisture concentration and in this case is 2.0%.

Using a constrained minimization routine of Matlab, the parameters of the model are found in Table 4.2 and the shifting parameters are found to be those of Table 4.3.

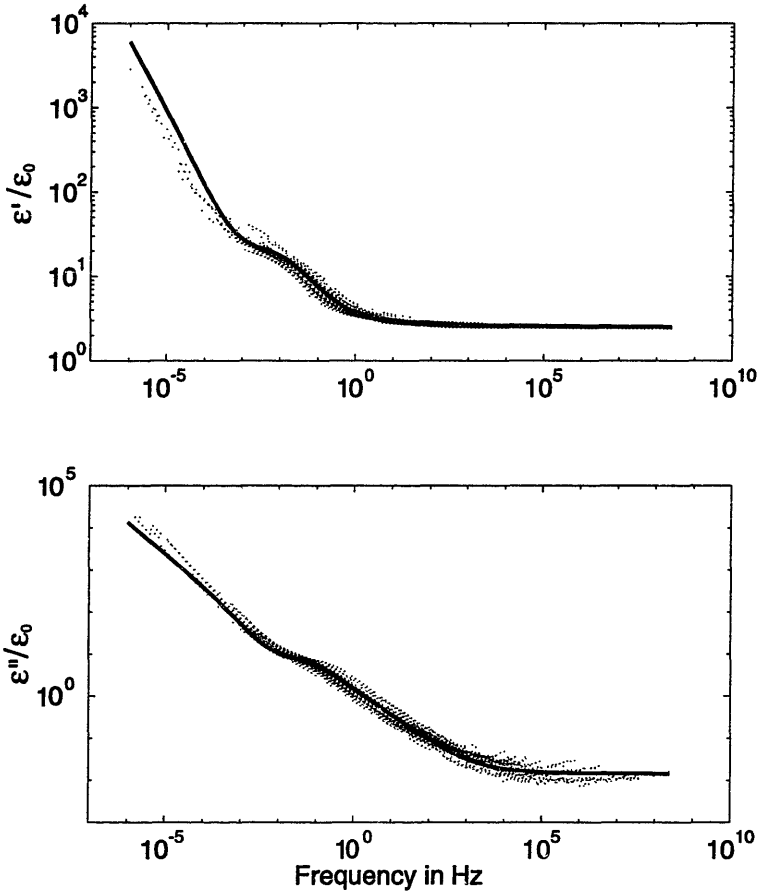

Figure 4.8: Universal curve for oil-free pressboard. The solid line is the curve calculated from the model. The dotted lines are the shifted data points.

Moisture C[illegible]t(%)	0,1.12,1.16,1.34,1.48,1.82,7.81
Temperatu[illegible]C)	30,40,50,60,70

Table 4.4: Moisture content and temperature levels at which oil-impregnated measurements were conducted.

4.4 Measurements for Oil-Impregnated Pressboard

The system used for oil-impregnated pressboard is consisted of an oil reservoir and a testing chamber. Oil was stored and conditioned in the oil reservoir. This oil was then transported to the testing chamber where the pressboard samples were impregnated and processed. The same parallel plate sensor, used in the oil-free measurements, was used for oil-impregnated pressboard measurements. The parallel plate sensor was placed inside the testing chamber for measurements. The moisture levels and temperatures at which measurements were conducted are shown in Table 4.4.

As can be observed, the range of moisture levels for this case is limited. This is due to the fact that diffusion of moisture from the oil to the pressboard takes much longer than that in the oil-free pressboard case. Thus the control of the moisture level is more difficult and it takes much longer for high levels of moisture to diffuse into the pressboard.

4.4.1 Measurement Technique

Hi-Val 1.7mm thick transformer pressboard impregnated with Shell Diala AX oil was used for the oil-impregnated pressboard measurements. The oil had to be conditioned in the oil reservoir at 70°C. Achieving a broad range of moisture levels for this case was a challenge since high relative humidity of oil is hard to achieve at high temperature. The moist air bubbled in was produced in the same flask and hotplate as in the oil-free case. At high temperature, since the oil can dissolve a large amount of moisture, the flask was heated again.

Once the oil was conditioned it was then circulated into the test chamber where

pressboard samples were placed to absorb the moisture introduced into the oil. A mesh wire net was placed inside the test chamber to ensure that both sides of the pressboard would remain exposed to the oil. The pressboard samples were conditioned by filling the test chamber with oil from the reservoir. Oil was then circulated within the test chamber to allow for a uniform mixture of the oil to occur. Samples were left to condition in the testing chamber for at least 48 hours.

After conditioning a sample, the parallel plate sensor was assembled with the sample placed between the plates. An even amount of force was applied on each corner by nylon screws in order to avoid air gaps from forming between the sensor and the pressboard. The assembled sensor was then placed in the test chamber to commence measurements.

Oil-impregnated measurements were conducted at 30, 40, 50, 60,and 70°C for each moisture level. The first measurement was taken at 70°C and the temperature was decreased by 10°C after each set of measurements. Due to the large thermal mass of oil, it took longer for the temperature to decrease and stabilize compared to the oil-free case, but since the diffusion time for the oil-impregnated pressboard is also much longer than that of the oil-free pressboard, it was still reasonable to assume that within the time frame of temperature change, the moisture is constant in the pressboard sample throughout the measurements for each moisture level.

For the oil-impregnated case moisture measurements of oil were also performed. Before each set of measurements the oil's moisture content was measured using the Mitsubishi Moisture Meter. The same measurement was conducted after the last measurement at 30°C. There were some discrepancies in these measurements due to the equipment and solution used.

Like the oil-free case there were other parameters of the system that were monitored, including relative humidity and temperature of both the test chamber and oil reservoir. Oil conductivity was also monitored because the aging of oil causes it to become more conductive. This provided a way to determine when it was necessary to change the oil in the system.

4.4.2 Measurement Results

The data collected for oil-impregnated measurements show similar trends to those exhibited in the oil-free case further confirming that a universal curve does exist. However, a broader range of moisture levels is desired in order to accurately find the universal curve. Figure 4.9 shows values of dielectric properties at 1.82% moisture content for five temperatures.

4.5 Conclusion

Comprehensive experiments relating the dielectric properties of the oil-free pressboard to the temperature and moisture effects have been performed. The results agree with the literature reported results. A dielectric model for biological tissue is adopted here for the cellulose structured pressboard. The universal curve is found by fitting the data to the model. Preliminary measurements with the oil-free pressboard show similar trends.

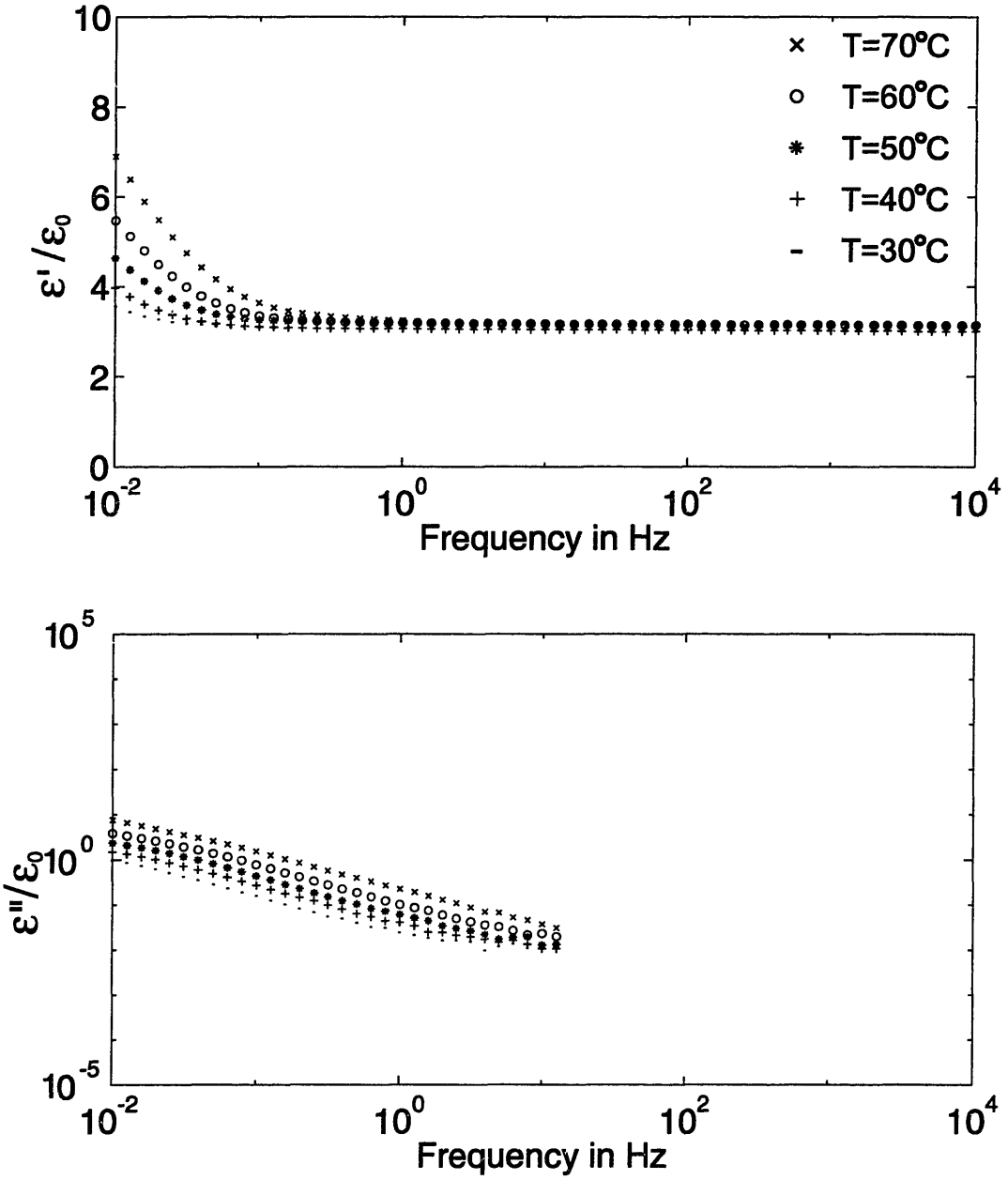

Figure 4.9: Dielectric properties of oil-impregnated pressboard at moisture content 1.82% at five temperatures.

Chapter 5

Sensor Measurements with Early Design

5.1 Measurement Setup

A typical measurement setup for interdigital dielectrometry measurements is shown in Figure 5.1. The sensor is connected to a microprocessor-controlled controller box through an electronic interface circuit. The controller box controls various operating parameters, generates a sinusoidal drive voltage, measures an output voltage from the interface circuitry, and records data. The interface box's main function is to buffer the signal and raise its input impedance. A computer serves as a data acquisition system as well as interface between operator and the controller. The commands sent from computer to the controller can either be manually typed or programmed and run automatically.

5.2 Multi-wavelength Sensor

The earlier design of the three-wavelength sensor by Dr. Philip von Guggenberg [2] is shown in Figure 5.2 . The flexible sensor consists of three sets of electrodes deposited on a common flexible polyimide substrate (Kapton) with wavelength of 1, 2.5, and 5

mm. The sensing electrodes are shielded in the $x-y$ plane by guard electrodes driven by the buffer stage of the interface circuit, and the guard electrodes are shielded by ground electrodes [3]. A thin (5 μm) layer of parylene covers the sensor on both sides to prevent moisture absorption by hydrophilic Kapton. The moisture in the volume of Kapton significantly deteriorates its insulating properties.

For each wavelength, one set of electrodes is driven with a variable frequency AC voltage and a high impedance measurement is made of the induced voltage on the alternate set of interdigitated electrodes. The gain magnitude G and phase ϕ of this floating voltage depend on the permittivity ϵ and electrical conductivity σ of the medium adjacent to the sensor. As described in Chapter 2, with three different penetration depths it is possible to calculate spatial profiles of permittivity and conductivity from the gain and phase of the floating voltage as a function of frequency for each sensor wavelength.

5.3 Lumped Circuit Model

When the lumped parameter representation of the sensor structure is used, the test response is equivalent to voltage gain G and phase ϕ of the RC circuit shown in Figure 5.3. The voltage measured at the sensing electrodes V_S can be expressed in terms of the driven voltage V_D as:

$$\frac{V_S}{V_D} = Ge^{j\phi} = \frac{Y_{12}}{Y_{12} + Y_{20} + j\omega C_L} \tag{5.1}$$

where Y_{12} is the transadmittance between driven and sensing electrodes which primarily reflects the dielectric properties of the test materials, Y_{20} is the admittance between the sensing electrode and the ground, and C_L is the load capacitance of the electronic interface. Y_{20} is primarily due to substrate properties but has a small contribution from the test material due to fringing fields. Moreover,

$$Y_{12} = \frac{j\omega C_p(G_{12} + j\omega C_{12})}{2G_{12} + j\omega(2C_{12} + C_p)}, \tag{5.2}$$

$$Y_{20} = G_{20} + j\omega C_{20}, \tag{5.3}$$

so the complex gain is expressed in terms of equivalent circuit elements as:

$$Ge^{j\phi} = \frac{G_{12} + j\omega C_{12}}{G_{12} + j\omega C_{12} + (G_{20} + j\omega(C_{20} + C_L))\,(2G_{12} + j\omega(2C_{12} + C_p))\,/(j\omega C_p)}. \quad (5.4)$$

In most cases, G_{20} is very small because the substrate is purely capacitive and only a negligible conduction current flows through the testing material and terminates at the ground electrode. We thus neglect G_{20} for simplicity of illustration of the sensor response here. The inversion computer algorithm can account for finite G_{20} if necessary. Setting $G_{20} = 0$, (5.4) becomes

$$Ge^{j\phi} = \frac{G_{12} + j\omega C_{12}}{G_{12}(1 + 2a) + j\omega(C_{12}(1 + 2a) + aC_p)}, \quad (5.5)$$

where $a = (C_{20} + C_L)/C_p$ and is almost a constant approximately independent of test material properties except for fringing field effects. When the material is highly insulating, the circuit is purely a capactive voltage divider and (5.5) simplifies to

$$Ge^{j\phi} = \frac{C_{12}}{C_{12}(1 + 2a) + aC_p}, \quad (5.6)$$

which means a constant gain and zero phase over all frequency. In fact that is the way we test if a sensor is clean by measuring its response in air. A typical measurement of air is shown in Figure 5.4. A contaminated sensor would have significant phase at low frequency.

In general, at high frequency, $\omega C_{12} >> G_{12}$, the capacitive properties of the medium dominates and the response looks like that of air, i.e. gain is constant and phase is zero; at low enough frequency, $G_{12} >> \omega C_{12}$, the medium behaves like a short circuit between the parylene coatings and again the gain is a constant and phase is zero. In-between the gain increases and the phase goes through a valley and back to zero at low frequency. A typical response that goes through the transition is simulated in Figure 5.5. When the medium is more insulating the characteristic curve shifts to the left; when the medium is more conducting, the curve shifts to the right.

The dielectric spectrum of Shell Diala A oil is measured using the interdigital sensor and the sensor response is converted to the dielectric properties shown in Figure 5.6

using the continuum model algorithm developed by previous students [2, 48, 49]. The literature reported relative dielectric constant of oil is 2.2 which is consistent with the estimated value. Oil is a non-dispersive material, i.e. the conductivity does not change with frequency. Since

$$\log(\varepsilon''/\varepsilon_0) = \log(\frac{\sigma}{\omega\varepsilon_0}) = \log(\sigma/\varepsilon_0) - \log(\omega), \tag{5.7}$$

for frequency independent conductivity, the curve of $log(\varepsilon''/\varepsilon_0)$ versus $\log(\omega)$ is a straight line with -1 as slope. The curve fitted to the data by linear regression has good agreement with this.

Shown in Chapter 2, a continuum model of an interdigital sensor provides a closed-form solution for a set of idealized interdigitated electrodes (an infinite array of infinitely long microstrip conductors of zero thickness). A 2D finite-element model such as Ansoft Maxwell allows assumption of finite thickness of the electrodes as in Figure 5.7, allowing for numerical calculation of electric and magnetic fields and associated physical properties.

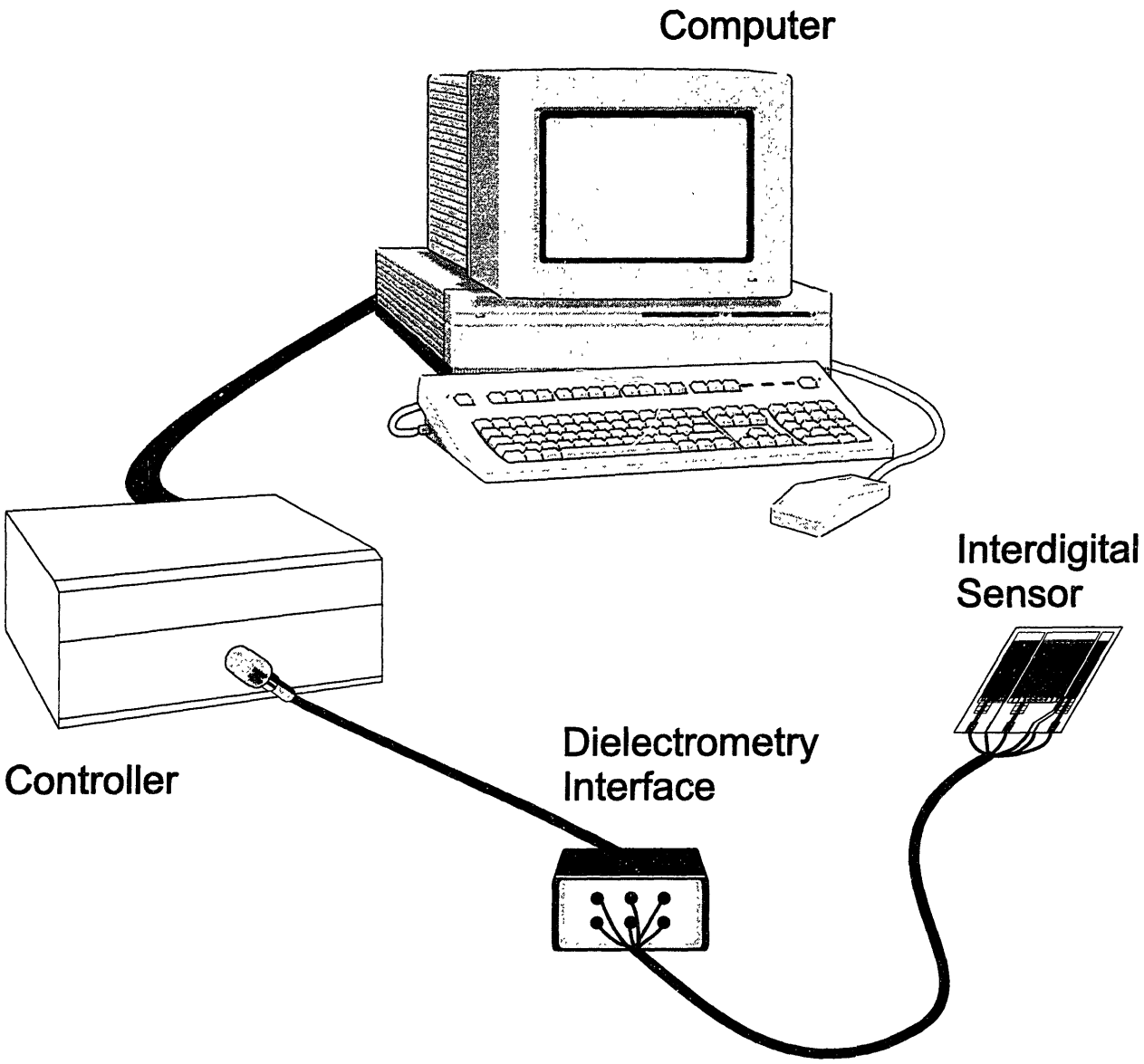

Figure 5.1: General measurement setup using interdigital sensor.

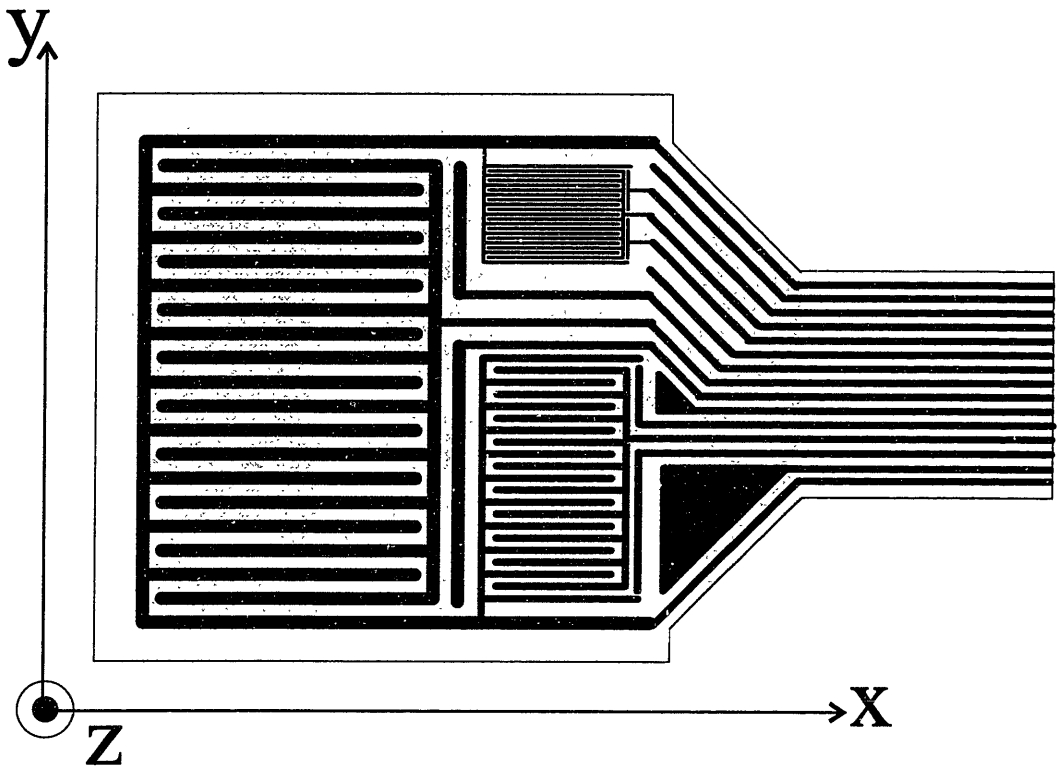

Figure 5.2: Earlier design of the Kapton three-wavelength interdigital sensor [2] (picture by D. E. Schlicker [47]).

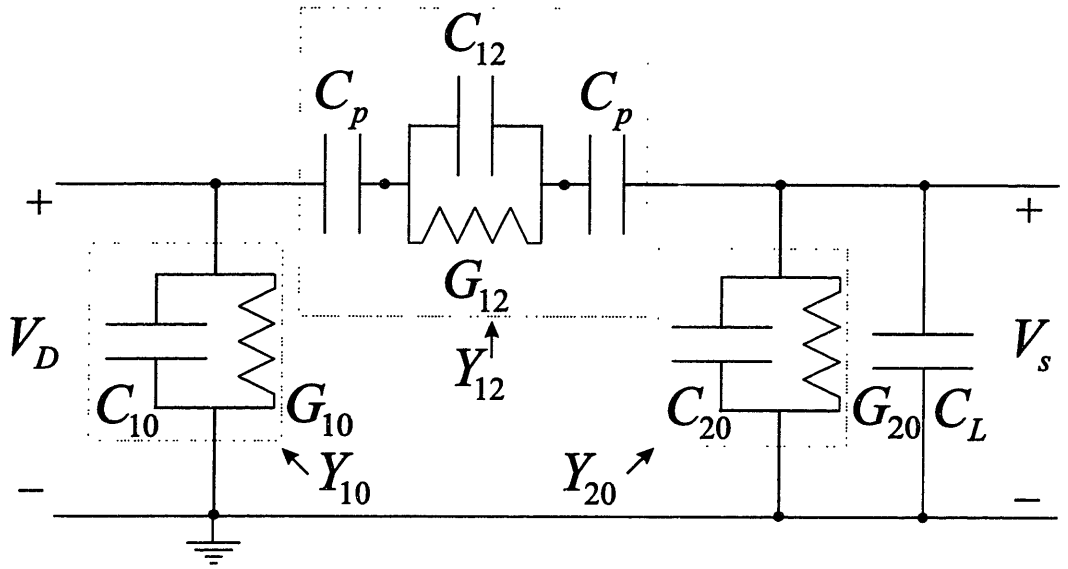

Figure 5.3: The equivalent circuit of the floating-voltage measurement of an interdigital sensor.

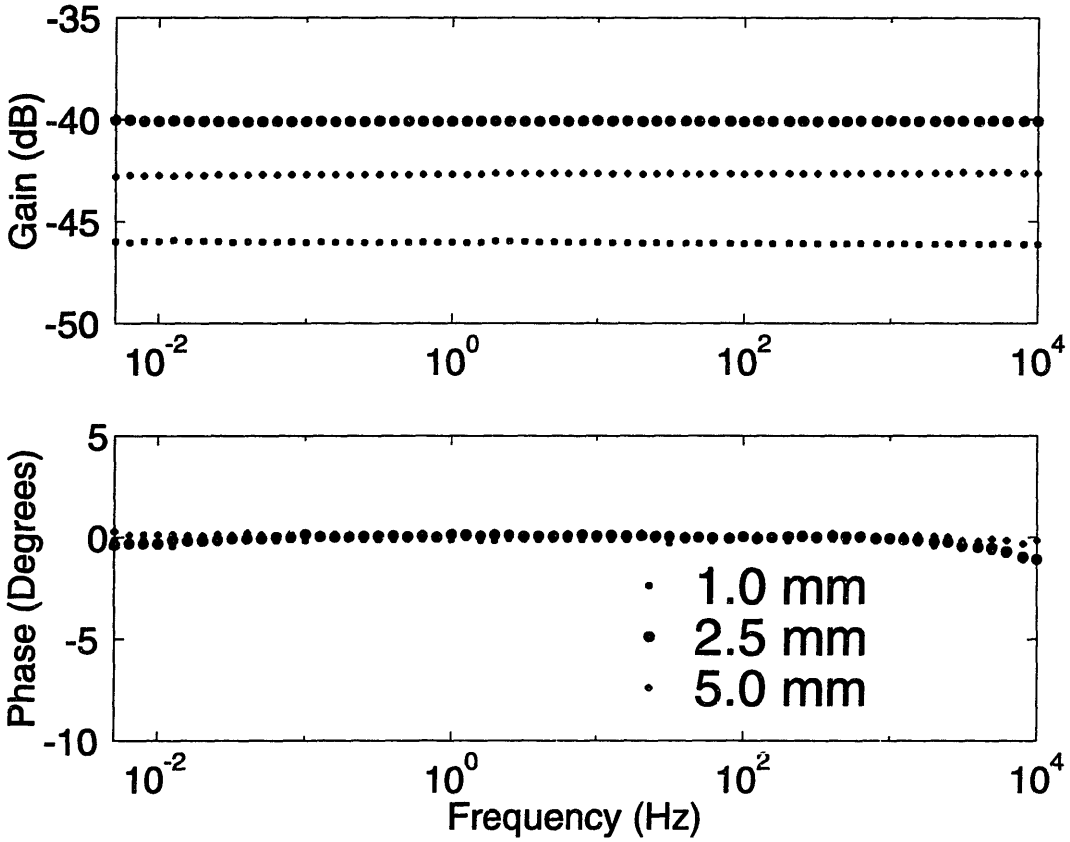

Figure 5.4: Measurement in air using a clean Kapton three-wavelength interdigital sensor of Figure 5.2.

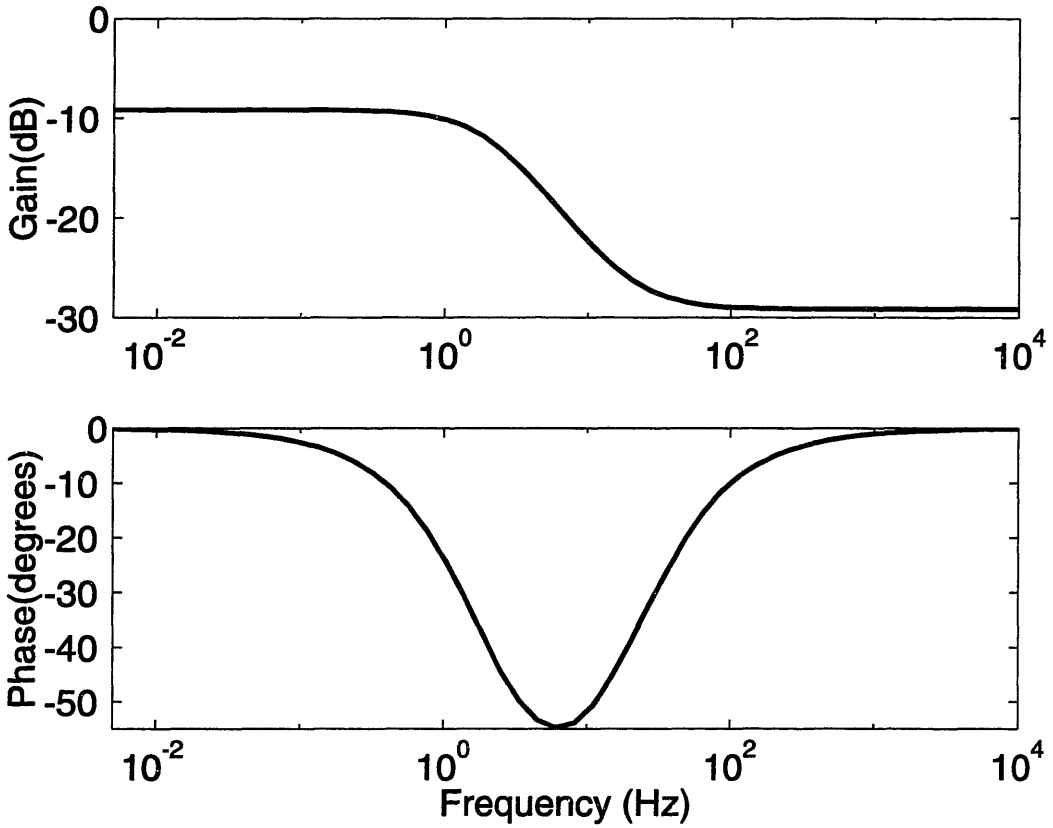

Figure 5.5: Simulated response for the sensor circuitry with $C_p = 110pF$, $C_L = 3pF$, $C_{12} = 4pF$, $G_{12} = 500pS$, and $C_{20} = 100pF$.

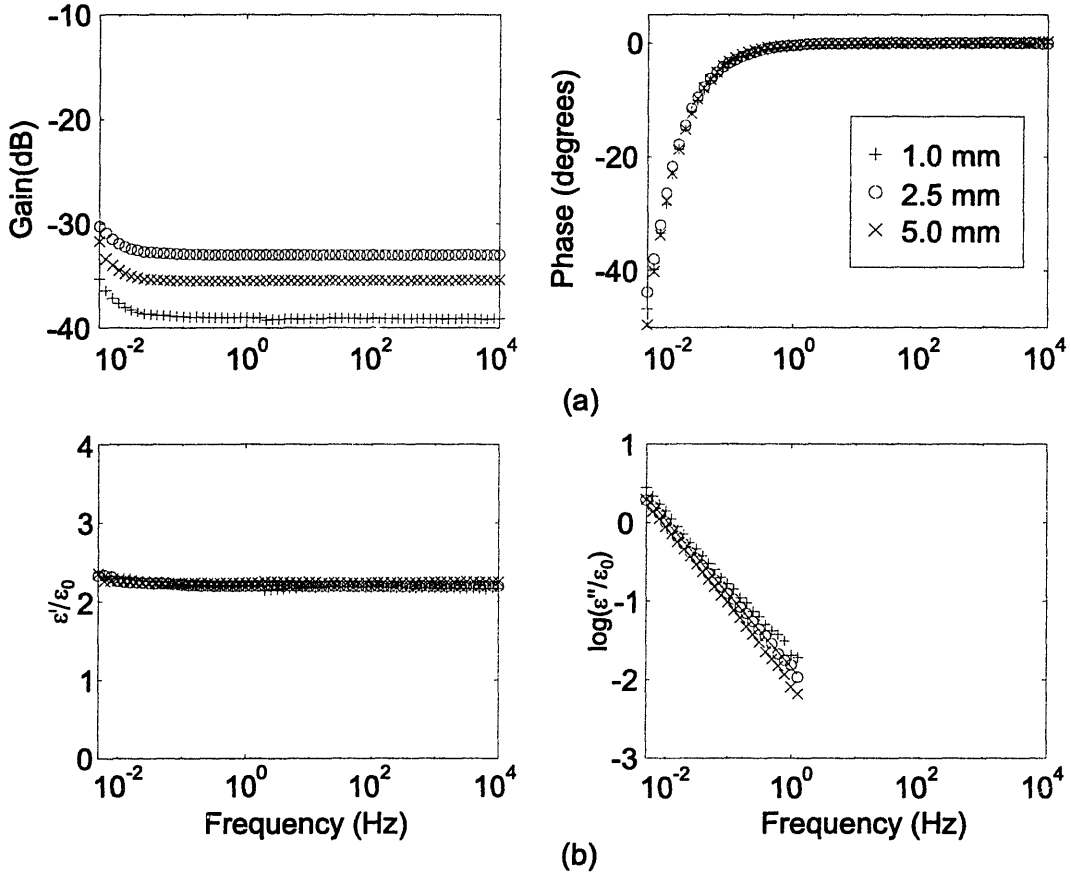

Figure 5.6: (a) Measured sensor response in Shell Diala A oil at room temperature. (b)Estimated dielectric properties of Shell Diala A oil using a continuum model algorithm.

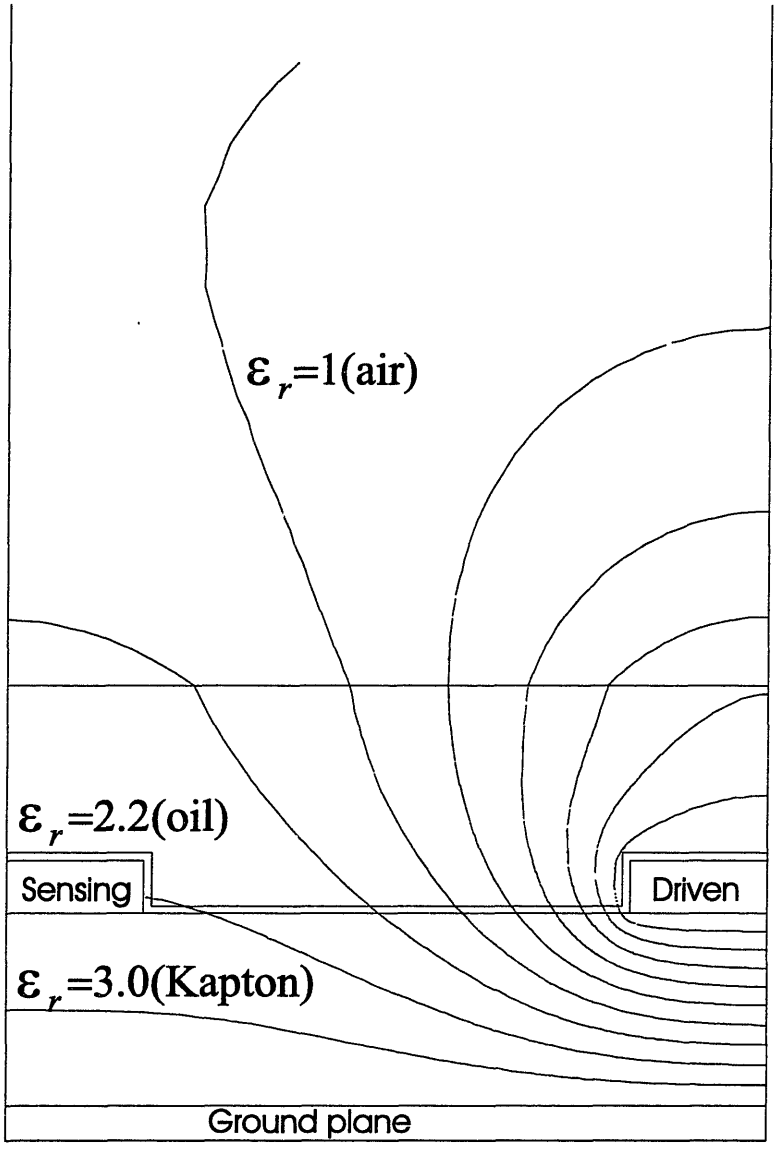

Figure 5.7: Equipotential lines in the half-cell geometry of an 1 mm interdigital sensor with lossless dielectrics. Relative permittivity of parylene coating is ϵ_r=3.05. The driven electrode (right) is at 1 V peak potential, the sensing electrode (left) is at 0.2 V potential, and the ground plane is at 0 V [50].

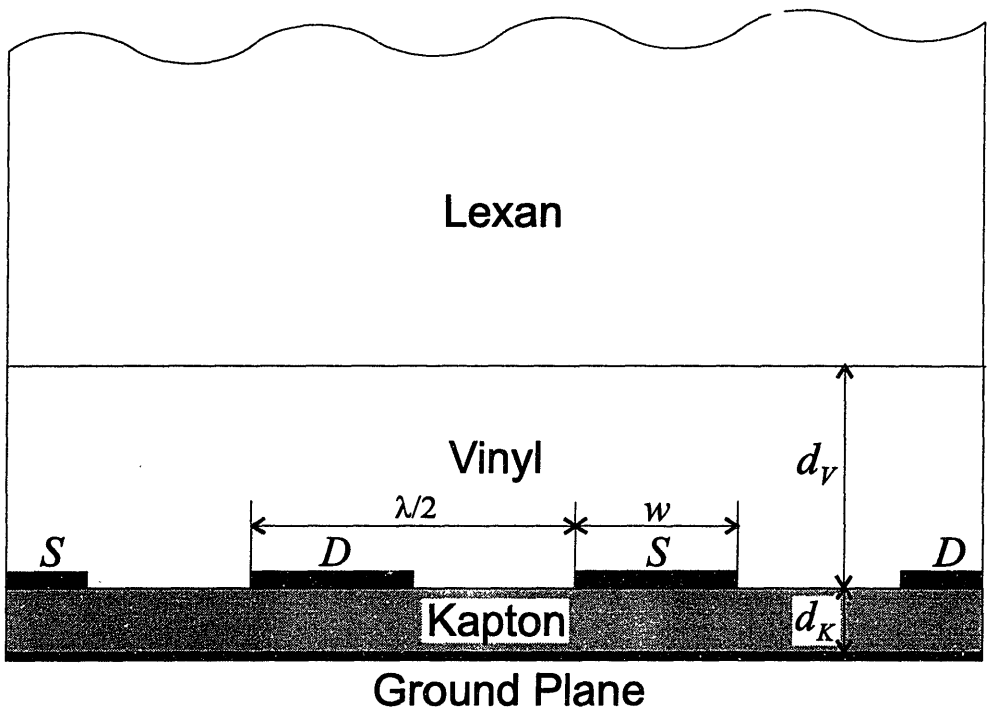

Figure 5.8: The cross-section of the interdigital sensor with two layers of materials above it.

5.4 Experimental Verification of the Penetration Depth

The goal of the series of experiments presented in this section which were conducted jointly with Alexander Mamishev is to actually test the dependence of the sensor response on the thickness of the material above the sensor. Figure 5.8 depicts the cross-section of the experimental setup. Two materials with known properties form a two-layer medium. When the thickness of the lower material is reduced, the interlayer boundary moves down, and the influence of the upper material increases. The upper material is thick enough to be considered infinitely thick.

Two commercially available insulating polymers, monolithic pieces of 1/2 inch thick Lexan (GE polycarbonate brand name) and 0.19 mm thick thin-filmed samples of

vinyl, are used. The thin film enables us to control the thickness of the test sample by changing the number of sheets of vinyl. In order to press the whole structure together and provide a good contact between the materials, a heavy slab of lead was positioned on top of the test cell. In general, a highly conductive metal would strongly affect the distribution of the electric field in the studied region, unless it is sufficiently far from the strong field region. It can be seen from (2.1) that the electric field excited by the sensor dies away exponentially with the vertical coordinate with the penetration depth of $\lambda/2\pi$. Let us denote the distance at which the electric field potential reduces by one order of magnitude as an effective penetration depth of our sensor. The total thickness of Lexan was 17 mm, which is about 10 times the effective penetration depth of the 5mm longest wavelength.

The schematic view of the experimental setup in Figure 5.8 shows one and a half periods of the interdigitated electrodes. The label D refers to the driven electrode and S refers to the sensing electrode. A one volt peak sinusoidal voltage was applied to the driven electrode. The voltage magnitude and phase of the sensing electrode was measured and recorded. As the distance d_v becomes smaller the influence of dielectric properties of the Lexan becomes stronger which is illustrated below.

The dielectric permittivity of the materials had been predetermined using a parallel-plate capacitor of known geometrical dimensions with

$$\varepsilon_a = \frac{\pi C}{L + W + W\ln(\frac{\pi L}{d}) + L\ln(\frac{\pi W}{d}) + \frac{\pi LW}{d}} \tag{5.8}$$

where L and W are the length and width of the parallel-plate capacitor, d is the distance between the plates, and C is its capacitance. Equation (5.8) takes into account the fringing fields of a parallel-plate capacitor and is derived using a Schwarz-Christoffel transformation.

Using (5.8) with guarded parallel plate measurements, the relative dielectric permittivity of the polycarbonate Lexan sheet has been estimated to be equal to 2.6, and that of vinyl film is equal to 3.8. The conductivity of Lexan is on the order of 10^{-15} S/m and in our frequency range its effect is negligible. The conductivity of vinyl is

on the order of 10^{-9} S/m, and the vinyl appears to be a dispersive material. Only a qualitative discussion of conductivity effects is given in this section.

As discussed above, according to the idealized model, the effective penetration depth of an interdigital sensor must be about one-fifth of the sensor's spatial wavelength λ. In our case, the metallization ratio is close to 0.5 for 5 mm and 2.5 mm wavelengths, and it is about 0.36 for the 1 mm wavelength. The results of a high frequency scan at 1 kHz are shown in Figure 5.9 for all three wavelengths. A good correspondence with theory can be observed. The 1 mm wavelength measurements do not respond to the changes of the thickness because in almost all cases the thickness exceeds one-third of 1 mm. The response of the 2.5 mm structure flattens off at about 0.7 mm, and for 5 mm at about 1.2 mm. It should be noted, however, that since distinction must be made between levels of attenuation which differ only by 1 or 2 dB, the sensitivity to the error in such measurements is relatively high. Of course, if the difference between the values of the dielectric permittivity of the two materials was larger, the effect of the movement of the interlayer boundary would have been more observable.

As seen from Figure 5.9, given the geometrical dimensions of this setup, the measurements with the 5 mm wavelength are the most descriptive in terms of sensitivity of the sensor to the position of the interlayer boundary. The results of the frequency scans for setups with varying thickness are shown in Figure 5.10 and Figure 5.11.

At high frequencies, the gain is approximately equal to the ratio of the capacitances in (5.5). Since the dielectric permittivity of vinyl is higher than that of Lexan, the equivalent capacitance measured by the sensor becomes smaller as the distance d_v decreases. Thus, the gain shifts towards the flat gain of the non-conductive Lexan-insulated interdigital capacitor. As the frequency is lowered, the slightly conductive vinyl makes the test cell behave like a first order system with one pole and one zero in the transfer function. It has a minimum in the phase-frequency curve whose position is determined by the location of the pole and zero (see Figure 5.11). It should be noted that depending on the ratio of interelectrode capacitances and conductances, and the load capacitance, the phase minimum may shift either to the left or to the right, since

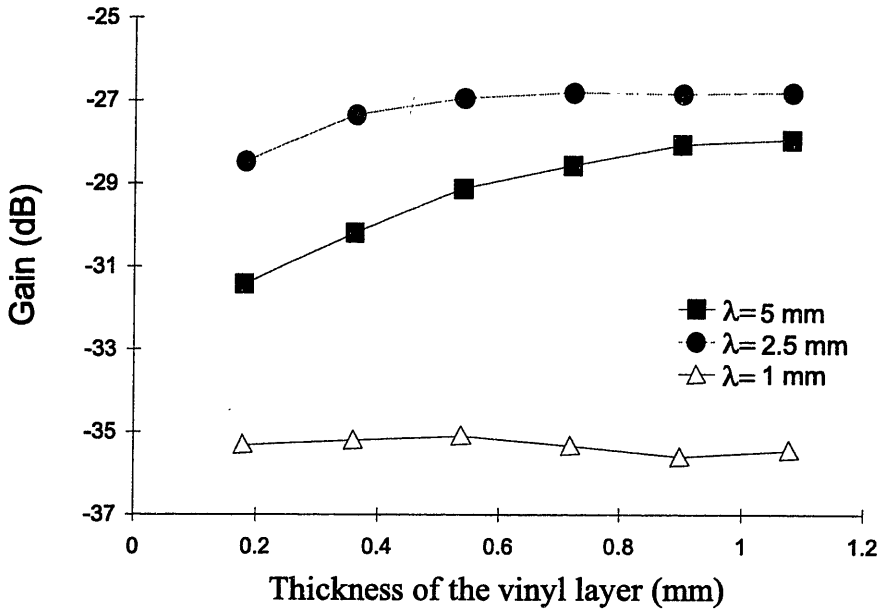

Figure 5.9: Experimental estimation of the effective penetration depth of a three-wavelength sensor by varying the thickness of the vinyl layer adjacent to sensor [51].

the conductivity of Lexan is lower, and the dielectric permittivity is lower than that of vinyl.

In the curves shown in Figure 5.9, the small negative phase-shift is not considered, primarily because it does not affect the overall estimation of the effective penetration depth. In the graphs shown in Figure 5.12, the gain, measured at the frequency of 10 kHz (the right-most data points in Figure 5.10, curve 1), is compared with the gain calculated with a finite-element electric and magnetic field calculation package Ansoft (curve 2). The irregularity of the shape of the experimental curve 1 is mostly due to the A/D conversion limitations at 10-kHz. The highest frequency of the sweep had been used to reduce effects of the conductivity on the output data.

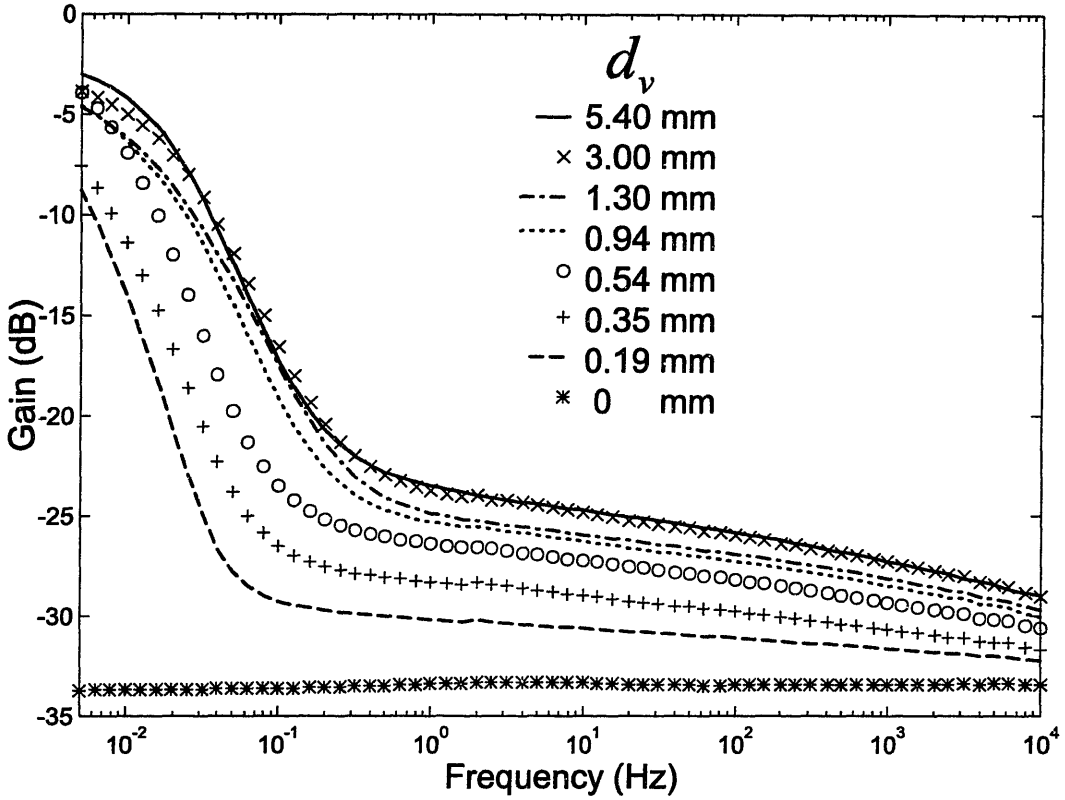

Figure 5.10: Response of the sensor's gain to the movement of the interlayer boundary, d_v.

5.5 Moisture Dynamics Experiments

5.5.1 Oil-Free Pressboard

Tests were performed using 3mm thick oil-free Hi-Val pressboard at room temperature under vacuum so that the moisture diffused out of the pressboard. Before vacuum, a full frequency scan was taken under equilibrium at 13% relative humidity. Then the chamber is vacuumed down to 2 torr at room temperature and kept at this level for all measurements shown in Figure 5.13. As the moisture leaves the pressboard, it becomes more insulating and the frequency spectrum shifts to the left.

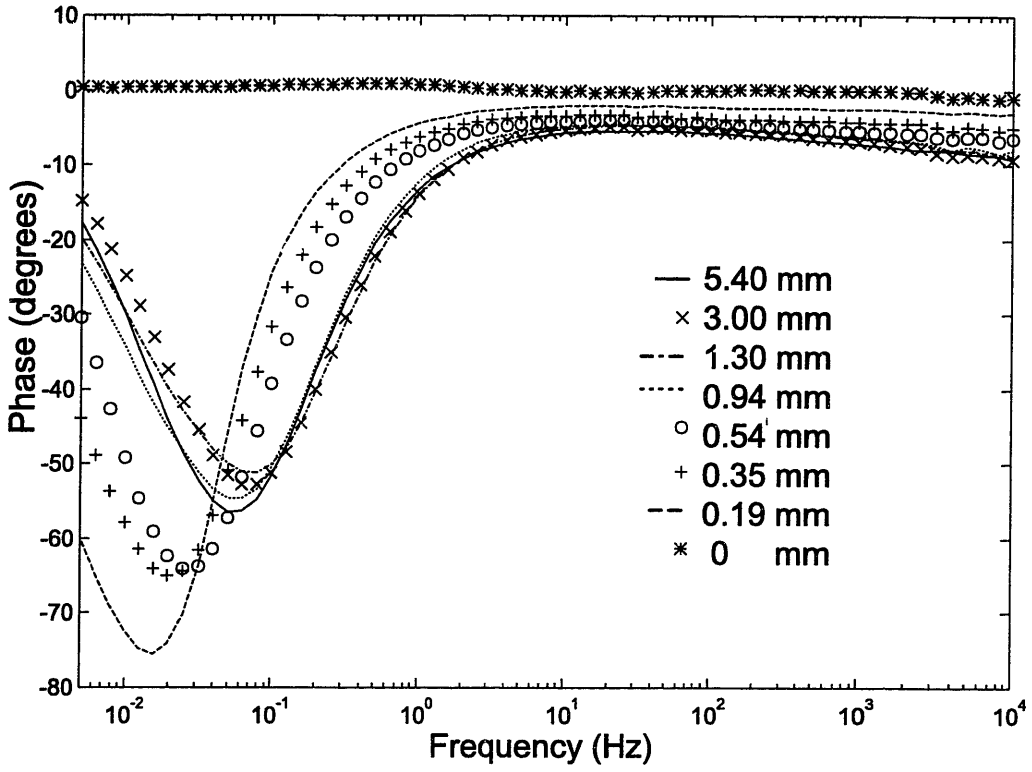

Figure 5.11: Response of the sensor's phase to the movement of the interlayer boundary, d_v.

5.5.2 Oil-Impregnated Pressboard

To simulate the commercial impregnation procedure for transformers, two pieces of oil-free Hi-Val pressboard (2 mm thick) were dried under vacuum for 24 hours and were impregnated with Shell Diala A oil at 70°C. A full frequency scan (0.005 to 10,000 Hz) was measured under equilibrium in ambient air at 70°C. Using the parameter estimation program for homogeneous materials with the continuum model that relates measured gain and phase to complex permittivity, we obtain the dielectric spectra in Figure 5.14. The three wavelengths approximately give the same value indicating that the moisture distribution is essentially uniform throughout the pressboard. The relative permittivity at high frequency is about 3.8 which is consistent with manufacture's specifications. The difference of ϵ' at low frequency may be due to the presence of the

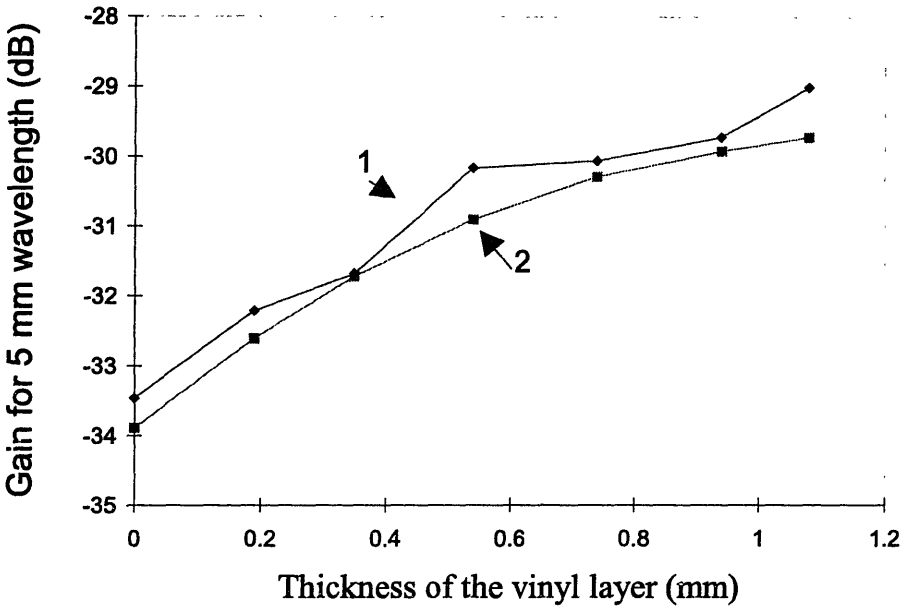

Figure 5.12: Comparison of the measured (1) and theoretical ($\varepsilon_r = 2.6$ for Lexan and $\varepsilon_r = 3.8$ for vinyl) (2) response of interdigital sensor ($\lambda = 5$ mm) at 10 kHz.

electrical double layer. By linear regression, the slope of the ϵ'' curve is -0.7, indicating that it is dispersive , i.e., the conductivity changes with frequency. This verifies the non-ohmic property discussed in [52]. As discussed earlier in this Chapter, a constant conductivity would have a slope of $log(\epsilon'')$ versus $log(f)$ of -1.

More quantitative analysis of the diffusion process is given in the next two chapters.

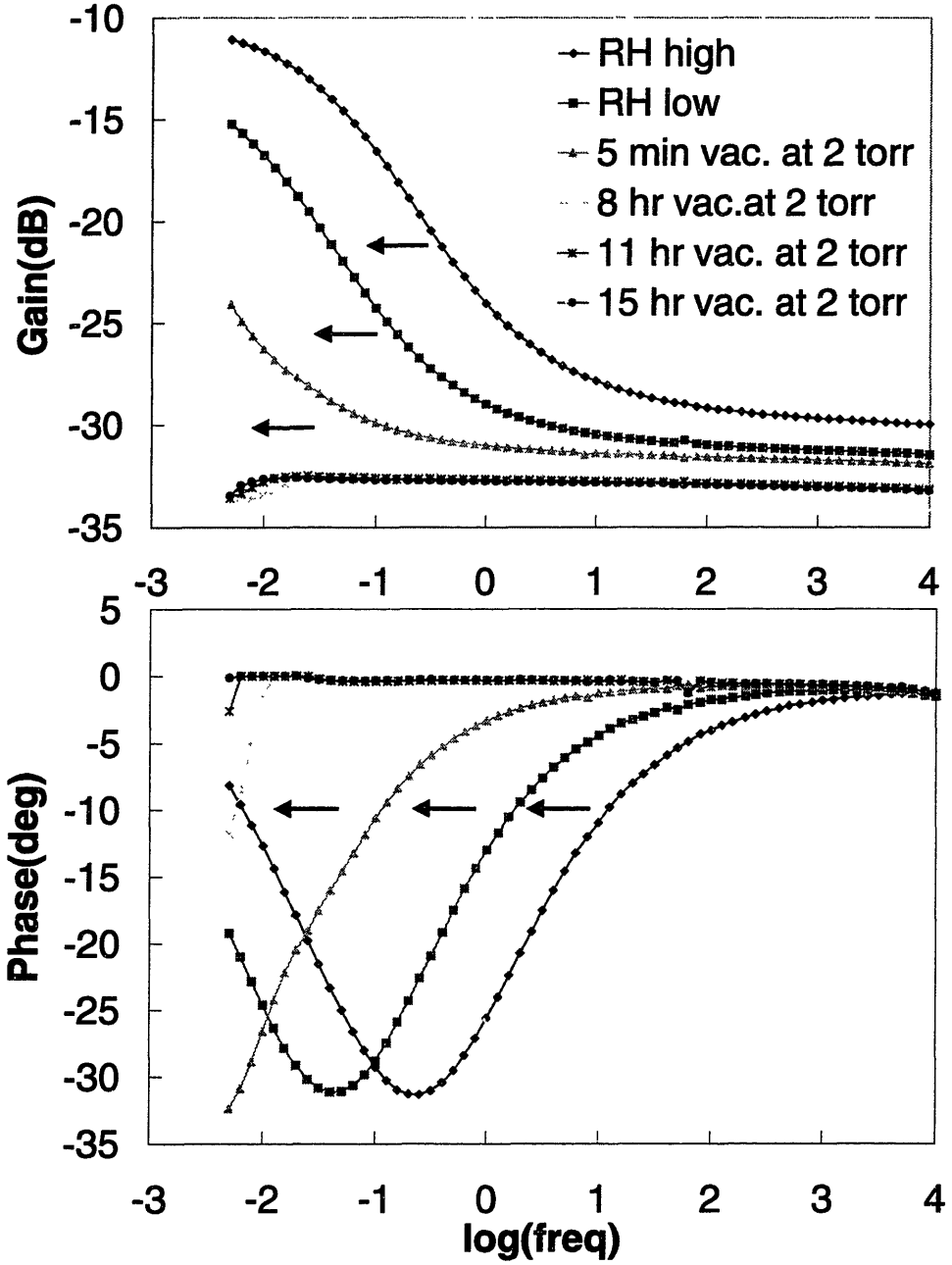

Figure 5.13: The measured response of the 5.0 mm wavelength when the moisture leaves the pressboard. As the moisture is reduced, the pressboard is more insulating and the curves shift to the left.

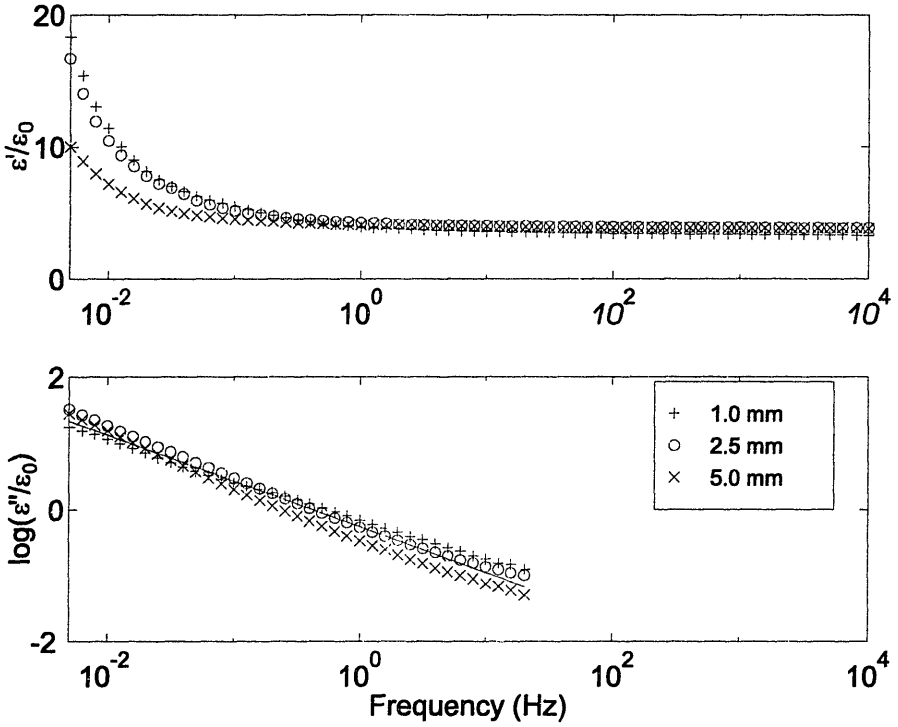

Figure 5.14: Dielectric spectrum for 2 mm thick oil-impregnated EHV-Weidmann Hi-Val pressboard at ambient air in equilibrium at 70°C.

Chapter 6

Measurements of Pressboard using Improved Sensor

6.1 New Sensor Design

The idealized model for which the closed form expression for the electrodes' electric field exists requires the electrodes be an infinitely long and wide array of infinitely thin microstrips placed on the surface of the insulating substrate. The thickness of the electrodes (35 μm for the earlier design), the finite length (25 mm) and finite number of the fingers (10 for each wavelength), the capacitance of the leads of the electrodes to ground and to each other, and the metallization ratio (described as ratio of the area covered with copper to the total area of the sensor, designed to be 50%) are the most important contributors to the discrepancies between the theoretical model and the real measurement data.

Experiments and analysis performed over the past few years led to development of an improved design of a three-wavelength sensor. The sensor shown in Figure 6.1 is free of some of the problems associated with the previous design. In particular, employment of a separate guard plane for each wavelength, minimization of cross-coupling between the leads and the sets of interdigital electrodes themselves, significant reduction of end effects and parasitic capacitances, change of insulating substrate from hydrophilic

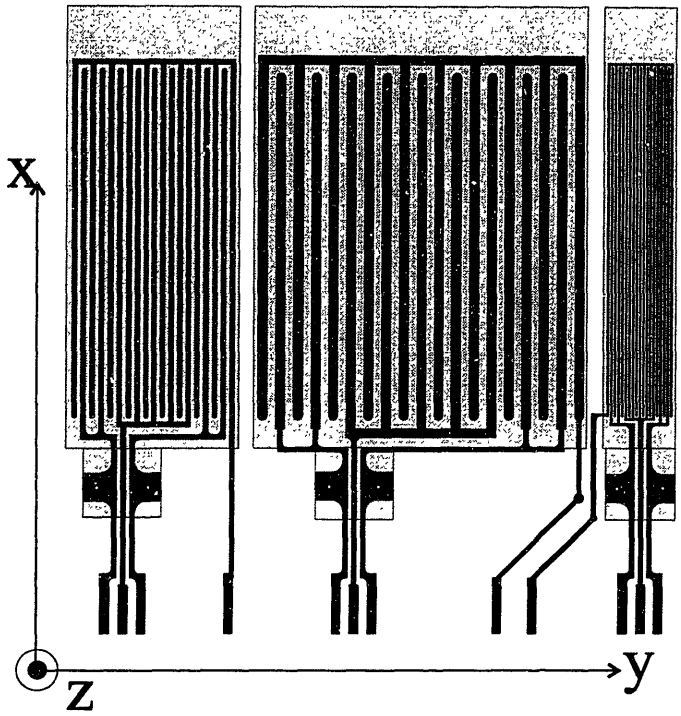

Figure 6.1: The improved design of the Teflon three-wavelength sensor [53].

Kapton to hydrophobic Teflon are the most important features of this improved design.

6.2 New Interface Box

As discussed in Chapter 5, the previous Kapton sensor design measures the induced voltage on the sensing electrodes. We call this a floating voltage measurement. Similarly the sensing electrodes can also be virtually grounded by external circuitry and the current that flows into the sensing electrodes can be measured. This is called a short-circuit measurement. A new interface box was designed and built for short-circuit measurements with the following new features:

- 10-volt driving signal to provide high signal-to-noise ratio;
- allow each wavelength to run individually to avoid cross-coupling;
- uses the short circuit measurement technique which increases the resolution, simplifies the equivalent circuitry, and is more robust to noise.

To illustrate the cross-coupling effects, we compare measurements taken with three

wavelengths driven together and individually for pressboard. The results shown in Figure 6.2 clearly indicate interference from adjacent wavelength signals. The difference is more significant at low frequencies when conduction dominates.

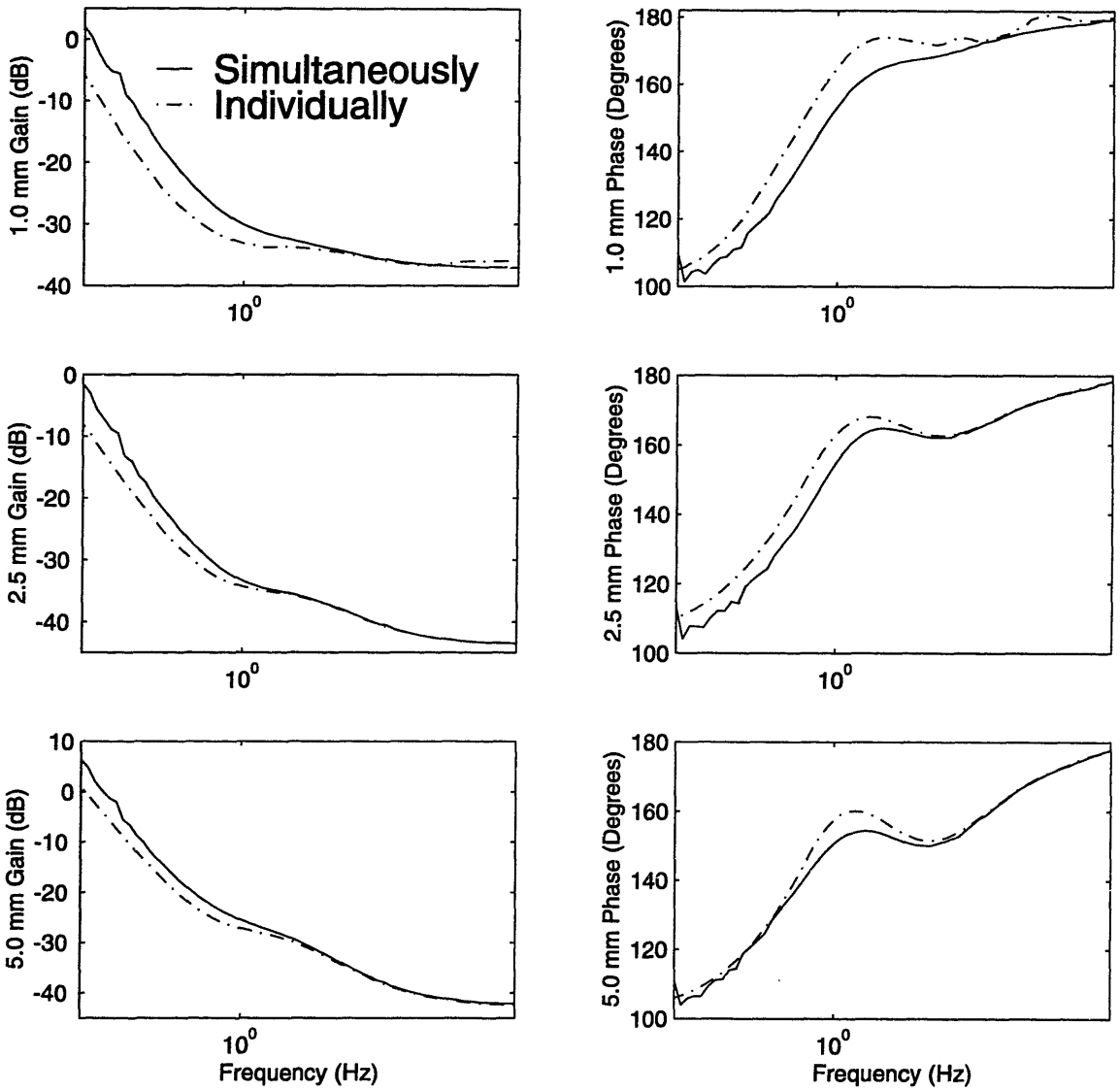

Figure 6.2: The effects of cross-coupling in pressboard measurements.

6.3 Experimental Setup

The experimental system shown in Figure 6.3 is designed and constructed for diffusion measurements using interdigital dielectrometry sensors. It is built inside a stainless steel hood for better shielding, support, and protection. The testing chamber is made of a Varian 8" O.D. stainless steel vacuum nipple. The reservoir is made of Pyrex 250 mm I.D. dessicator. Both of them have a volume of about 6500 ml. The larger volume of oil provides better stability and accuracy. There are two side viewing ports for monitoring. Since the top needs to be taken apart often, we want to disconnect as few parts on the top as possible. The temperature probe and two outlets are transferred to the bottom flange. The vacuum port is combined with the Harley moisture meter and it is connected to the top by the Swagelok quick connector.

The comprehensive plumbing system allows a variety of circulation, transport, and processing of the oil in the reservoir and testing chamber. The temperature, vacuum, and relative humidity of the chamber are well monitored and controlled. A conductivity cell is incorporated to measure the complex permittivity of the oil. This provides more information for dielectrometry measurements of pressboard using the interdigital sensor.

The three-wavelength sensor testing structure in Figure 6.4 is inside the chamber and includes two back to back sensors to allow simultaneous measurement of two samples. The porous Teflon and aluminum plates squeeze the whole structure, and at the same time allow maximum mass-transfer between the test samples and the surrounding environment.

The SMA hermetic seal feed-through from Pasternack Enterprises keeps the experiment chamber vacuum and pressure tight while getting the electrical signal to the interface box.

A new fixture for holding the connecting wires from the sensor is designed to allow use of rigid coaxial cables which provide better mechanical stability and signal quality.

The equivalent circuitry for short-circuit measurements is shown in Figure 6.5 with

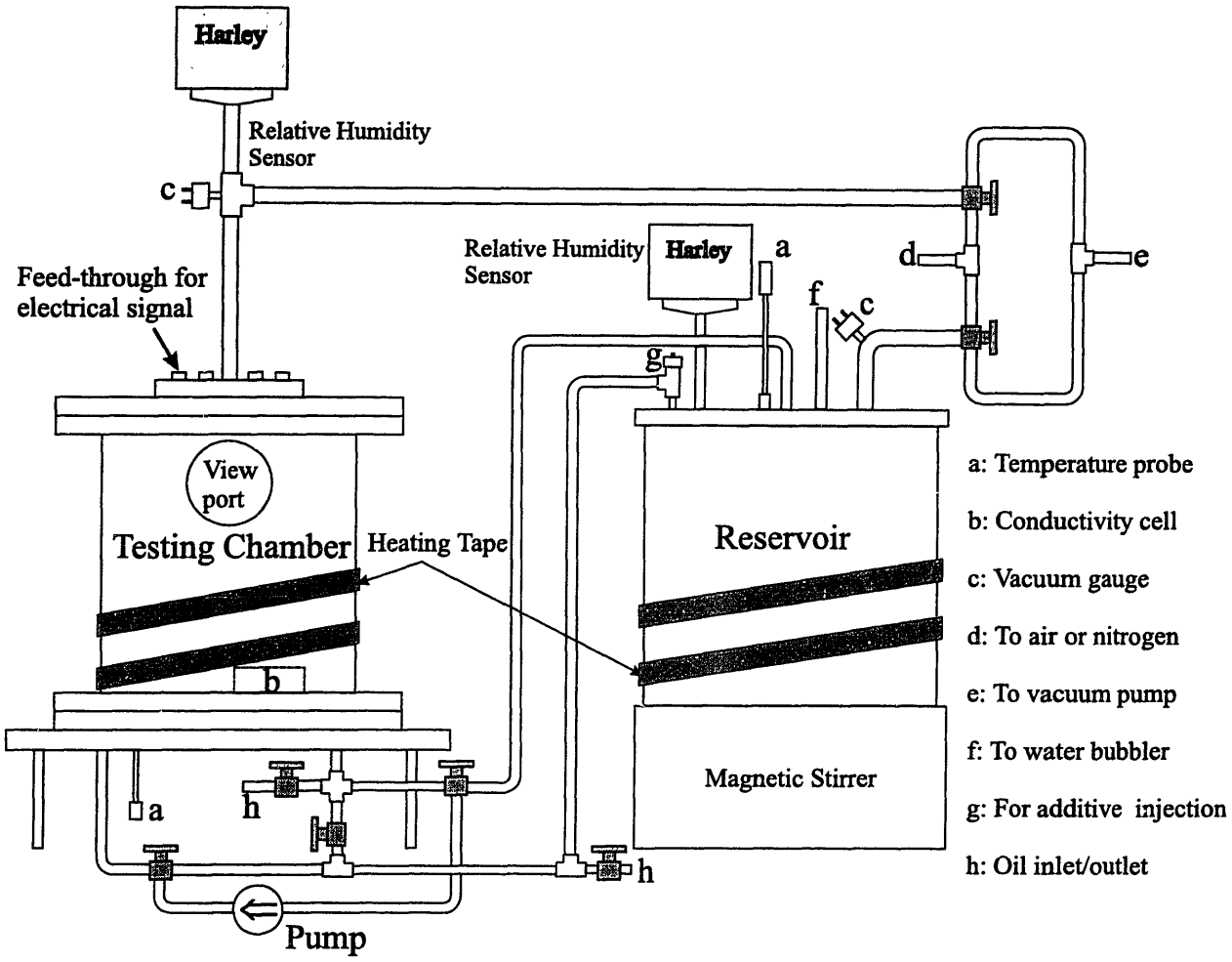

Figure 6.3: Bench-top apparatus for diffusion process using dielectrometry measurements.

sensing voltage $V_S = 0$, and the measured complex gain for output voltage V_O and driving voltage V_D in terms of equivalent circuit elements is:

$$\hat{G} = \frac{V_O}{V_D} = -\frac{G_{12} + j\omega C_{12}}{j\omega C_F} \tag{6.1}$$

where G_{12} is the transconductance and C_{12} is the transcapacitance between the sensing and driving electrodes, and C_F is the known feedback capacitor in the interface circuitry.

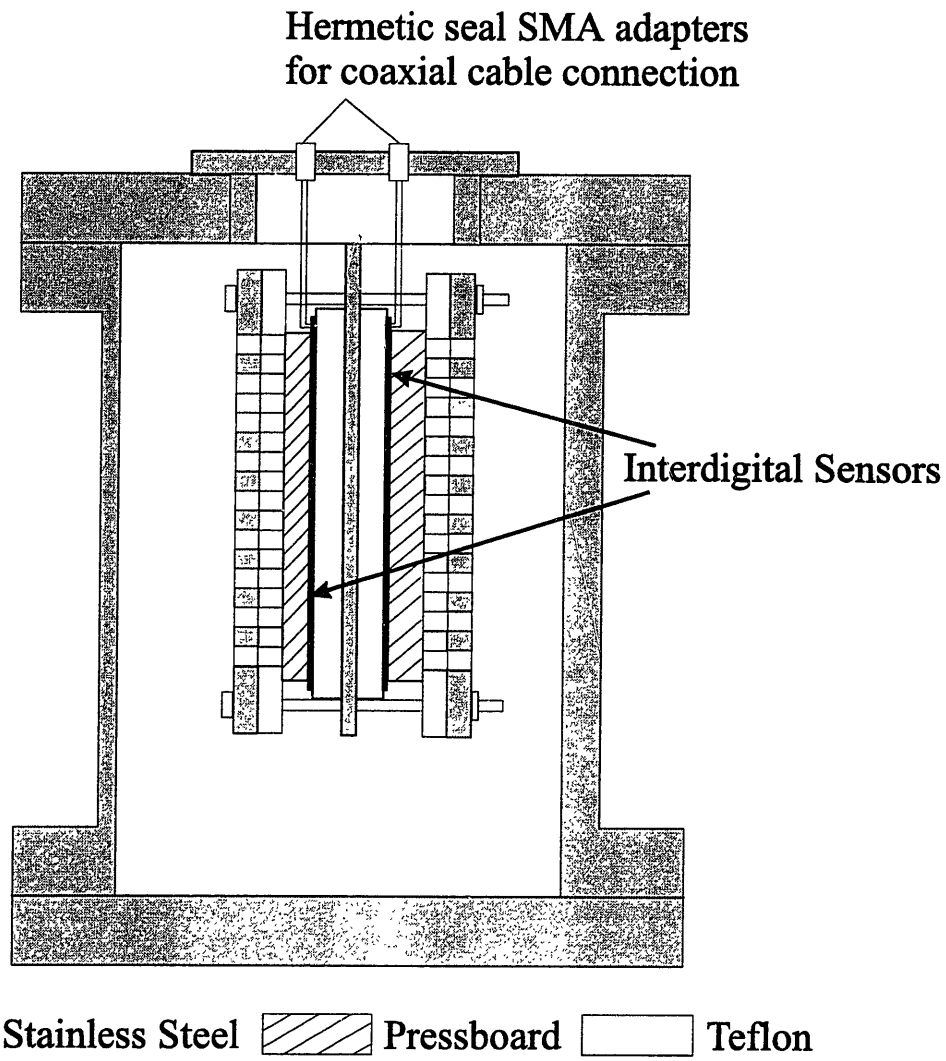

Figure 6.4: Test structure simultaneously using a pair of three-wavelength sensors in laboratory bench-top measurements.

6.4 Experiment Description

Many tests have been performed for both oil-free and oil-impregnated pressboard under various temperature and moisture conditions. Only representative data using the new sensor, new interface circuitry and new experimental system are presented here.

As shown in Figure 6.4 for the test structure, the interdigital sensor is attached to one side of the pressboard, whereas the other side of the pressboard is exposed to ambient conditions through a perforated steel plate. The four side edges of the pressboard sample are sealed with silicon glue to only allow one dimensional diffusion

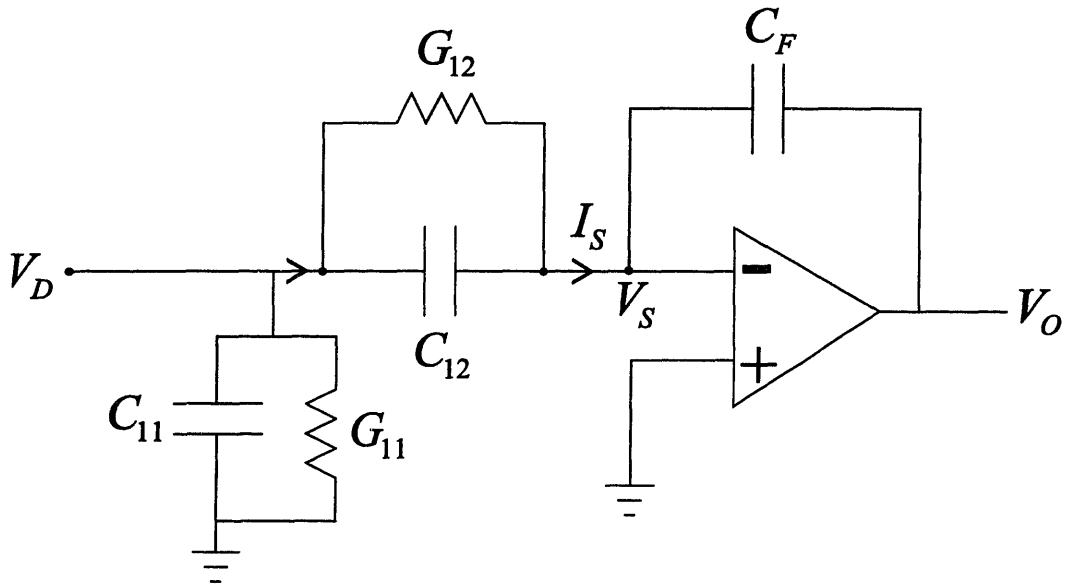

Figure 6.5: Equivalent circuitry of short-circuit measurement.

transverse to the pressboard surface. The test sandwich structure is placed in a vacuum-tight chamber whose temperature and moisture can be monitored and controlled as shown in Figure 6.3.

The tests were performed at five temperatures: 30, 40, 50, 60, and 70°C. Hi-Val pressboard, manufactured by EHV-Weidmann Industries, Inc., is used in all experiments. The samples are either 1.0 mm or 1.5 mm thick. At each constant temperature, the oil-free pressboard was first vacuum-dried for over 24 hours. This gives a uniform zero initial moisture distribution. The moisture diffusion process starts by bubbling in a constant flow of moist air.

The signals from the sensing electrode were recorded at three frequencies: 0.1 Hz, 1 Hz, and 10 Hz. A complete dielectric spectroscopy sweep from 0.005 Hz to 10 kHz is also performed at the beginning and end of each experiment when the pressboard sample is in thermal and moisture equilibrium.

6.5 Effects of Pressboard Thickness

According to the diffusion equation with constant diffusion coefficient D

$$\frac{\partial C}{\partial t} = D\frac{\partial^2 C}{\partial x^2}, \tag{6.2}$$

the diffusion time constant for moisture diffusing from one side of the pressboard is

$$\tau = \frac{4d^2}{\pi^2 D}, \tag{6.3}$$

where d is the thickness of pressboard. It is proportional to the square of the thickness of the pressboard. The diffusion time constant of an 1.5 mm thick pressboard should be 2.25 times that of an 1.0 mm thick pressboard.

Experiments are carried out for moisture diffusion in 1.0 mm and 1.5 mm Hi-Val oil-free pressboard by bubbling moist air. Direct measurement results of the gain and phase are shown in Figure 6.6 for the 1.0 mm thick sample. It takes about 21 hours for the 1.0 mm piece to reach equilibrium, so that it should take about 47 hours for the 1.5 mm piece to reach the same equilibrium.

The calculated transcapacitance and transconductance shown in Figure 6.7 confirm the theoretical prediction of the diffusion time constant: it takes about 50 hours for the 1.5 mm sample to reach the equilibrium. The spatial resolution of the three-wavelength sensor is demonstrated by the delay in different wavelengths, i.e. the 5.0 mm wavelength responds to the increase of the moisture first and the 1.0 mm detects moisture last. Each signal follows approximately the same pattern governed by the diffusion dynamics. After a small initial delay, the signal grows at a high rate, after which it flattens off, indicating the end of the diffusion process experiment to the equilibrium steady state. The 5.0 mm wavelength signal flattens off first because this wavelength reflects an average value of moisture of the entire pressboard thickness whereas the 1.0 mm measurement flattens off the last because within its small penetration depth the diffusion process is still going on.

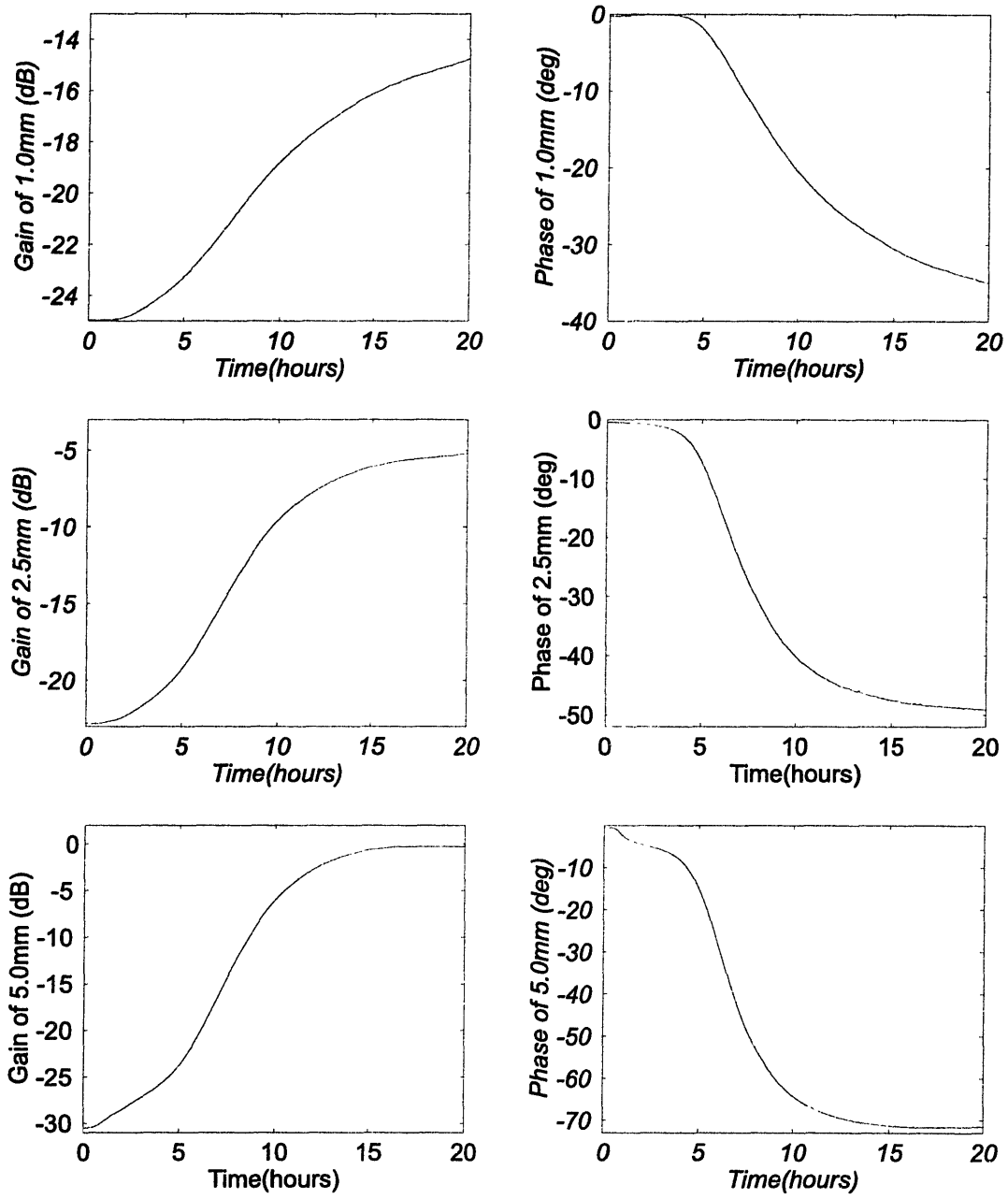

Figure 6.6: The measured Gain and Phase change of the three-wavelength sensor for 1.0 mm oil-free pressboard under wetting process.

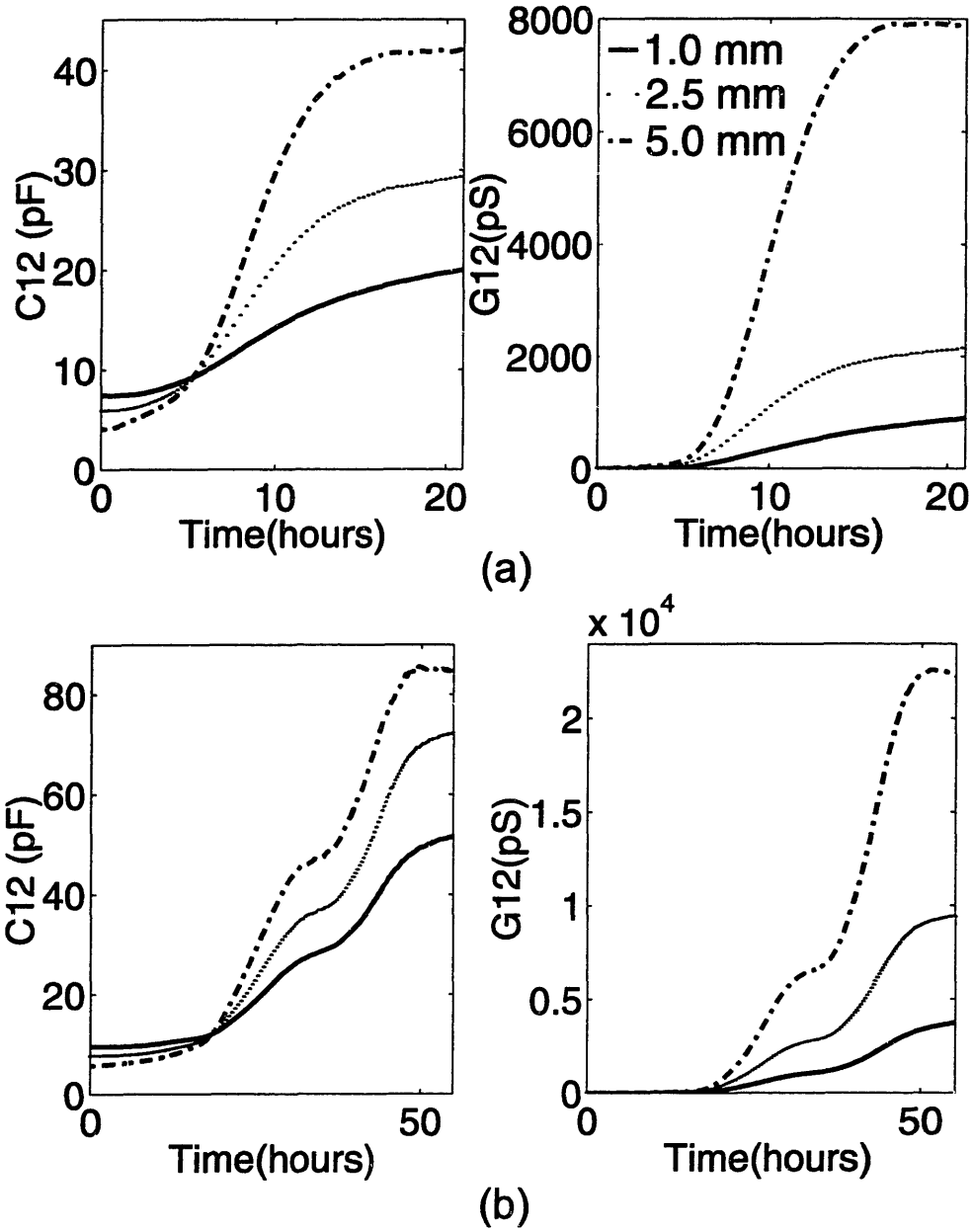

Figure 6.7: The transcapacitance and transconductance of the three-wavelength sensor oil-free pressboard under wetting process at f=10Hz and 30°C.(a) 1.0 mm pressboard (b) 1.5 mm pressboard.

6.6 Temperature Effects

As described in Chapter 3, earlier empirical work has used a diffusion coefficient as a function of temperature and moisture concentration:

$$D(C,T) = D_0 e^{kC+E_a(1/T_0-1/T)}, \tag{6.4}$$

where D_0, $k = 0.5$, E_a, and T_0 are constants, C is the moisture concentration in weight percent per unit weight dry cellulose, and T is the absolute Kelvin temperature. With an increase of T, the diffusion coefficient increases.

Moisture diffusion into the 1.5 mm thick Hi-Val oil-free pressboard is measured at different temperatures. Shown in Figure 6.8, with an increase in the temperature, the diffusion process becomes faster as indicated by the faster increase of the transconductance.

The relative humidity of ambient air of each test is shown in Figure 6.9. With the increase of temperature, the ambient relative humidity decreases. This is because the moist air bubbled into the test chamber has the same water vapor pressure for all temperatures whereas the saturation water vapor pressure increases with temperature.

The quantitative analysis of the temperature dependence of the moisture diffusion coefficient is given in Chapter 7.

6.7 Negative Conductance

From the measured gain and phase, the transcapacitance C_{12} and transconductance G_{12} are calculated from the lumped element circuit in Figure 6.5. For some data, the transconductance turns out to be negative. It looks nonphysical intuitively, but if we take a second look at the equivalent circuit, there are many possible distributed element circuit combinations that make it negative.

Figure 6.10 shows one distributed element model of the measured materials. The

equivalent conductance G_{12} in terms of distributed elements is

$$G_{12} = \frac{2G_1(G_1^2 + \omega^2 C_1(C_1 + C_2)) + G_2(G_1^2 - \omega^2 C_1^2)}{(2G_1 + G_2)^2 + \omega^2(2C_1 + C_2)^2}. \tag{6.5}$$

So when the last term in the numerator in (6.5) is negative and is greater in magnitude than the sum of all the positive terms, G_{12} could be negative.

Another model is shown in Figure 6.11 for which the corresponding G_{12} is

$$G_{12} = \frac{G_1\left[G_1^2(3G_1^2 - \omega^2 C_2^2 + 6\omega^2 C_1^2 + 8\omega^2 C_1 C_2) + \omega^4 C_1^2\left(3C_2^2 + 3C_1^2 + 8C_1 C_2\right)\right]}{\left(3G_1^2 - \omega^2(C_2^2 + 3C_1^2 + 4C_1 C_2)\right)^2 + 4\omega^2 G_1^2(3C_1 + 2C_2)^2}. \tag{6.6}$$

Again, when the magnitude of the negative term in the numerator is greater than the sum of all the positive terms, G_{12} is negative.

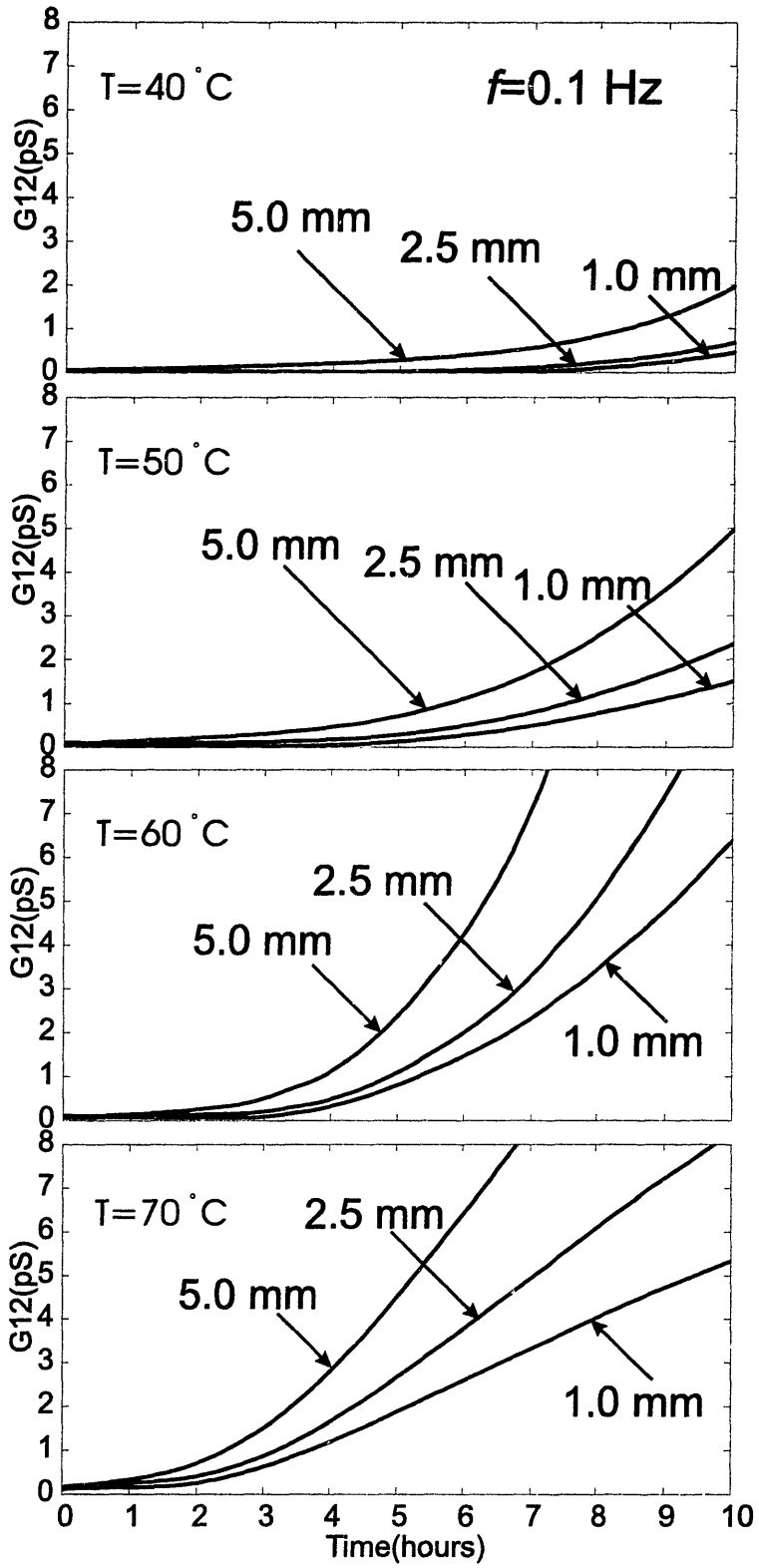

Figure 6.8: The measured transconductance of the three-wavelength sensor measurements for 1.5 mm oil-free pressboard under wetting process at $f = 10Hz$ for various temperatures.

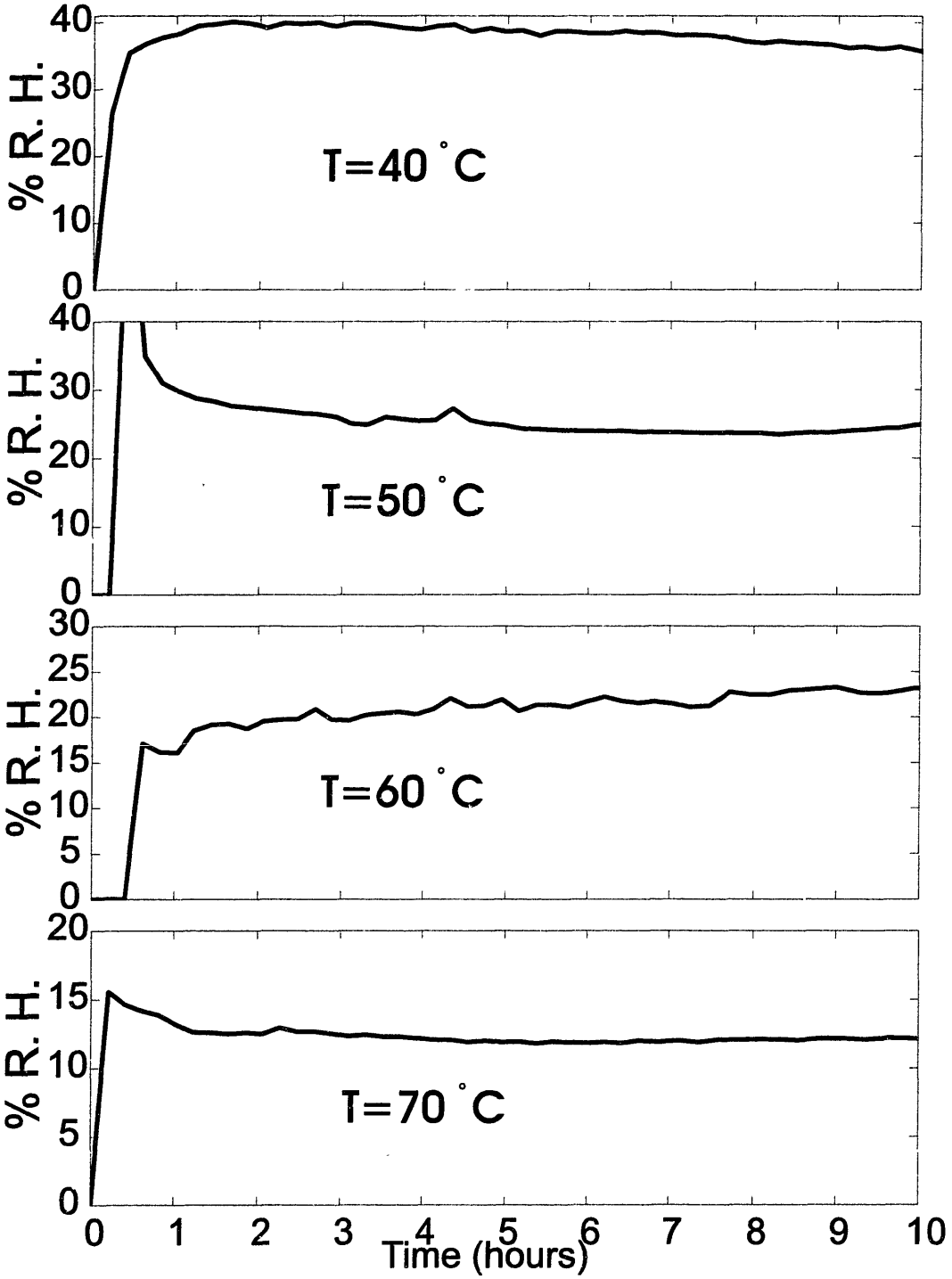

Figure 6.9: The air relative humidity of the test chamber at various temperatures.

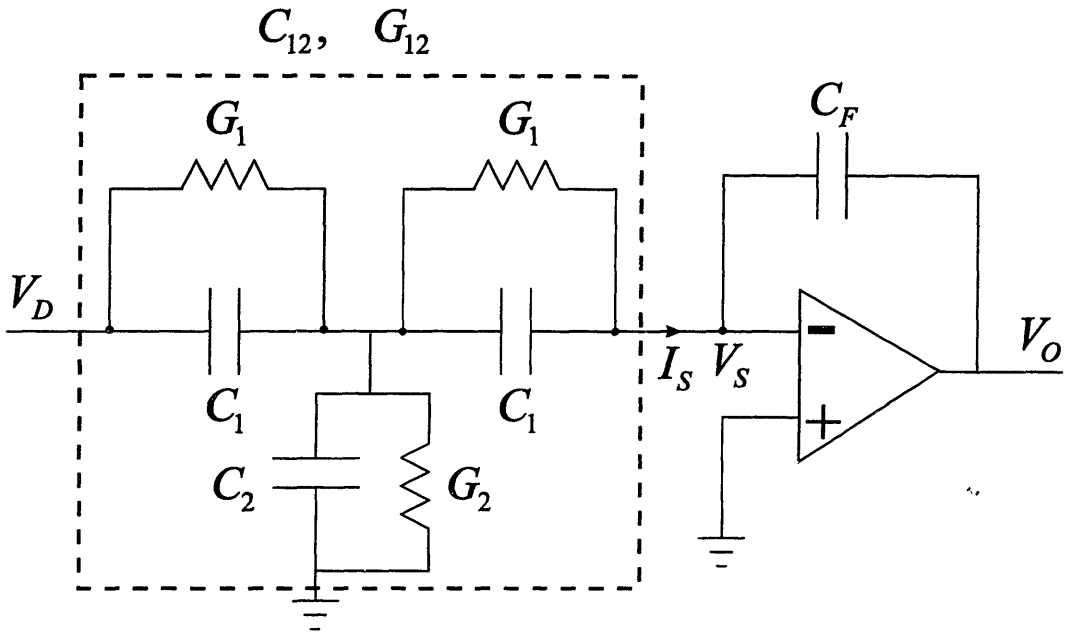

Figure 6.10: The distributed element circuit model for possible negative transconductance.

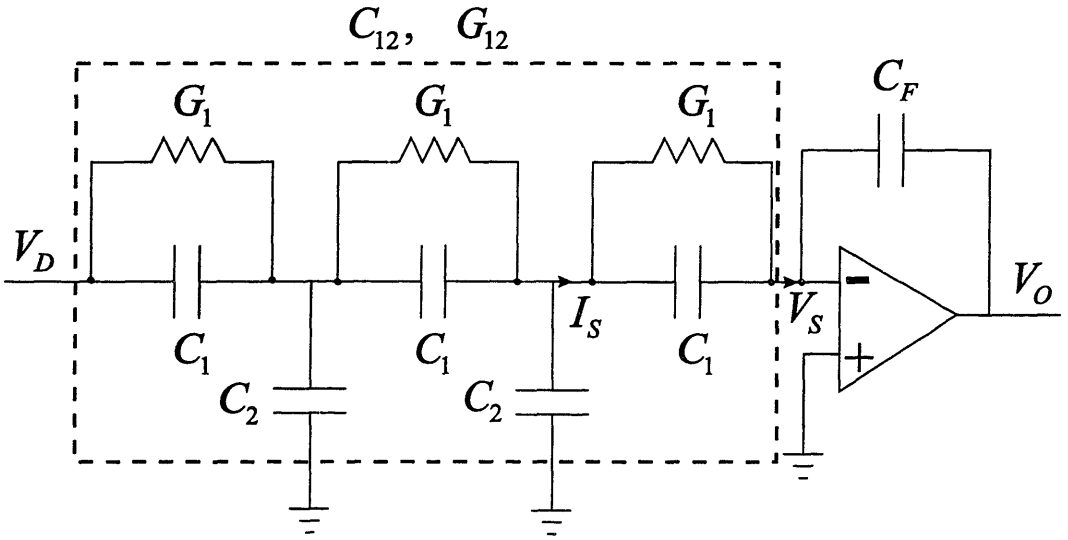

Figure 6.11: Another distributed element circuit model for possible negative transconductance.

Chapter 7

Diffusion Analysis

7.1 Introduction

As illustrated in Chapter 6,the interdigital sensor can be used to measure the diffusion process of moisture in pressboard. Similar tests using interdigital sensors have been done by other investigators to measure moisture diffusion into thin epoxy films [54].

Tests performed for oil-free Hi-Val pressboard at five temperatures: 30, 40, 50, 60, and 70°C are used to analyze the moisture profile and the diffusion coefficient.

7.2 Boundary Conditions

The measurement schematic is shown in Figure 7.1. The moist air flow keeps the relative humidity of the testing chamber at a nearly constant level, which gives a constant moisture boundary condition at the pressboard-air interface at $x = l$. The other side of the pressboard is against the sensor at $x = 0$, which imposes a zero flux boundary condition.

The air relative humidity is monitored by a commercial relative humidity sensor and the value is converted to the moisture in pressboard at the $x = l$ boundary using air-pressboard equilibrium curves drawn by Oommen [16] from Jeffries' data [22]. At each temperature each curve is fitted with a 6th-order polynomial to be conveniently

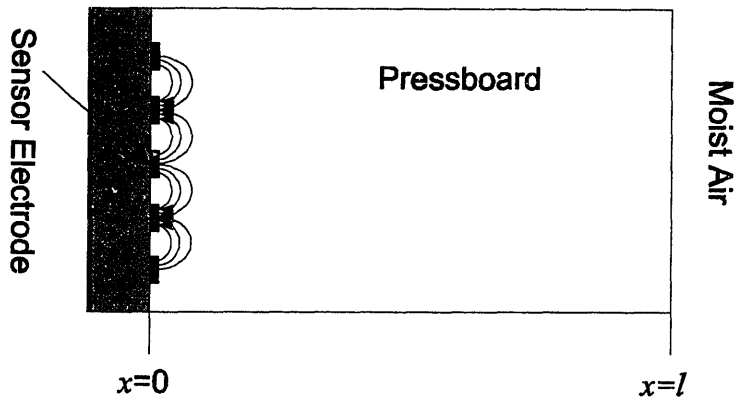

Figure 7.1: 1 mm wavelength sensor detects changes near the pressboard-sensor surface at $x = 0$ while the moisture diffuses from the ambient at $x = l$.

used in the algorithm:

$$y = a_6x^6 + a_5x^5 + a_4x^4 + a_3x^3 + a_2x^2 + a_1x + a_0, \tag{7.1}$$

where x is the air relative humidity in percent and y is the moisture in paper in percent by weight. The coefficients in Equation 7.1 are listed in Appendix C.

7.3 Moisture Spatial Profile

In this section, the output of the three wavelengths at 70°C is used to find the moisture spatial profiles and then the diffusion process is simulated using a constant moisture diffusion coefficient model until the numerical model reasonably matches the experimental profile.

7.3.1 Distribution of Dielectric Properties

Even though the change of the pressboard properties through its thickness is gradual in the discussed experiment, the pressboard in the model is represented as a three-layer medium with each layer thickness corresponding to the effective penetration depth of 0.3λ for each wavelength λ of the sensor. This is illustrated in Figure 7.2. In other words, the number of wavelengths limits the spatial resolution of the sensor, and only

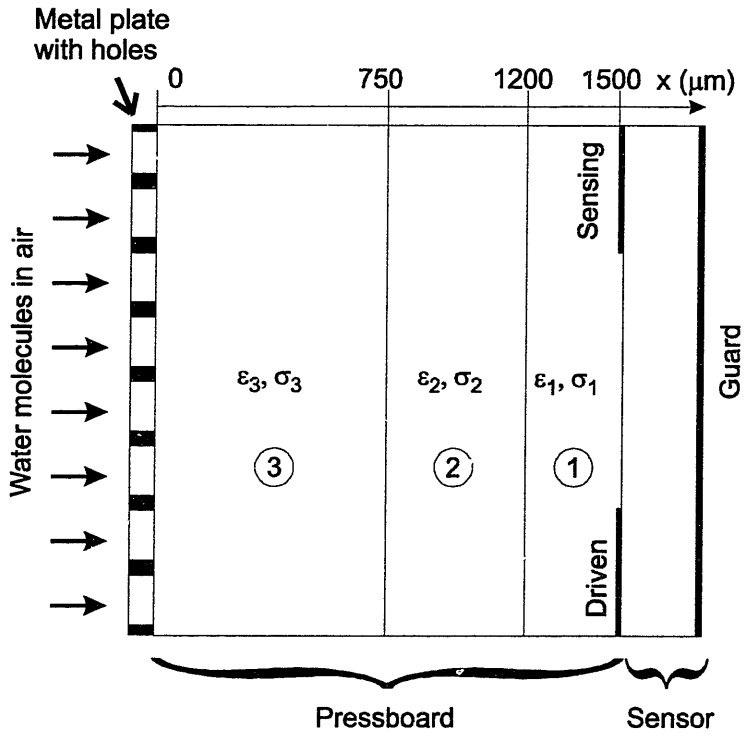

Figure 7.2: A schematic representation of the experimental arrangement. The 1.5 mm thick oil-free pressboard is modeled as a three-layer medium with distinct properties for each layer related to the quantity of moisture in each layer.

three regions can be distinctively identified with the three-wavelength sensor of Figure 6.1. Described later in this section, the knowledge of the temporal dynamics of the process helps to improve this representation when plotting moisture profiles.

Figure 7.3 shows the values of measured transcapacitance for each of the three electrode pairs. Each signal follows approximately the same pattern dictated by the diffusion dynamics. After a small initial delay, the signal grows at a high rate, after which it flattens off, indicating the end of the diffusion process experiment. The initial delay time is the smallest for the largest wavelength because it can "see" deepest into the pressboard.

The relative amplitude of change of transconductance is normally larger than that of the transcapacitance due to the high electric conductivity growth with the increase of

the moisture concentration. Nevertheless, as demonstrated below, the transcapacitance provides sufficient sensitivity for the moisture profile measurements.

7.3.2 Moisture Profiles

The transcapacitance signals in Figure 7.3 were used to generate the curves of moisture concentration in the pressboard layers, assuming a linear relationship between the capacitance values and the moisture levels at each moment of time. That is, the zero level of moisture concentration corresponds to the lowest capacitance value in Figure 7.3 for each wavelength. The highest capacitance value for each wavelength corresponds to the moisture level of 1.8%. In both cases, at the initial time point and the final time point, the moisture profile is believed to be flat and in equilibrium at 0% and 1.8%, respectively. Consequently, the intermediate values of the moisture concentration would correspond to flat moisture profiles that extend from the left side boundary into the pressboard until the penetration depth interface that is reached.

Figure 7.4 shows the change in the average values of moisture concentration in the three regions that correspond to the penetration depths of the three wavelengths of the sensor. The average value corresponds to the cumulative amount of moisture in all regions within reach of a given penetration depth. The small difference between the moisture concentration measured by the 2.5 mm and the 1.0 mm wavelengths is related to a relatively small signal delay difference in the detection time analysis. Since the right side blocked boundary condition eliminates the moisture escape, the gradient-driven diffusion process results in a nearly flat moisture concentration profile across regions 1 and 2 of the pressboard indicated in Figure 7.2.

Figure 7.5 shows calculated moisture profiles from dielectrometry measurements for 14 distinct moments of time in 2 hour intervals. The moisture spatial profiles were calculated from the measurement data using multi-variable parameter estimation algorithms for the three-wavelength sensor combined with the moisture measurement data of the ambient environment together with moisture equilibrium curves.

The process starts with a step change in moisture concentration to 1.8% at the

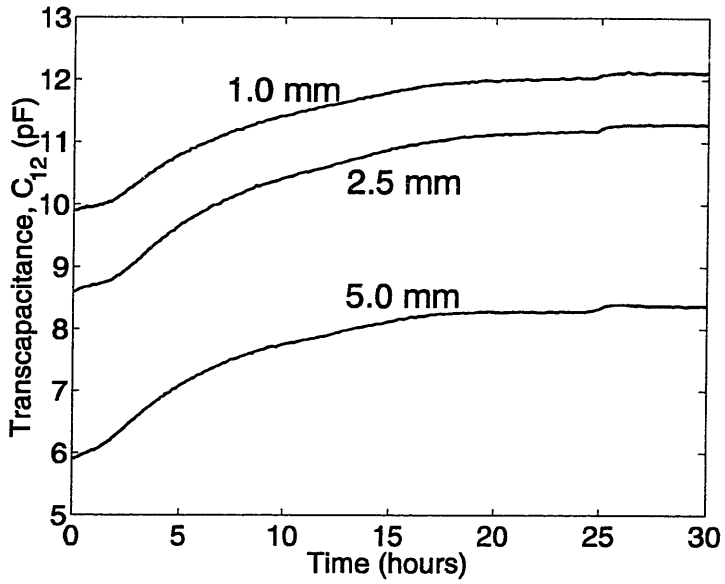

Figure 7.3: Measured capacitance between each electrode pair throughout the moisture diffusion experiment in 1.5 mm thick oil-free pressboard for each sensor wavelength.

left boundary at time zero. The first two profiles (at the time moments of two hours and four hours) show a slightly overestimated amount of moisture in the middle region of the pressboard. Future work will include the mass conservation requirements in order to improve the spatial resolution without adding more electrode pairs of different spatial periodicity.

The experiment is terminated after about 30 hours, when the signals essentially stop changing. At this point, the moisture profile is expected to be almost uniform and at the maximum value of 1.8%. The profile at 28 hours has these characteristics.

Now, it is possible to evaluate the moisture diffusion coefficient from the moisture dynamics presented in Figure 7.5. By simulating the diffusion process using a standard finite difference technique, one can match the measured profiles. The estimated value of the diffusion coefficient is $D = 2.3 \times 10^{-11}$ m^2/s. Figure 7.6 shows theoretical moisture profiles generated using the estimated value of diffusion coefficient that are in reasonable agreement with the measured profiles in Figure 7.5.

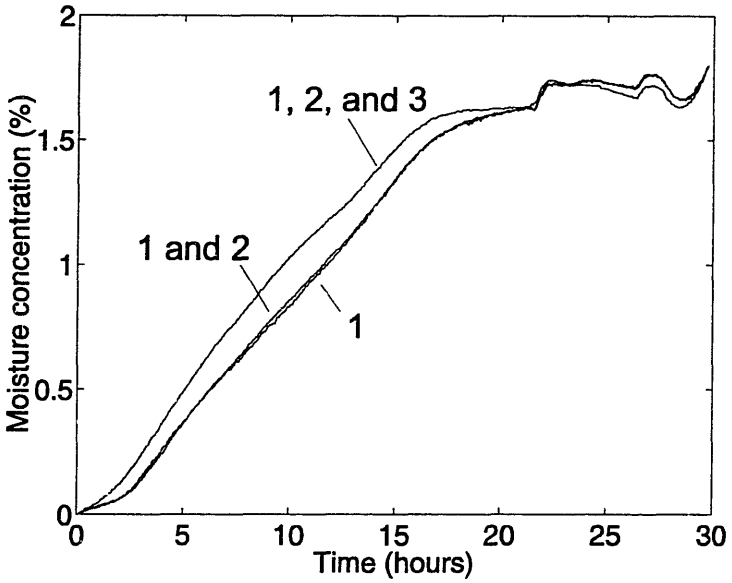

Figure 7.4: Average moisture level measured by each wavelength: region 1 (1 mm), regions 1 and 2 (2.5 mm), and regions 1, 2, and 3 (5 mm).

7.4 Calculation of Diffusion Coefficient as a Function of Temperature and Moisture Concentration

In this section, a linear relation between the transcapacitance and the moisture concentration is also assumed, and the output of the shortest wavelength of 1 mm at different temperatures is used to find the diffusion coefficient as a function of concentration and temperature. The shortest wavelength provides the most accurate values of moisture concentration because the moisture distribution near the zero flux boundary is essentially constant within its relatively small penetration depth.

This section analyzes the signals from the sensing electrodes taken at 1 Hz sinusoidal frequency. The 1.0 mm wavelength sensor measures the transadmittance of the region close to the sensor-pressboard interface. The moisture concentration at the sensor-pressboard interface at any time during the diffusion process is measured using a linear relationship between the transcapacitance and the moisture concentration.

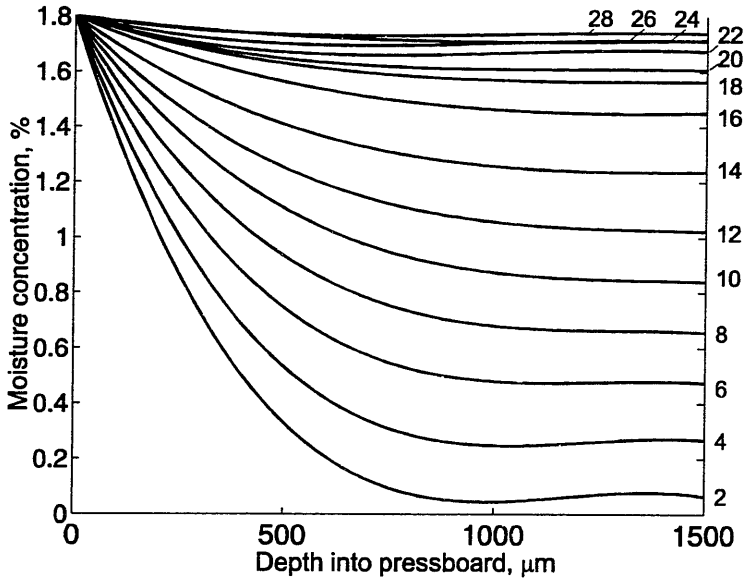

Figure 7.5: Calculated spatial profiles of moisture concentration across the thickness of the oil-free pressboard from dielectrometry measurements. Numbers next to the curves correspond to the time in hours at which the profile was measured.

7.4.1 Diffusion Analysis

Our goal is to find the diffusion coefficient D and the moisture spatial profiles during the entire diffusion process. The diffusion of moisture is defined mathematically in one dimension by Fick's second law of diffusion:

$$\frac{\partial C}{\partial t} = \frac{\partial}{\partial x}(D\frac{\partial C}{\partial x}). \tag{7.2}$$

When D is a constant, the closed form solution for zero initial distribution and constant boundary condition C_1 at $x = l$ and zero flux at $x = 0$ is

$$C = C_1 \left\{ 1 - \frac{4}{\pi} \sum_{n=0}^{\infty} \frac{(-1)^n}{2n+1} \, e^{-t/\tau_n} \cos \frac{(2n+1)\pi x}{2l} \right\}, \tag{7.3}$$

where

$$\tau_n = \frac{4l^2}{D(2n+1)^2\pi^2}. \tag{7.4}$$

When the diffusion coefficient is concentration-dependent, Equation (7.2) becomes non-linear and no general analytical solution is available. Numerical methods are then employed to solve the diffusion equation.

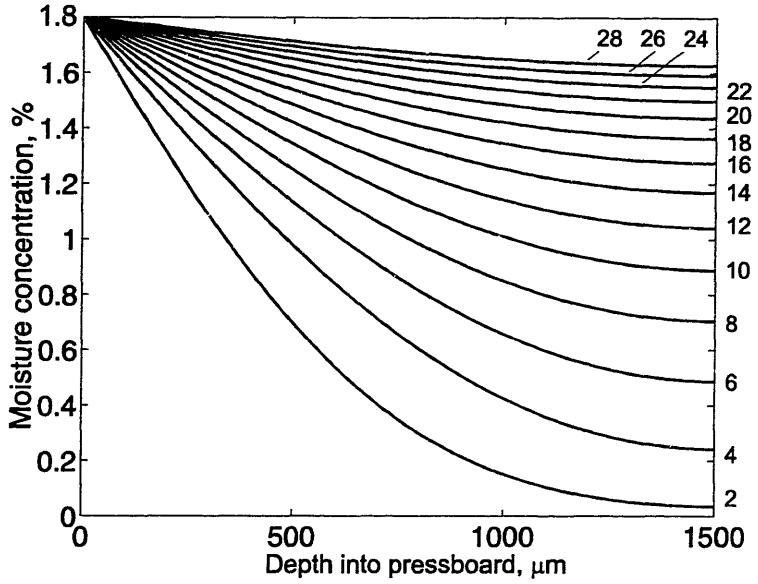

Figure 7.6: Theoretical spatial profiles of moisture concentration across the thickness of oil-free pressboard. Numbers next to the curves correspond to the time in hours after the moisture was stepped on to 1.8% at $x = 0$.

The empirical temperature and moisture concentration dependence model of Equation (7.5) is used here to find the corresponding parameters, D_0, k, and E_a, for Hi-Val pressboard from our experiments:

$$D(C,T) = D_0 e^{kC+E_a(1/T_0-1/T)}, \tag{7.5}$$

Let

$$dz = D(C)dC, \tag{7.6}$$

So that Equation (7.2) becomes

$$\frac{\partial C}{\partial t} = \frac{\partial^2 z}{\partial x^2}. \tag{7.7}$$

Equation (7.7) is discretized for numerical calculation

$$\frac{C_j^{n+1} - C_j^n}{\Delta t} = \frac{z_{j+1}^{n+1} - 2z_j^{n+1} + z_{j-1}^{n+1}}{(\Delta x)^2}, \tag{7.8}$$

D_0	k	E_a
0.67×10^{-12} m^2/s	0.45	7646 °K

Table 7.1: Diffusion coefficient parameters obtained from measurements using a least squares fit.

where superscript n corresponds to time steps and subscript j corresponds to space steps. This backward time scheme is chosen for stability of the algorithm [55].

Then, z can be derived in terms of C from

$$dz = D(C)dC = D_0 e^{kC+E_a(1/T_0-1/T)}dC, \tag{7.9}$$

as

$$z = \frac{D_0}{k} e^{kC+E_a(1/T_0-1/T)}. \tag{7.10}$$

Standard numerical procedures are then carried out to solve Equation (7.8).

To find the parameters for the diffusion coefficient, the measured moisture concentration of the 1 mm wavelength sensor is taken at five different temperatures and the Matlab built-in function for least squares fit, *leastsq*, in the optimization toolbox is used to find the parameters that minimize the sum of the error squares of the moisture concentration. The results are shown in Table 7.1.

7.4.2 Discussion

For $T = 70$°C, the diffusion coefficient at the start when $C = 0\%$ is $D = 1.9 \times 10^{-11}$ m^2/s, and at the end when $C = 1.8\%$ is $D = 4.3 \times 10^{-11}$ m^2/s. The average is about 3.1×10^{-11} m^2/s. This is close to the value that is estimated in Section 5.3 for a constant diffusion coefficient model, 2.3×10^{-11} m^2/s . In this section, the diffusion coefficient is found by minimizing the sum of the error squares between the measured moisture concentration and the theoretical values for various temperatures, whereas the approach in Section 5.3 uses a constant diffusion coefficient to do a forward simulation until the calculated profile closely matches most of the measured profile.

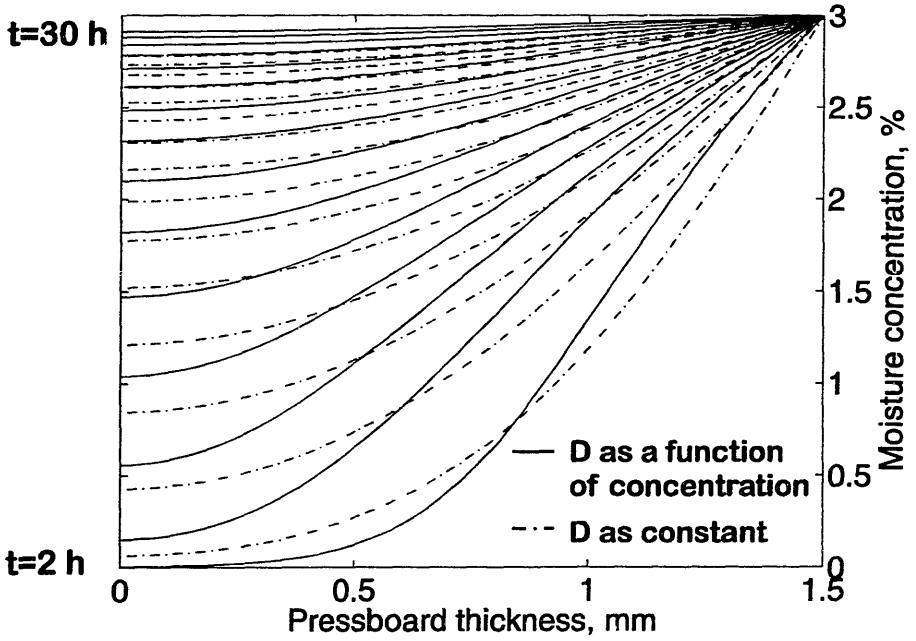

Figure 7.7: Calculated moisture profile in the pressboard at 60°C for diffusion coefficient as a function of concentration using estimated parameters and as a constant $D = 2.4 \times 10^{-11}$ m^2/s, an average of D at $C = 0\%$ and $C = 3.0\%$.

The spatial profiles of the diffusion process at 60°C with the diffusion coefficient as a function of concentration, and as a constant $D = 2.4 \times 10^{-11}$ m^2/s (an average of D at $C = 0\%$ and $C = 3.0\%$) are shown in Figure 7.7. The curves are plotted from 2 hours to 30 hours at 2-hour intervals. At first, since the moisture concentration is low, the diffusion coefficient in most regions is smaller than the average value, the curves for constant diffusion coefficient increase faster than the concentration dependent model. When the moisture in the pressboard increases, the diffusion speed also increases, thus the concentration dependent curves exceed the constant diffusion curves. This also explains why the experimental data in Figure 7.5 of Section 7.3 show that the moisture reaches equilibrium in a time of 28 hours, whereas the constant diffusion coefficient simulation in Figure 7.6 of Section 7.3 has not yet reached equilibrium after 28 hours.

The diffusion coefficient for oil-free pressboard calculated here is much smaller than that reported in [35]. This could be possibly due to three reasons. First, the materials

Source	MIT	Foss [35]	Quarshie [56]
Material	Pressboard	Kraft paper	Manilla paper
$C = 2.1\%$	2.5×10^{-11}	1.3×10^{-9}	1.3×10^{-11}
$C = 3.0\%$	3.8×10^{-11}	2.1×10^{-9}	4.8×10^{-11}

Table 7.2: A comparison of our measured diffusion coefficient (m^2/s) and literature reported values at 60°C.

are different. Foss' data are for A50P281A Kraft paper made from 100% sulphate fiber with thickness of 0.01 inch. The reported value in [56] by Quarshie is close to our results given in Table 7.2. Quarshie used 50 layers of Manilla paper, each 0.045 mm thick.

Second, our sample is tightly compressed. Pressure has been shown to slow down the diffusion process [56]. For the EHV-Weidmann T-IV pressboard that Quarshie tested, the diffusion coefficient of unclamped pressboard is about 1.3 times that of clamped pressboard.

Third, due to the porous squeezing structure at the pressboard-air interface, the pressboard is not completely exposed to the ambient at that interface. This might slow down the diffusion, but the effect should be small because according to the manufacturer, the diffusion in the direction parallel to the interface is much faster than that to the direction perpendicular to the interface which we are studying.

Chapter 8

Conclusions

A comprehensive survey is performed for existing methodologies to measure moisture in transformer insulation. Several sets of classic moisture equilibrium curves are studied and a comparison is given for each method. A new set of curves is constructed based on the best method. This is a useful tool for utilities and power system monitoring manufacturers. Moisture measurement for oil shows the solubility of moisture in oil increases significantly only in severely aged transformer oil.

When the system is not in equilibrium, the moisture curves are not applicable and the three-wavelength interdigital dielectrometry sensor developed at the MIT Laboratory for Electromagnetic and Electronic Systems is a unique way to measure the spatial profile of the moisture distribution in transformer pressboard. Preliminary measurements of oil and oil-impregnated pressboard are given in this thesis. A joint research group effort led to development of an improved design of the three-wavelength sensor which reduces the problems associated with the previous design and simplifies the inversion algorithm to convert the electrical signals to dielectric properties. The thesis focuses on the design and implementation of experimental studies based on interdigital dielectrometry using the new three-wavelength sensor.

As a first step to relate measurable dielectric properties to absorbed moisture, the moisture and temperature effects on the dielectric spectrum of oil-free pressboard are measured using a parallel-plate geometry sensor for nine moisture levels and five

temperature levels. A dielectric model for biological tissue is adopted here for cellulose structured pressboard. A universal curve is found relating dielectric properties to moisture concentration and temperature by fitting the data to the model. Preliminary measurements of the oil-impregnated pressboard show similar characteristics.

An improved bench-top apparatus is designed to implement various moisture measurements using an interdigital dielectrometry sensor. Diffusion processes in oil-free pressboard are monitored at five different temperatures using the interdigital dielectrometry sensor technology. Improved sensing techniques provide better quality signals and results. Sensor measurements agree well with theoretical analysis for effects of pressboard thickness and temperature. The ability of the interdigital sensor to be able to measure the moisture distribution is demonstrated through the bench-top experimental results.

Real-time on-line measurement of the moisture diffusion process is achieved in this research project. For the first time, the time evolution of the moisture spatial profile in oil-free transformer pressboard has been estimated non-destructively. The moisture diffusion profiles have been obtained using the three-wavelength interdigital sensor with a fast algorithm suitable for on-line monitoring with real time display of results. An algorithm is developed for finding the diffusion coefficient as a function of moisture concentration and temperature. The understanding of moisture-related processes in power transformers can be enhanced with this methodology.

There is no analytical solution of the time dependent moisture profiles for a diffusion coefficient as a function of temperature and moisture concentration. A numerical algorithm is developed for finding the diffusion coefficient as a function of moisture concentration and temperature from experiments. The calculated results extend the existing small data base of diffusion studies.

Appendix A

Instructions for Using the Bench-top Apparatus

For the bench-top apparatus shown in Figure 6.3; some of the operations are under pressure and high temperature; so safe operation of the system is very important. Because the top of the reservoir is not bolted down to the body and it has large surface area, a small pressure will create a large force that could lift the top. Therefore, it is important always remember the following: no pressure for the reservoir. For individual operation, the procedures as well as the order of operations are as follows and must be followed exactly. Visualize the flow direction helps to operate the system. All the valves of the system are labeled.

1. Vacuum test chamber free of oil

V3 off; V4 off; V5 off; V7 off; V1 to vacuum; V10 off; V12 on; vacuum pump on. Other valves are not directly associated with this operation and should be positioned in accordance with the function of the rest of the system. This applies to the following operations as well.

2. Vacuum test chamber with oil without circulation

V3 off; V4 off; V5 off; V7 off; V1 to vacuum; V10 off; V12 off; vacuum pump on; V12 on gradually according to the degassing condition to avoid oil being sucked into the moisture trap.

3. Vacuum test chamber with oil circulation within test chamber only

V1 to vacuum; V3 to a; V4 off; V5 to a; V7 off; V12 off; V10 off; vacuum pump on; V12 on gradually according to the degassing condition to avoid oil being sucked into the moisture trap; circulation pump on after system stabilizes under vacuum.

4. Vacuum reservoir with oil

V6 off; V5 off or to a; V4 off; V3 off or a; V11 off; V8 off; vacuum pump on; V2 to vacuum gradually according to the degassing condition. Magnetic stirrer on to allow thorough diffusion after oil stabilizes under vacuum.

5. Get oil from outside into vacuumed test chamber

After vacuum, oil in/outlet port to oil source by plastic tube, V3 off, V4 off, V5 off, V12 off, V1 off, vacuum pump off, V7 on.

6. Transport oil from reservoir into vacuumed test chamber

After vacuum, turn off magnetic stirrer, V4 off, V7 off, V2 to air/nitrogen, V8 off, V11 to vent, V1 off, vacuum pump off, V12 off, V3 to a, V5 to b. Turn light on for observation.

7. Transport oil from reservoir to test chamber by circulation pump

V1 to air, V2 to air, V3 to a, V4 off, V5 to b, V6 off, V7 off, V8 off, V10 to vent, V11 to vent, V12 on, circulation pump on.

8. Get oil from outside into reservoir after vacuum

After vacuum, V3 off or a, V4 off, V5 off or to a, V8 off, V11 off, the oil in/outlet near V6 connected to oil source by plastic tube, V2 off, vacuum pump off, V6 on.

9. Transport oil from test chamber to reservoir by circulation pump

V1 to air, V2 to air, V3 to b, V4 off, V5 to a, V6 off, V7 off, V8 off, V10 to vent, V11 to vent, V12 on, circulation pump on.

10. Get oil out of test chamber by gravitation

V1 to air, V3 off, V4 off, V5 off, V10 to vent, V12 on.

11. Get oil out of test chamber with nitrogen pressure

Bolt down the feed-through with SMA adapters, V1 to air/nitrogen, V12 on, V10 to nitrogen, V3 off, V4 off, V5 off, V7 on, pressure on.

12. Get oil out of reservoir by circulation pump

Connect the oil in/outlet near V6 to container with plastic tube, V2 to air, V3 to b, V4 off, V5 to b, V8 off, V6 on, circulation pump on.

13. Circulate oil within test chamber with system sealed

V1 off, V3 to a, V4 off, V5 to A, V6 off, V7 off, V10 off, circulation pump on.

14. Circulate oil between reservoir and test chamber with system sealed

Bolt down the feed-through, V1 off, V2 off, V3 to a, V4 on, V5 to b, V6 off, V7 off, V8 off, V9 off, V10 off, V11 off, V12 on, circulation pump on.

15. Bubbling moist air to reservoir

Connect pressure source (either nitrogen cylinder or pressure pump) to the gas source with pressure off, V2 to air, V3 off, V4 off, V5 off, V6 off, V7 off, V8 on, V9 on, V11 to air, turn the pressure on.

16. Bubbling moist air to test chamber

Connect pressure source (either nitrogen cylinder or pressure pump) to the gas source with pressure off, V1 to air, V2 off, V3 off, V4 on, V5 off, V6 off, V7 off, V8 on, V9 on, V10 to vent, V11 off, V12 on, turn the pressure on.

17. Pressurize test chamber

V1 to nitrogen, V2 off, V11 off, V9 off, V5 off, V4 off, V3 off, V12 on, and V10 to nitrogen.

18. Bubbling moist air while circulating oil between reservoir and test chamber Bolt down the feedthrough top. V1 off, V2 to air, V3 to a, V4 on, V5 to b, V6 closed, V7 closed, V8 open, V9 open, V10 to vent, V11 off, V12 off, and turn bubller on.

Appendix B

New Interface Box

B.1 Interface Box Circuitry

The interface box circuitry is composed of three parts: digital expansion board; drive board; and sensing board.

The schematic of the digital expansion part shown in Figure B.1. The major function is to enable the interface box to run three channels individually and can switch the integration capacitors for different test impedances.

The schematic of the drive board is shown in Figure B.2. Its function is to amplify the one volt peak sinusoidal signal from the controller box to 10 volts.

The schematic of the sense board is shown in Figure B.3. Each box has three identical boards for three wavelengths except with different integration capacitor values.

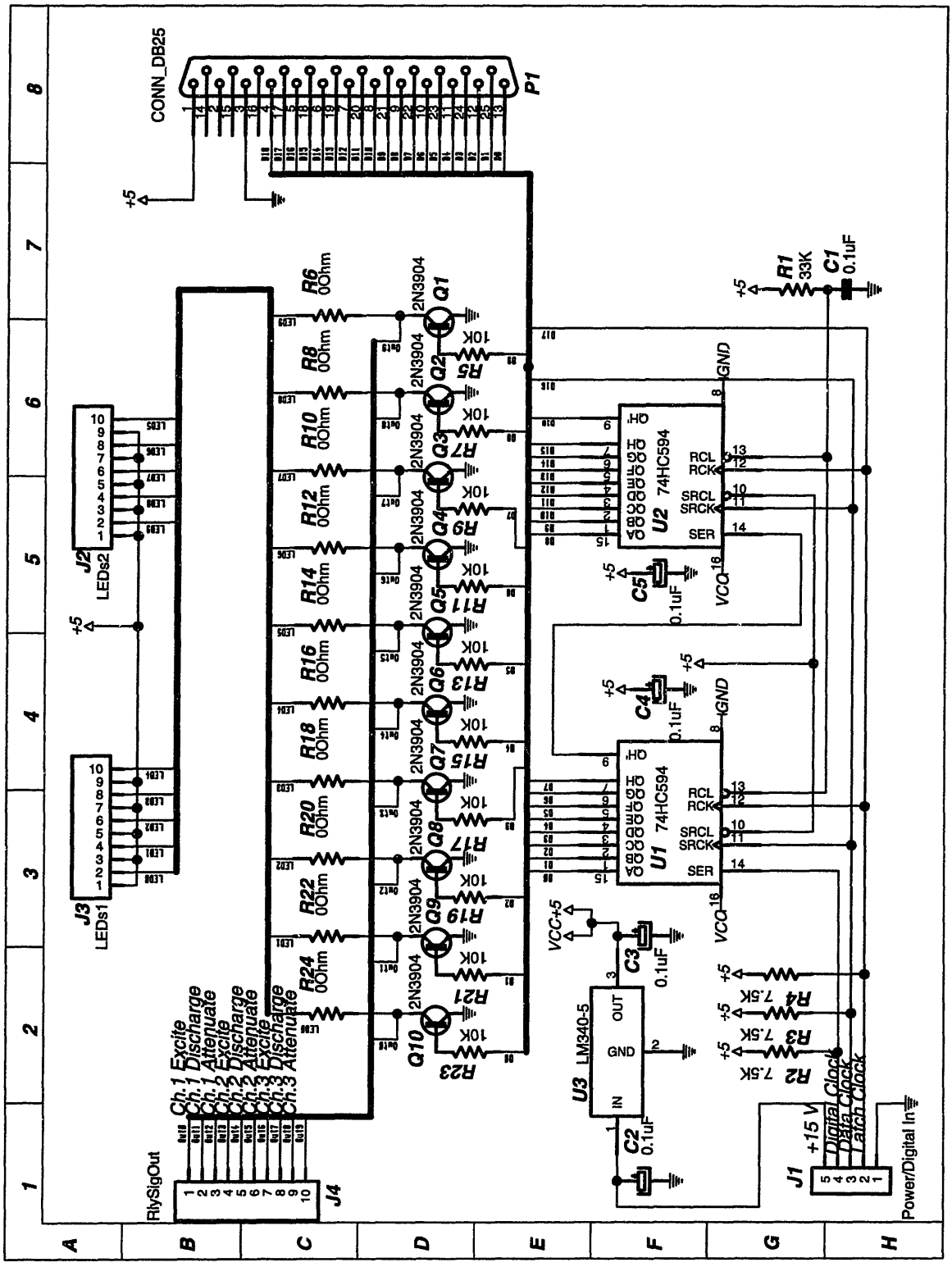

Figure B.1: Schematic of the digital expansion board of the interface box circuitry, mainly laid out by D. E. Schlicker at MIT.

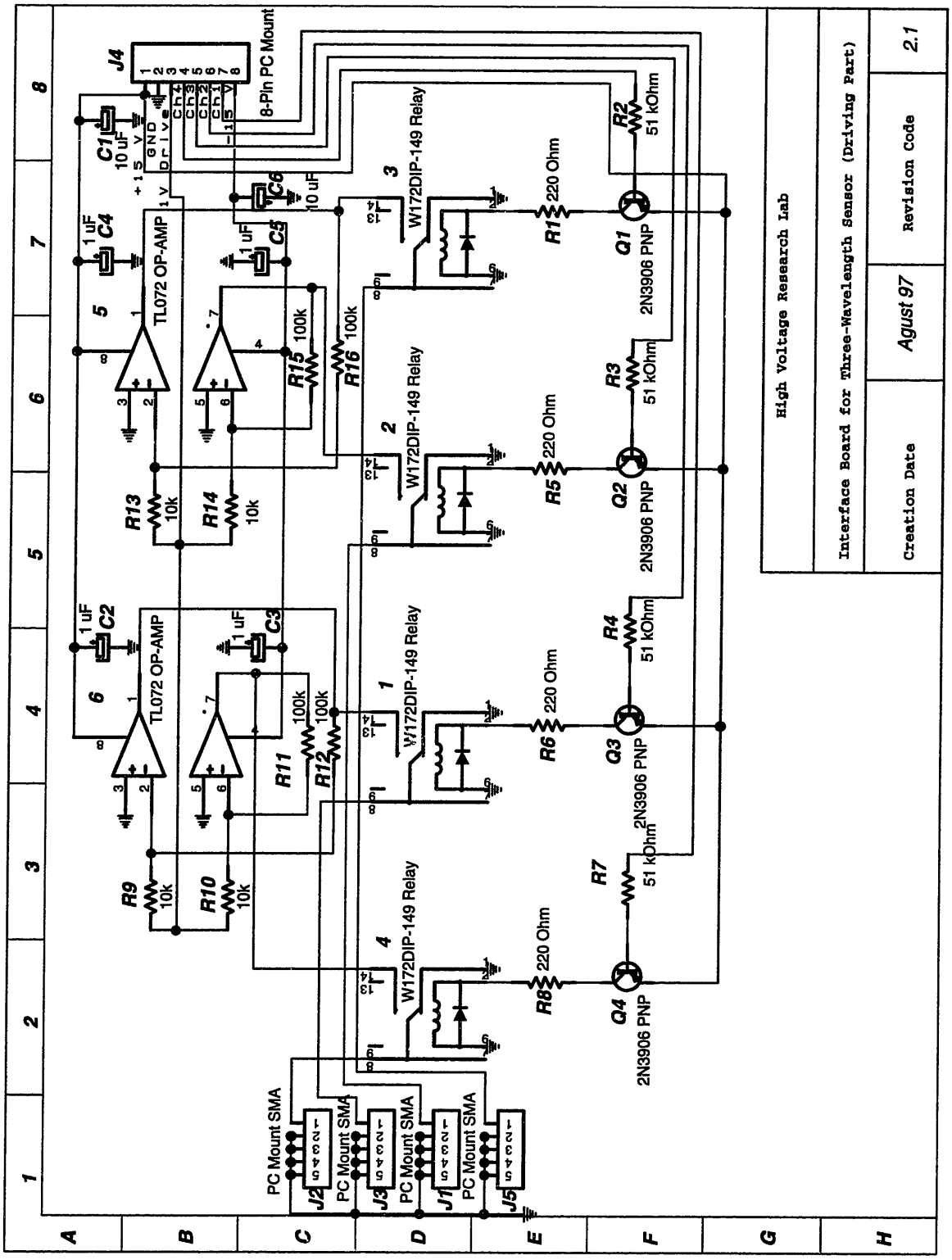

Figure B.2: Schematic of the drive board of the interface box circuitry.

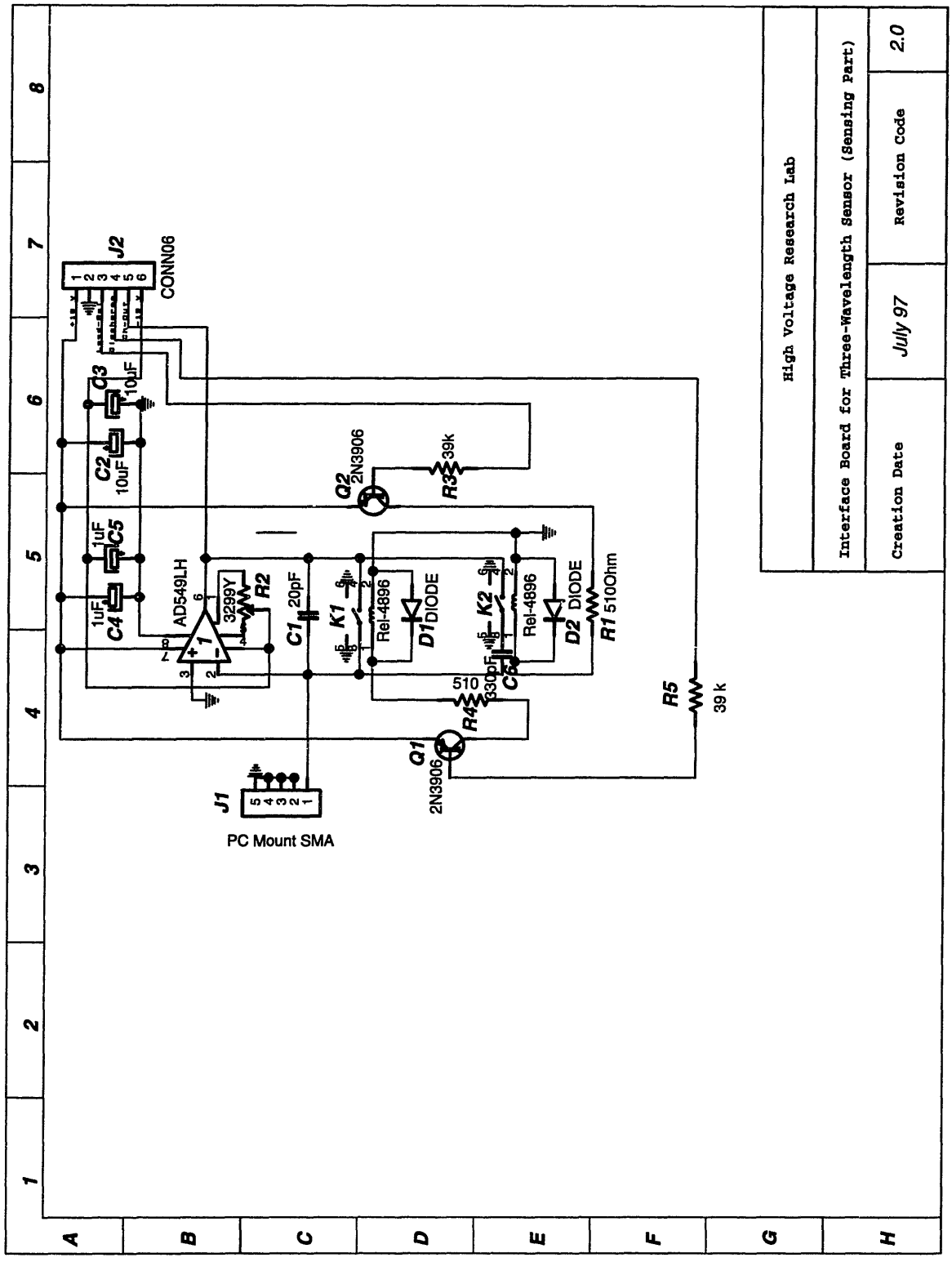

Figure B.3: Schematic of the sense board of the interface box circuitry.

B.2 Box Assembly

B.2.1 Materials to Begin with

Before starting box assembly, make sure the following materials are available:

- Instruction package including these assembly instructions, circuit schematics, PCB layout, bill of materials, pinouts connections, and box machining template.
- All circuit parts assorted in cabinet.
- Circuit boards.

B.2.2 Board Preparation

Cut individual boards from the raw board carefully using the cutter at the LEES machine shop. Need to put paper towel on both sides of the board to protect the surface of the board while cutting.

B.2.3 Board Assembly

Other than the regular board soldering cautions, such as the polarity of the capacitor, diodes, and transistors, there are also special places that need extra attention to:

1. Sense Boards

- The SMA connectors and the OP-AMP are soldered on the solder side.
- The center pin of the SMA connector, pin 2 of OP-AMP, pin 3 of upper relay and two caps' pins are connected in air without touching the board to avoid a leakage path.
- The SMA should be soldered in such a way that the connector is perpendicular to the board edge. Recommended technique is to solder the pins of SMA diagonally.

2. Drive Board

Only three channels are used for now. So only three SMA connectors are connected as shown in Figure B.4.

3. Digital Board

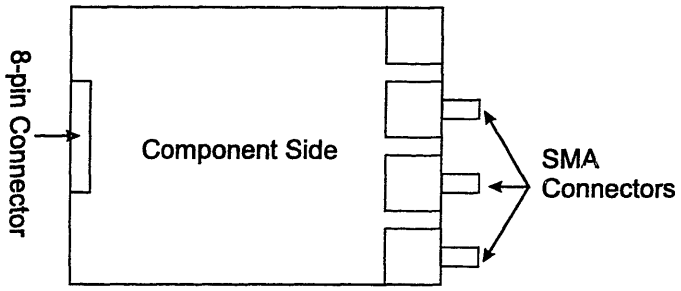

Figure B.4: SMA connections for the drive board.

The 10-pin headers used for LED is IDC (Insulation Displacement Connector), white color, different from that used for the Relay Signal. The pin order we designated is opposite to the header label. The proper pin order is shown in Figure B.5.

B.2.4 Box Assembly

First machine the box following the machine templates shown in Figure B.6, Figure B.7, Figure B.8, Figure B.9, and Figure B.10. The templates are all in real size.

- Sense boards are at the bottom and up-side down.
- The SMAs in the front, from left to right, are Channel 1, 2, and 3, respectively; so the sense boards are also designated this way.
- Sense boards are connected to the bottom side of the Aluminum shielding plate through standoffs. The center board only has three mounting holes on the aluminum plate. Attention must be paid to the orientation of the aluminum plate as indicated in the template.
- Above the aluminum shielding plate is the drive board which has component side up and bolted through stands to the shielding piece.
- The top layer is the digital expansion board and it is component side up. It is mounted to the box through the DB-25 connector. Two porcelain standoffs (about 1 and 3/4" long, such that it touches the aluminum shielding plate; if existing standoff is not long enough, use nylon washers to increase the length) are mounted at the opposite two corners to avoid the digital board touching other places when it is pushed by the LED wires. Without the standoffs, the board could touch the SMA connectors and

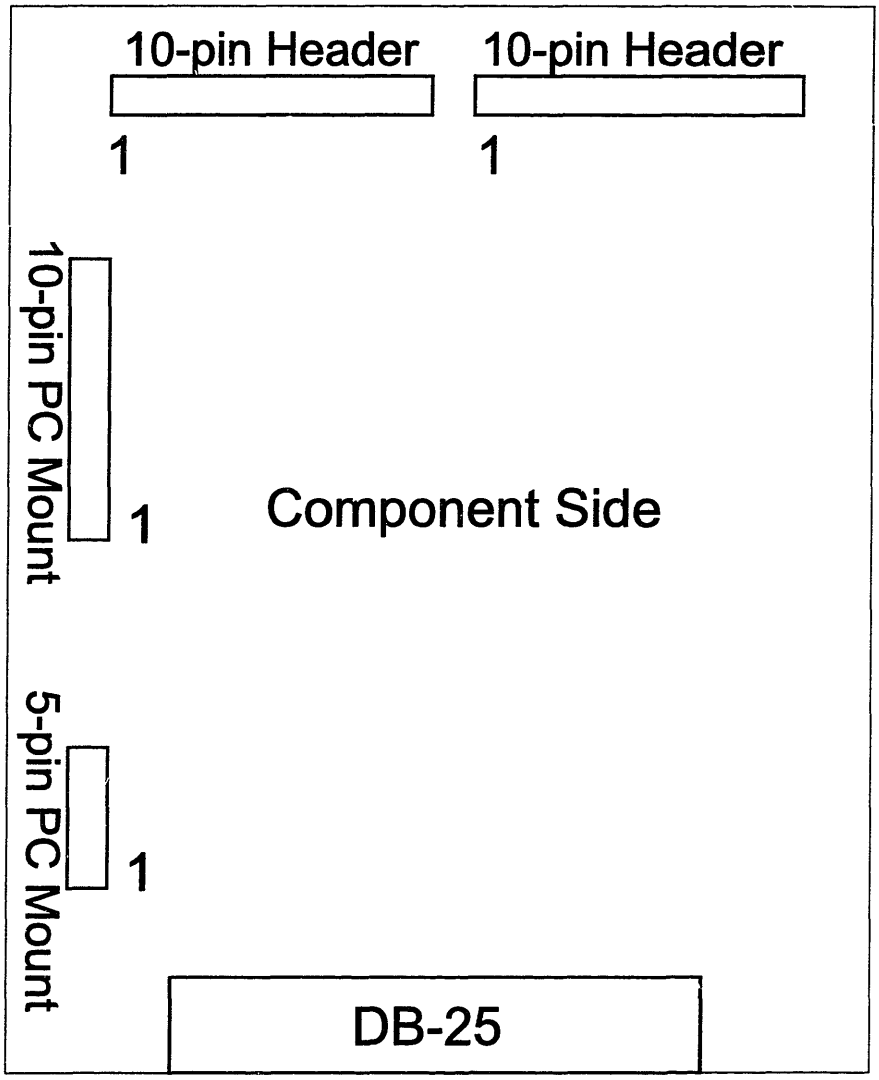

Figure B.5: Connectors for the digital board.

short circuit, and the two shift registers could be easily burnt out.

• The 4-pole double throw switch is mounted in such a way that looking from the back side of the interface box, the C&K label is at left. Each pin is defined as shown in Figure B.11.

B.2.5 Wiring

All wires should be soldered, not just crimped.

• Interface to Controller Connections (Sheet: Interface_Controller)

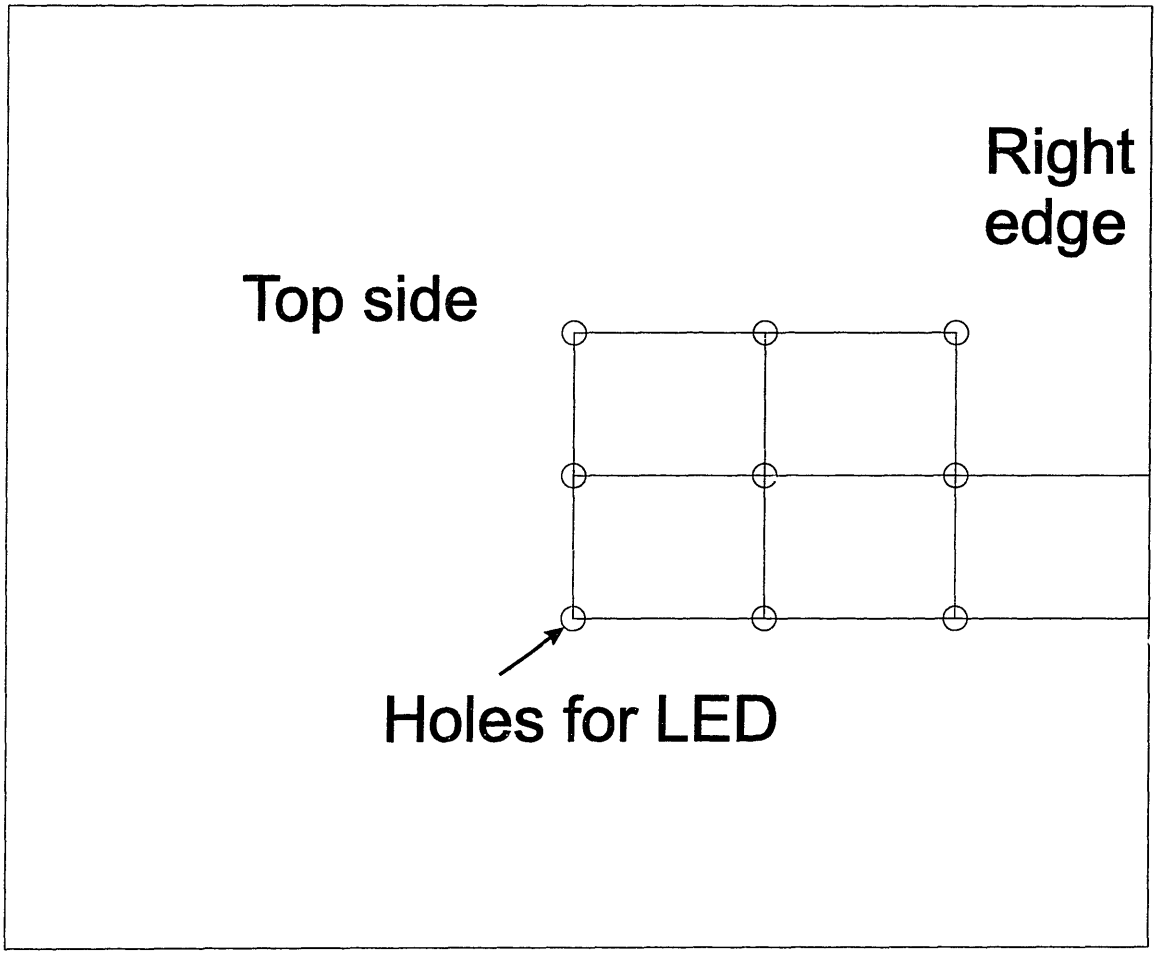

Figure B.6: Machine template for the top of the box for LED connections.

One side of the multi-conductor cable is connected to the DB-15 connector; the majority of wires of the other side of the cable goes to the 9-pin CPC connector while three wires: white, blue, and orange, need to go to the 16-pin CPC connector to the controller box. For this purpose, the multi-conductor cable needs to be peeled back about 10 inches to allow enough wires to go to the 16-pin connector.

Pins 9,10,11,12, and 13 of the DB-15 female part should be connected to GND.

• LED Connections (Sheet: LED (Digital Board))

Looking from the component side, the 10-pin IDC header #2 (LEDs1) is at the left side, and 10-pin header #3 is the one on the right side. Pin order is 1 to 10 from left to right.

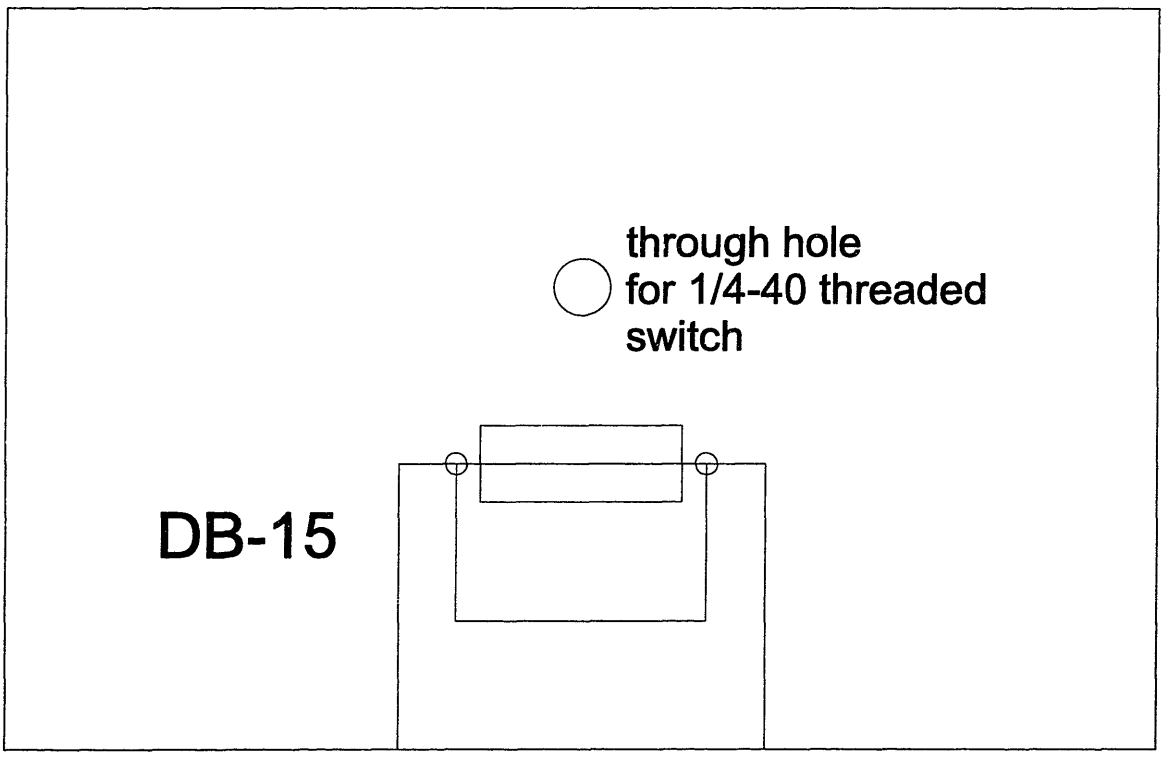

Figure B.7: Machine template for DB 15 connector on the back of the box.

- Board Wiring (Sheet: Wire Chart)

All the PC mount headers on the drive board and sense boards are in reverse pin order, i.e. the arrow in the header indicates the last pin, instead of pin 1. The two PC mount headers in the Digital Board are in the right order, i.e. the arrow indicates Pin 1.

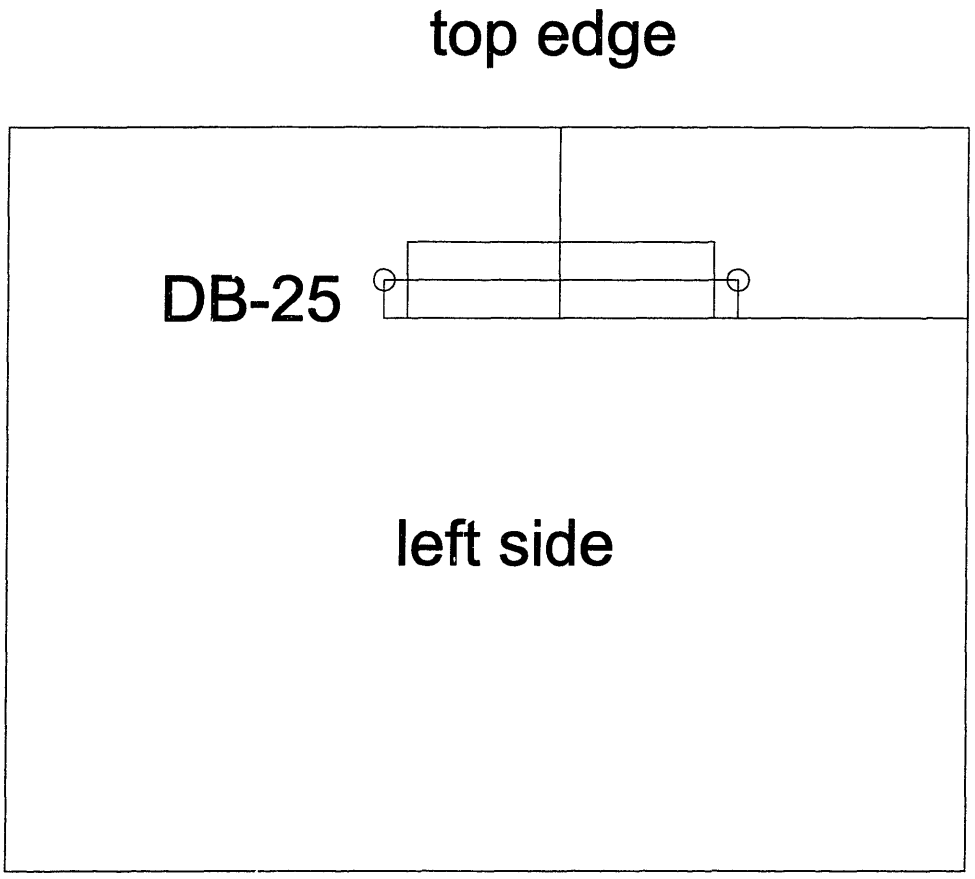

Figure B.8: Machine template for DB 25 connector on the side of the box.

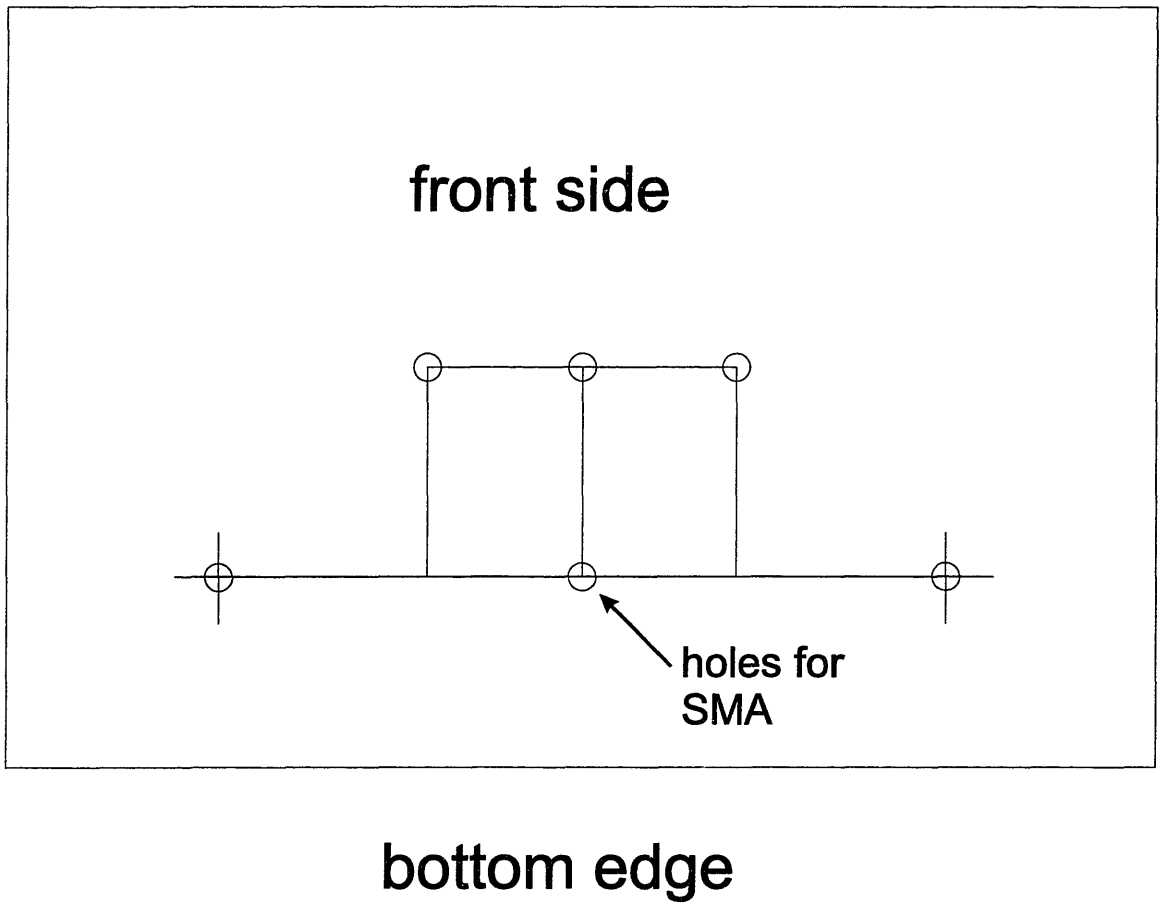

Figure B.9: Machine template for SMA connectors on the front of the box.

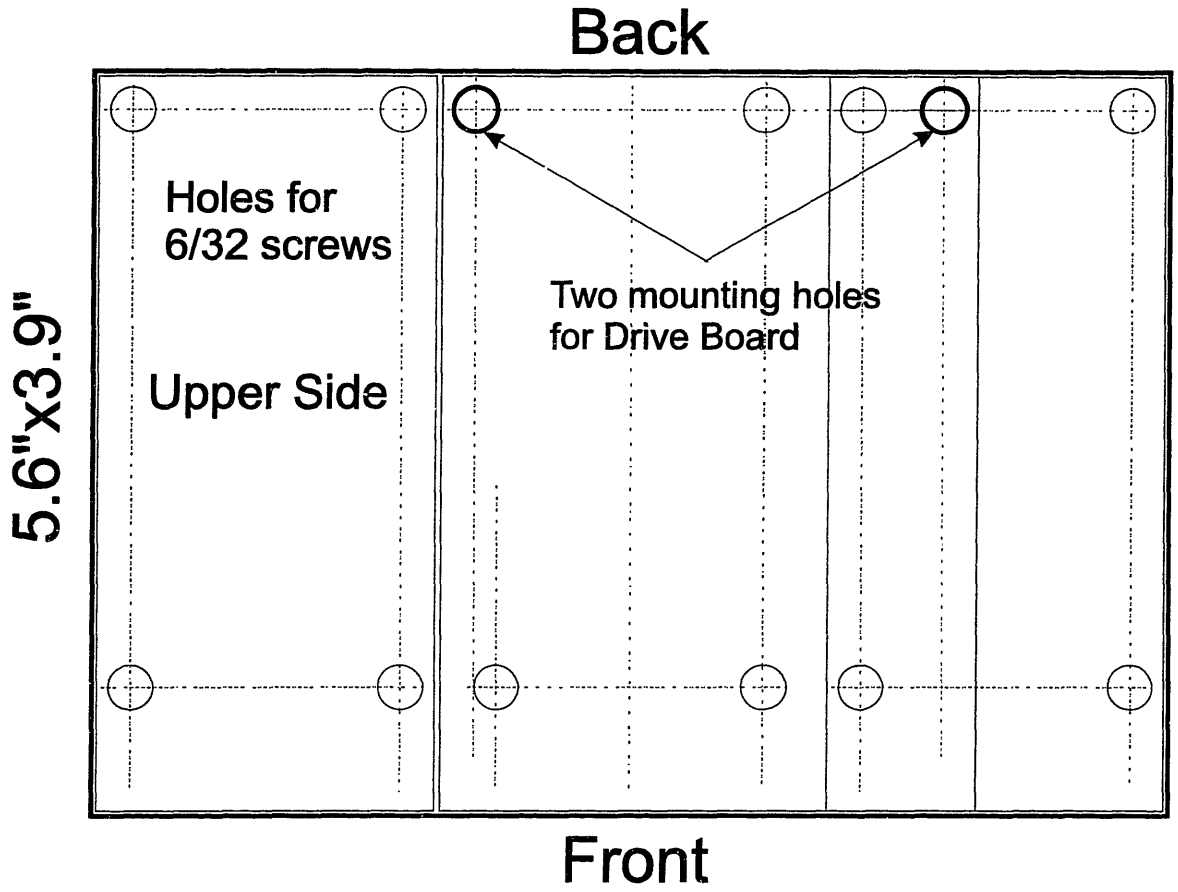

Figure B.10: Machine template for the shielding and separating aluminum plates.

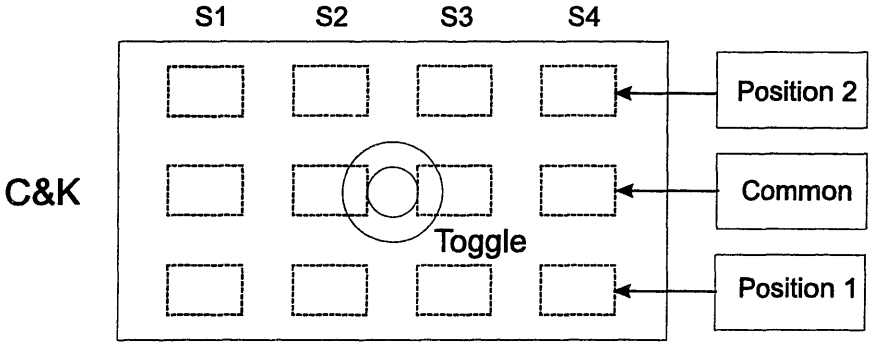

Figure B.11: Numbering and positioning of the four-pole double-throw C&K switch for the relay signal.

Appendix C

Moisture Content in Wood Pulp

Jeffries reported data for the moisture content in wood pulp versus ambient relative humidity as a function of temperature in [22]. Oommen [16] drew a group of equilibrium curves from Jeffries' data which can be used to find the moisture content in the pressboard at the boundary when the air relative humidity is monitored. At each temperature each curve is fitted with a 6th-order polynomial to be conveniently used in the algorithm

$$y = a_6x^6 + a_5x^5 + a_4x^4 + a_3x^3 + a_2x^2 + a_1x + a_0, \tag{C.1}$$

where x is the air relative humidity in percent and y is the moisture in paper in percent by weight. The coefficients in (C.1) are shown in Table C.1. The moisture equilibrium curves reconstructed from the 6-th order polynomial are shown in Figure C.1.

T (°C)	30	40	50	60	70
$a_6(\times 10^{-11})$	-9.3468655	-3.8729882	9.5319144	7.4380470	16.252499
$a_5(\times 10^{-8})$	4.2446633	2.5228351	-1.1755019	- 0.75286519	- 3.3218692
$a_4(\times 10^{-6})$	-6.3395879	-4.2926236	-0.37397578	- 0.57129397	2.2473555
$a_3(\times 10^{-4})$	4.3831525	3.2448905	1.2731316	1.1731076	- 0.27101029
$a_2(\times 10^{-3})$	- 14.929696	-11.950117	-7.2850779	-6.2300223	- 2.7797731
$a_1(\times 10^{-1})$	3.2828657	2.9079147	2.4316118	2.1359436	1.7762623
$a_0(\times 10^{-1})$	2.4131270	1.6954583	1.0483257	1.3978572	0.7441865

Table C.1: Polynomial fitting parameters for partition curves for ambient air relative humidity and moisture in paper for various temperatures.

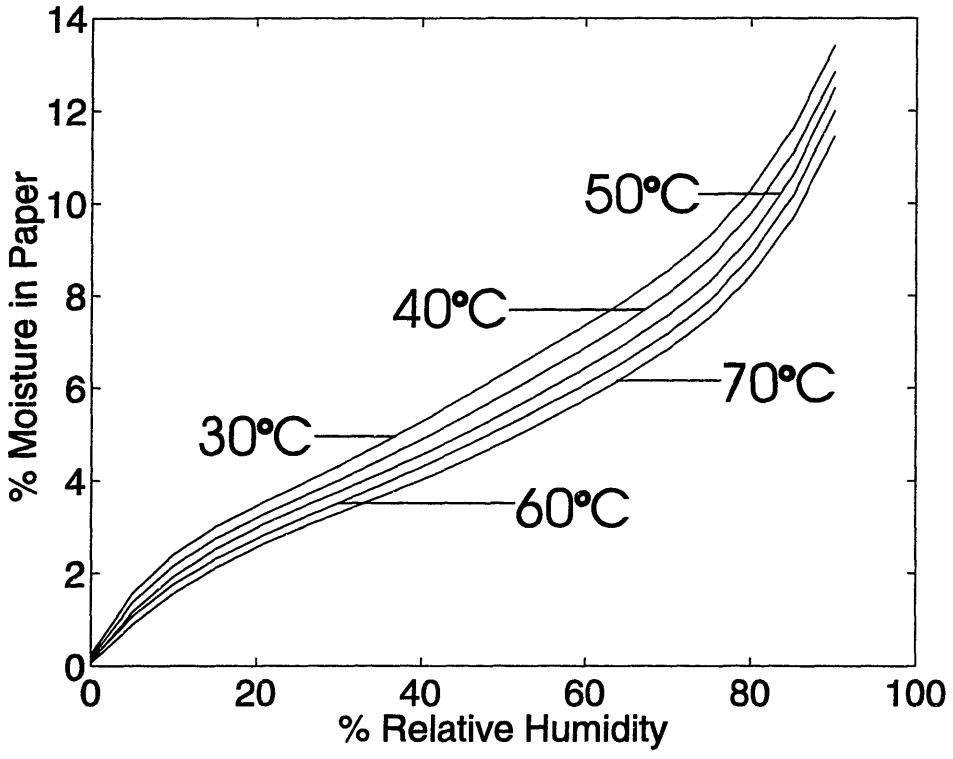

Figure C.1: Moisture in wood pulp as a function of ambient relative humidity curves reconstructed from the 6-th order polynomial fit to Jeffries' [22] data.

Appendix D

Data Processing Code

D.1 fick.m

```
function C=fick(C1,D,hour)

%Function fick plot the spatial profile of moisture for constant
%diffusion coefficient D and boundary condition C1 at 2-hour interval
%for a total of time of "hour" using Fick's second law of diffusion.

C0=0;
x=0:10^(-5):1.5*10^(-3);
xx=1.5*10^(-3):-10^(-5):0;
l=1.5*10^(-3);
n=0:20;

for t=2*3600:2*3600:hour*3600

for k=1:length(x)
a=(-1).^n./(2*n+1);
b=exp(-D*10^(-12)*(2*n+1).^2*pi^2*t/4/l^2);
c=cos((2*n+1)*pi*x(k)/2/l);
intermediate=a.*b.*c;
C(k)=C0+(C1-C0)*(1-4/pi*sum(intermediate));
end

a=plot(xx*1000,C,'-.');
hold on
end
```

D.2 diffimpl.m

```
function Csim= DiffImpl(D0,k,Ea,T,CompHours,C1,l)
        % This function plots the spatial profile of diffusion process
% with diffusion coefficient a function of concentration and temperature.
% D0 is actual D0*10^12,Ea is actual Ea/1000. T is in C, CompHours
% is in hours, each hour that want to be ploted are stored in column for
% each temperature, C1 is in percent, l is m.
% Implicit Method


%time steps in an hour
TimeSteps=400;
XSteps=150;

q=0;

for n=1:length(T)
dt=max(CompHours(:,n))*3600/TimeSteps;
ll=2*l(n);
x=0:ll/XSteps:ll;
dx=ll/XSteps;
b=dt/dx^2;

%Boundary Condition
C(1)=C1(n);
C(XSteps+1)=C1(n);
%Initial Condition
C(2:XSteps)=0;
Cp=C;
m=XSteps-1;
dimen=2:m-1;
for o=1:length(CompHours(:,n))-1
for t=CompHours(o,n)*3600:dt:CompHours(o+1,n)*3600
         D=D0*1e-12*exp(k*C+Ea*1000*(1/298-1/(273+T(n))));
 Z=D/k;
         Diag1=(-b*D(2:XSteps))';
 Diag2=(1+2*D(2:XSteps)*b)';
 Diag3=(-b*D(2:XSteps))';
 A=spdiags([Diag1 Diag2 Diag3],-1:1,m,m);
 B(1)=b*D(1)*C(1)+C(2)+b*(Z(3)-C(3)*D(3)-2*Z(2)+2*C(2)*D(2)...
+Z(1)-C(1)*D(1));
 B(dimen)=C(dimen+1)+b*(Z(dimen+2)-C(dimen+2).*D(dimen+2)-...
  2*Z(dimen+1)+2*C(dimen+1).*D(dimen+1)+Z(dimen)-C(dimen).*D(dimen));
 B(m)=b*D(1)*C(1)+C(XSteps)+b*(Z(1)-C(1)*D(1)-2*Z(XSteps)...
   +2*C(XSteps)*D(XSteps)+Z(m)-C(m)*D(m));
 Cp(2:XSteps)=A\B';
         C=Cp;
      end
plot(x*1000,C,'r')
hold on
Csim_intermediate(o)=C(XSteps/2+1);
```

```
   end
set(gca,'FontSize',20)
xlabel('Pressboard thickness, mm','FontSize',20);
ylabel('Moisture concentration, %','FontSize',20);
axis([0 1.5 0 C1(n)])

Csim(q+1:q+length(CompHours(:,n))-1)=Csim_intermediate;
q=length(Csim);
end
```

D.3 LsqImpl.m

```
          function diff = LsqImpl(D,CompHours,C1,Cexp,T,l)
          % This function is called by leastsq.
          % D is a vector which contains the coefficients of the
          % equation.  For finding the parameters for the D for all temperature data.
  % Use implicit method
  % Y. Du 6/22/98
D0=D(1);
k=D(2);
Ea=D(3);


%time steps in an hour
TimeSteps=60;
dt=3600/TimeSteps;
XSteps=100;

q=0;

for n=1:length(T)
ll=2*l(n);
dx=ll/XSteps;
b=dt/dx^2;

%Boundary Condition
C(1)=C1(n);
C(XSteps+1)=C1(n);
%Initial Condition
C(2:XSteps)=0;
Cp=C;
m=XSteps-1;
dimen=2:m-1;
for o=1:length(CompHours(:,n))-1
for t=CompHours(o,n)*3600:dt:CompHours(o+1,n)*3600
         D=D0*1e-12*exp(k*C+Ea*1000*(1/298-1/(273+T(n))));
 Z=D/k;
         Diag1=(-b*D(2:XSteps))';
 Diag2=(1+2*D(2:XSteps)*b)';
 Diag3=(-b*D(2:XSteps))';
 A=spdiags([Diag1 Diag2 Diag3],-1:1,m,m);
 B(1)=b*D(1)*C(1)+C(2)+b*(Z(3)-C(3)*D(3)-2*Z(2)+2*C(2)*D(2)...
+Z(1)-C(1)*D(1));
 B(dimen)=C(dimen+1)+b*(Z(dimen+2)-C(dimen+2).*D(dimen+2)-...
  2*Z(dimen+1)+2*C(dimen+1).*D(dimen+1)+Z(dimen)-C(dimen).*D(dimen));
 B(m)=b*D(1)*C(1)+C(XSteps)+b*(Z(1)-C(1)*D(1)-2*Z(XSteps)...
   +2*C(XSteps)*D(XSteps)+Z(m)-C(m)*D(m));
 Cp(2:XSteps)=A\B';
         C=Cp;
      end
Csim_Intermediate(o)=C(XSteps/2+1);
```

```
end
leng=length(CompHours(:,n));
Csim(q+1:q+leng-1)=Csim_Intermediate;
q=length(Csim);
end

        diff = Csim- Cexp;
```

D.4 Process.m

```
%Process.m processs the data from newsys97/newint5(30C),8(50C),9(60C),...
% 10(70C),11(40C) for diffusion coefficient
% using the new algorithm of implicit method

Cexp= [ 0.7343, 4.9731, 7.0233,...
0.3198, 1.5261, 3.9067,...
0.3610    1.1857    2.9841 ...
0.2940    1.2938    2.8914 ...
0.5087    1.1251    1.7721]
CompHours=[0       0    0   0    0;
       4.1697  10.3467  6.7314  5.1719   4.6603 ;
       11.2903 24.0158  13.8311 11.9792  9.9106;
       17.2122 44.5989 25.9631 22.3219  17.7275];
T=[30 40 50 60 70];
l=[1e-3 1.5e-3 1.5e-3 1.5e-3 1.5e-3];
C1=[7.8372 4.7156 3.3823 2.9424 1.8712];

%Using Least Square Fit to find D
Opt(1)=0;
Opt(2)=1e-8;
Opt(3)=1e-8;
Opt(4)=1e-8;

tic
Dini=[0.5 0.5 7];
D=leastsq('LsqImpl',Dini,Opt,[],CompHours,C1,Cexp,T,l);
toc
```

D.5 ngpimpvc.m

```
function ngpimpVc(DatFileName,filebegin,fileend,ttl,fno,Num,CL1mm, CL2mm,CL5mm,
VoltageBoostOrNot)

% Function ngpimpVc plots  raw data of all frequency
% data in a multi-frequency measurement in one figure using the
% time in the Head, given the frequency started at 10^fmax, ended
% at 10^fmin and the relative humidity using the new interface box.
% Data collected using Code NA*SIN1C.e
% It also computes C12 and G12.
% VoltageBoostOrNot=0, means 1 volt excitation
% VoltageBoostOrNot=1, means 10 volts boost

% Data aquisition by D.E. Schlicker
% Data process by Y. Du
% 11/11/97

% open data file

%no. of data in one measurement (between each time header
dno=2;
col=0;
fileno=fileend-filebegin+1;

for file=filebegin:fileend
file
    if (fileno==1) DatID=fopen(DatFileName,'rt');
else if(file<=9)  DatID = fopen([DatFileName '00' num2str(file) '.gpd'],'rt');
     else if(file<=99) DatID= fopen([DatFileName '0' num2str(file) '.gpd'],'rt');
else DatID=fopen([DatFileName '1' num2str(file) '.gpd'],'rt');
     end
    end
    if (DatID == -1)
disp(' ');
error('Error Opening Data File!');
    end;
    for k=1:Num*3*fno
Head(:,k+col) = fscanf(DatID,'[GH,%f,%i,%i,%i,%i,%i,%i]',7);
Data(:,col*dno+(k-1)*dno+1:col*dno+(k-1)*dno+dno)=fscanf(DatID,'[GD,%i,%f,%f,%f,%f,%i]',[6,dno]);
    end

    fclose(DatID);
    [row col]=size(Head);
    end
end
col=col/fno;

dno=dno*fno;

for k=1:fno
Gain1(k,:)=Data(3,k*2-1+dno*2:dno*3:col*dno-1);
```

```
Gain25(k,:)=Data(3,k*2-1+dno:dno*3:col*dno-1);
Gain5(k,:)=Data(3,k*2-1:dno*3:col*dno-1);

Offset1(k,:)=Data(5,k*2-1+dno*2:dno*3:col*dno-1);
Offset25(k,:)=Data(5,k*2-1+dno:dno*3:col*dno-1);
Offset5(k,:)=Data(5,k*2-1:dno*3:col*dno-1);
Amp1(k,:)=Data(6,k*2-1+dno*2:dno*3:col*dno-1);
Amp25(k,:)=Data(6,k*2-1+dno:dno*3:col*dno-1);
Amp5(k,:)=Data(6,k*2-1:dno*3:col*dno-1);

Phase1(k,:)=Data(4,k*2-1+dno*2:dno*3:col*dno-1);
Phase1(k,:)=Phase1(k,:)+360*(Phase1(k,:)<0)*(VoltageBoostOrNot==0);
Phase25(k,:)=Data(4,k*2-1+dno:dno*3:col*dno-1);
Phase25(k,:)=Phase25(k,:)+360*(Phase25(k,:)<0)*(VoltageBoostOrNot==0);
Phase5(k,:)=Data(4,k*2-1:dno*3:col*dno-1);
Phase5(k,:)=Phase5(k,:)+360*(Phase5(k,:)<0)*(VoltageBoostOrNot==0);

%RH for oil
RH(k,:)=(Data(5,k*4:dno*3:col*dno)-1)/4*100-2.575;

Freq(k,:)=10.^(Data(2,k*2-1+dno*2:dno*3:col*dno-1));
end


%Determine the relative time

T1=Head(3,1)*30*24+Head(4,1)*24+Head(5,1)+Head(6,1)/60+Head(7,1)/3600;
T22=T1;
for k=1:col/3
kk=k*3*fno-8;
T2=Head(3,kk)*30*24+Head(4,kk)*24+Head(5,kk)+Head(6,kk)/60+Head(7,kk)/3600;
time(k)=T2-T1;
end


%Impedance calculation
Gr1mm = 10.^(Gain1./20);
Fi1mm = Phase1*pi/180;

Gr25mm = 10.^(Gain25./20);
Fi25mm = Phase25*pi/180;

Gr5mm = 10.^(Gain5./20);
Fi5mm = Phase5*pi/180;

% Recalculate into real and imaginary parts of gain
Gre1 = Gr1mm.*(cos(Fi1mm));
Gim1 = Gr1mm.*(sin(Fi1mm));
cGain1=Gre1+j*Gim1;


Gre2 = Gr25mm.*(cos(Fi25mm));
```

```
Gim2 = Gr25mm.*(sin(Fi25mm));
cGain25=Gre2+j*Gim2;

Gre5 = Gr5mm.*(cos(Fi5mm));
Gim5 = Gr5mm.*(sin(Fi5mm));
cGain5=Gre5+j*Gim5;

for k=1:fno

Omega = Freq (k,1)*2*pi;
Y12m1(k,:)=(-1)^((VoltageBoostOrNot==0))*cGain1(k,:)*j*Omega*CL1mm/(1+9*VoltageBoostOrNot);
GG12m1(k,:)=real(Y12m1(k,:));
CC12m1(k,:)=imag(Y12m1(k,:))/Omega;

Y12m25(k,:)=(-1)^((VoltageBoostOrNot==0))*cGain25(k,:)*j*Omega*CL2mm/(1+9*VoltageBoostOrNot);
GG12m25(k,:)=real(Y12m25(k,:));
CC12m25(k,:)=imag(Y12m25(k,:))/Omega;

Y12m5(k,:)=(-1)^((VoltageBoostOrNot==0))*cGain5(k,:)*j*Omega*CL5mm/(1+9*VoltageBoostOrNot);
GG12m5(k,:)=real(Y12m5(k,:));
CC12m5(k,:)=imag(Y12m5(k,:))/Omega;
end

for k=1:fno
figure('PaperPosition',[0.25 0.75 8 9.5])
subplot(3,2,1), plot(time, Gain1(k,:))
xlabel('Time(hours)')
ylabel('Gain of 1.0mm (dB)')
ax=axis;
axis([0 max(time) ax(3) ax(4)]);

subplot(3,2,2), plot(time, Phase1(k,:))
xlabel('Time(hours)')
ylabel('Phase of 1.0mm (deg)')
ax=axis;
axis([0 max(time) ax(3) ax(4)]);


subplot(3,2,3) ,plot(time, Gain25(k,:))
xlabel('Time(hours)')
ylabel('Gain of 2.5mm (dB)')
ax=axis;
axis([0 max(time) ax(3) ax(4)]);

subplot(3,2,4) ,plot(time, Phase25(k,:))
xlabel('Time(hours)')
ylabel('Phase of 2.5mm (deg)')
ax=axis;
axis([0 max(time) ax(3) ax(4)]);

subplot(3,2,5), plot(time, Gain5(k,:))
xlabel('Time(hours)')
```

```
ylabel('Gain of 5.0mm (dB)')
ax=axis;
axis([0 max(time) ax(3) ax(4)]);

text('String',ttl,'Fontsize',18,'HorizontalAlignment','center','Units','Inches',...
'Position',[3 8.5])
text('String', [ num2str(Head(3)) '/' num2str(Head(4)) '/' num2str(Head(2)) ' ' ...
num2str(Head(5)) ':' num2str(Head(6)) ],'Fontsize',10,'HorizontalAlignment',...
'left','Units','Inches','Position',[5 8.2] )
text('String',  ['f= ' num2str(Freq(k)) ''] ,'Fontsize',10,...
'HorizontalAlignment','left','Units','Inches','Position',[5 8.05] )
text('String', ['File:' DatFileName ],'Fontsize',10,'HorizontalAlignment','left',...
'Units','Inches','Position',[5 7.9] )

subplot(3,2,6), plot(time, Phase5(k,:))
xlabel('Time(hours)')
ylabel('Phase of 5.0mm (deg)')
ax=axis;
axis([0 max(time) ax(3) ax(4)]);

%************************************* Plot Impedance
figure('PaperPosition',[0.25 0.75 8 9.5])
subplot(3,2,1), plot(time, CC12m1(k,:))
xlabel('Time(hours)')
ylabel('C12 of 1.0mm (pF)')
ax=axis;
axis([0 max(time) ax(3) ax(4)]);

subplot(3,2,2), plot(time, GG12m1(k,:))
xlabel('Time(hours)')
ylabel('G12 of 1.0mm (pS)')
ax=axis;
axis([0 max(time) ax(3) ax(4)]);


subplot(3,2,3) ,plot(time, CC12m25(k,:))
xlabel('Time(hours)')
ylabel('C12 of 2.5mm (pF)')
ax=axis;
axis([0 max(time) ax(3) ax(4)]);

subplot(3,2,4) ,plot(time, GG12m25(k,:))
xlabel('Time(hours)')
ylabel('G12 of 2.5mm (pS)')
ax=axis;
axis([0 max(time) ax(3) ax(4)]);

subplot(3,2,5), plot(time, CC12m5(k,:))
xlabel('Time(hours)')
ylabel('C12 of 5.0mm (pF)')
ax=axis;
axis([0 max(time) ax(3) ax(4)]);
```

```
text('String',ttl,'Fontsize',18,'HorizontalAlignment','center','Units','Inches',...
'Position',[3 8.5])
text('String', [ num2str(Head(3)) '/' num2str(Head(4)) '/' num2str(Head(2)) ' ' ...
num2str(Head(5)) ':' num2str(Head(6)) ],'Fontsize',10,'HorizontalAlignment',...
'left','Units','Inches','Position',[5 8.2] )
text('String',  ['f= ' num2str(Freq(k)) ''] ,'Fontsize',10,...
'HorizontalAlignment','left','Units','Inches','Position',[5 8.05] )
text('String', ['File:' DatFileName ],'Fontsize',10,'HorizontalAlignment','left',...
'Units','Inches','Position',[5 7.9] )

subplot(3,2,6), plot(time, GG12m5(k,:))
xlabel('Time(hours)')
ylabel('G12 of 5.0mm (pS)')
ax=axis;
axis([0 max(time) ax(3) ax(4)]);
end



figure
plot(time,RH(1,:))
ax=axis;
axis([0 max(time) ax(3) ax(4)])
xlabel('Time (hours)')
ylabel('%')
ax=axis;
if ((ax(4)-ax(3))<3) ax(4)=ceil((ax(4)-ax(3))/2+ax(3)+2);
ax(3)=floor((ax(4)-ax(3))/2+ax(3)-2);
elseif (max(RH(k,:))-min(RH(k,:))>10)
ax(4)=ceil(max(RH(k,:)));
ax(3)=floor(min(RH(k,:)));
end
axis([0 max(time) ax(3) ax(4)]);
text('String','','Fontsize',18,'HorizontalAlignment','center','Units','Inches',...
'Position',[3 6.5])
text('String', [ num2str(Head(3)) '/' num2str(Head(4)) '/' num2str(Head(2)) ' ' ...
num2str(Head(5)) ':' num2str(Head(6)) ],'Fontsize',10,'HorizontalAlignment',...
'left','Units','Inches','Position',[5 5.8] )
text('String', ['File:' DatFileName ],'Fontsize',10,'HorizontalAlignment','left',...
'Units','Inches','Position',[5 5.5] )
```

D.6 jeffplot.m

```
%Function Jeff calculates the moisture concentration at the boundary of the
%pressboard by ambient Relative Humidy rh at temperature T using Jeffries' data.
% 4/28/98 Yanqing Du

x=0:5:90;

for T=30:10:70
if T==70
y = 1.62524996E-10*x.^6 - 3.32186925E-08*x.^5 + 2.24735555E-06*x.^4 ...
 - 2.71010293E-05*x.^3 - 2.77977314E-03*x.^2 + 1.77626234E-01*x + 7.44186563E-02;

elseif T==60
y = 7.43804707E-11*x.^6 - 7.52865191E-09*x.^5 - 5.71293970E-07*x.^4 ...
+1.17310767E-04*x.^3-6.23002235E-03*x.^2+2.13594361E-01*x+1.39785727E-01;

elseif T==50
y = 9.53191441E-11*x.^6 - 1.17550191E-08*x.^5 - 3.73975784E-07*x.^4 ...
+1.27313164E-04*x.^3-7.28507799E-03*x.^2+2.43161186E-01*x+1.04832578E-01;



elseif T==40
y = -3.87298823E-11*x.^6 + 2.52283515E-08*x.^5 - 4.29262362E-06*x.^4 ...
+3.24489057E-04*x.^3-1.19501173E-02*x.^2+2.90791470E-01*x+1.69545834E-01;

elseif T==30
y = -9.34686547E-11*x.^6 + 4.24466336E-08*x.^5 - 6.33958786E-06*x.^4 ...
+4.38315253E-04*x.^3-1.49296958E-02*x.^2+3.28286566E-01*x+2.41312699E-01;

end

plot(x,y)
hold on

end

set(gca,'FontSize',20)
xlabel('% Relative Humidity','FontSize',20);
ylabel(' % Moisture in Paper','FontSize',20);
axis([0  100 0 14])
```

Bibliography

[1] M. Zaretsky, *Parameter Estimation Using Microdielectrometry with Application to Transformer Monitoring.* PhD thesis, Department of Electrical Engineering and Computer Science, Massachusetts Institute of Technology, Cambridge, MA, Nov. 1987.

[2] P. A. von Guggenberg, *Application of Interdigital Dielectrometry to Moisture and Double Layer Measurements in Transformer Insulation.* PhD thesis, Department of Electrical Engineering and Computer Science, Massachusetts Institute of Technology, Cambridge, MA, June 1993.

[3] Y. K. Sheiretov, "Dielectrometry measurements of moisture dynamics in oil-impregnated pressboard," Master's thesis, Department of Electrical Engineering and Computer Science, Massachusetts Institute of Technology, Cambridge, MA, May 1994.

[4] M. C. Zaretsky, L. Mouayad, and J. R. Melcher, "Continuum properties from interdigital electrode dielectrometry," *IEEE Transactions on Electrical Insulation*, vol. 23, pp. 897–917, Dec. 1988.

[5] F. M. Clark, "Factors affecting the mechanical deterioration of cellulose insulation," *Transactions of Electrical Engineering*, vol. 61, pp. 742–749, Oct. 1942.

[6] J. Fabre and A. Pichon, "Deterioration processes and products of paper and oil. Application to transformers," in *Proceedings of the International Conference on Large High Voltage Electric Systems (CIGRÉ)*, (Paris, France), June 15–25, 1960. Paper No. 137.

[7] H. P. Moser, *Transformerboard.* St. Johnsbury, Vermont: Special print of Scientia Electrica, translated by EHV-Weidmann Lim., 1979.

[8] A. Morin, M. Zahn, and J. Melcher, "Fluid electrification measurements of transformer pressboard/oil insulation in a couette charger," *IEEE Transactions on Electrical Insulation*, vol. 26, pp. 870–901, Oct. 1991.

[9] A. Washabaugh, P. von Guggenberg, M. Zahn, and J. Melcher, "Temperature and moisture transient flow electrification measurements of transformer pressboard/oil

insulation using a Couette facility," in *Proceedings of The 3rd International Conference on Properties and Applications of Dielectric Materials*, vol. 2, (Tokyo, Japan), pp. 867–870, July 8–12, 1991.

[10] W. A. Fessler, W. J. McNutt, and T. O. Rouse, "Bubble formation in transformers," Tech. Rep. EL-5384, EPRI, Palo Alto, CA, Aug. 1987.

[11] B. Fallou, "Summary of work done at l.c.i.e. on the paper-oil complex," *internal report of Laboraroire centre des Industries electriques, France.*

[12] S. M. Islam, P. R. S. Jota, and M. Stace, "Detection of oil-paper equilbrium moisture content in power transformer using hybrid intelligent interpretation of polarisation spectrums from recovery voltrage measurements," in *IEEE International Symposium on Electrical Insulation*, (Arlington, Virginia), June 1998.

[13] P. Griffin and J. Christie, "Effects of water and benzotriazole on electrostatic charge generation in mineral oil/cellulose systems," in *Proceedings: Static Electrification in Power Transformers*, June 1993. Project 1499-99.

[14] T. O. Rouse, "Mineral insulating oil in transformers," *Electrical Insulation Magazine*, vol. 14, no. 3, pp. 6–16, 1998.

[15] G. Beer, G. Gasparini, F. Osimo, and F. Rossi, "Experimental data on the drying-out of insulation samples and test coil for transformers," in *Proceedings of the International Conference on Large High Voltage Electric Systems (CIGRÉ)*, vol. II, (Paris, France), June 8–18, 1966. Paper No. 135.

[16] T. V. Oommen, "Moisture equilibrium in paper-oil insulation systems," in *Proceedings of the 16th Electrical/Electronics Insulation Conference*, (Chicago, IL), pp. 162–166, Oct. 3–6, 1983.

[17] R. Kaufman, E. J. Shimanski, and K. W. McFaydynen, "Gas and moisture equilibrium in transformer oil," *Communication and Electronics*, pp. 312–318, July 1955.

[18] D. N. Ewart, "Laboratory and factory measurements of moisture in power transformers," tech. rep., Aug. 1960.

[19] E. Norris, "High-voltage power-transformer insulation," *Proceedings of The Institution of Electrical Engineers*, vol. 110, pp. 428–440, Feb. 1963.

[20] J. K. Nelson, "Electrical field distribution in transformer oil," *IEEE Electrical Insulation Magazine*, vol. 10, no. 3, pp. 16–28, 1994.

[21] A. G. Schlag, "The recovery voltage method for transformer diagnosis," *Tettex Instruments booklet.*

[22] R. Jeffries, "The sorption of water by cellulose and eight other textile polymers," *Journal of the Textile Institute Transactions*, vol. 51, no. 9, pp. 339–374, 1960.

[23] J. Reason, "Cost-effective transformer maintenance," *Electrical World*, pp. 17–30, Oct. 1997.

[24] Handbook of Chemistry and Physics, D-94, 46th Edition, the Chemical Rubber Co., Cleveland, Ohio, 1966.

[25] J. Piper, "Moisture equilibrium between gas space and fibrous materials in enclosed electric equipment," *Transactions of the American Institute of Electrical Engineers (AIEE)*, vol. 65, pp. 791–797, Dec. 1946.

[26] A. R. Urquhart and A. M. Williams, "The moisture relations of cotton, the effect of temperature on the absorption of water by soda-boiled cotton," *Journal, Textile Institute*, vol. 15, p. T559, Oct. 1924.

[27] S. M. Neale and W. A. Stringfellow, "The primary sorption of water by cotton," *Transactions, Faraday Society*, vol. 37, p. 525, 1941.

[28] C. C. Houtz and D. A. McLean, "Adsorption of water by papers at elevated temperatures," *Journal of Physical Chemistry*, vol. 43, pp. 309–321, 1939.

[29] L. M. Pidgeon and O. Maass, "The adsorption of water by wood," *Journal, American Chemical Society*, vol. 52, p. 1053, 1930.

[30] W. W. Guidi and H. P. Fullerton , "Mathematical methods for prediction of moisture take-up and removal in large power transformers," *Proceedings of IEEE Winter Power Meeting*, no. C-74, pp. 242–244, 1974.

[31] T. Oommen, "Moisture equilibrium charts for transformer insulation drying practice," *IEEE Transaction on Power Apparatus and Systems*, vol. PAS-103, pp. 3063–3067, Oct. 1984.

[32] S. Glasstone, *Textbook of Physical Chemistry*, ch. XIV. Cambridge, MA: D. Van Nostrand Co., 1946.

[33] T. V. Oommen, E. M. Petrie, and S. R. Lindgren, "Bubble generation in transformer windings under overload conditions," *Minutes of the Sixty-Two Annual International Conference of Doble Clients*, pp. 16–28, Mar. 1995.

[34] P. Griffin, C. Bruce, and J. Christie, "Comparison of water equilibrium in silicone and mineral oil transformers," in *Minutes of the Fifty-Fifth Annual International Conference of Doble Clients*, 1988. Paper No. 10-9.

[35] S. Foss, "Power transformer drying model," Tech. Rep. DS-002-87, Dynamic Systems, Pittsfield, MA, Oct. 1987. Prepared for General Electric Company, Large Transformer Operation, Pittsfield, MA, and Consolidated Edison Corporation, New York, NY.

[36] P. F. Ast, "Movement of moisture through a50p281 kraft paper (dry and oil-impregnated)," Tech. Rep. Test report HV-ER-66-41, General Electric, June 1966.

[37] E. K. Steele, "Moisture redistribution in simulated transformer paper-oil systems," Tech. Rep. Memo report MATL 70-37, General Electric, Nov. 1970.

[38] Shell Oil Company, One Shell Plaza, 900 Louisiana Street, Houston, Texas 77002, (800) 231-6950, *Shell Diala Oils.* Shell Lubricants Technical Bulletin SOC: 39-92.

[39] Y. Du, M. Zahn, A. V. Mamishev, , and D. E. Schlicker, "Moisture dynamic measurements of transformer board using a three-wavelength dielectrometry sensor," in *IEEE International Symposium on Electrical Insulation*, (Montreal, Quebec, Canada), pp. 53–56, June 1996.

[40] Y. Du, B. Lesieutre, and M. Zahn, "Dielectrometry measurements of effects of moisture and anti-static additive on transformer board," in *IEEE Conference on Electrical Insulation and Dielectric Phenomena*, (Minneapolis, MN), pp. 226–229, Oct. 1997.

[41] Y. K. Sheiretov and M. Zahn, "Dielectrometry measurements of moisture dynamics in oil-impregnated pressboard," *IEEE Transactions on Dielectrics and Electrical Insulation,*, vol. 2, pp. 329–335, June 1995.

[42] A. K. Jonscher, *Dielectric Relaxation in Solids.* Chelsea Dielectrics Press, London, 1983.

[43] B. Nettelblad, "Effect of moisture content on the dielectric properties of cellulose," in *Nordic Insulation Symposium NORD-IS 92*, June 1992.

[44] N. Altamirano, "Effects of moisture and temperature on dielectric spectroscopy of transformer pressboard," tech. rep., Dec. 1998.

[45] A. K. Jonscher, *Universal Relaxation Law.* Chelsea Dielectrics Press, London, 1996.

[46] R. M. Hill, L. A. Dissado, J. Pugh, M. G. Broadhurst, C. K. Chiang, and K. J. Wahlstrand, "The dielectric response of portulacaceae (jade) leaves over an extended frequency range," *Journal of Biological Physics*, vol. 14, no. 4, pp. 133–135, 1987.

[47] D. E. Schlicker, "Flow electrification of aged transformer oils," Master's thesis, Department of Electrical Engineering and Computer Science, Massachusetts Institute of Technology, Cambridge, MA, Sept. 1996.

[48] M. C. Zaretsky and J. R. Melcher, "Complex permittivity measurements of thin films using microdielectrometry," in *Conference on Electrical Insulation and Dielectric Phenomena*, (Claymont, DE), pp. 462–471, Nov. 1986.

[49] Y. K. Sheiretov and M. Zahn, "Dielectrometry measurements of moisture dynamics in oil-impregnated pressboard," in *IEEE International Conference on Properties and Applications of Dielectric Material*, (University of Queensland, Brisbane, Australia), pp. 33–36, July 1994.

[50] A. V. Mamishev and M. Zahn, "Techniques for semi-empirical characterization of material and sensor properties in interdigital dielectrometry," in *IEEE International Symposium on Electrical Insulation*, (Montreal, Quebec, Canada), pp. 486–489, June 1996.

[51] A. V. Mamishev, Y. Du, and M. Zahn, "Measurement of dielectric property distributions using interdigital dielectrometry sensors," in *IEEE Conference on Electrical Insulation and Dielectric Phenomena*, (Virginia Beach, VA), pp. 309–312, Oct. 1995.

[52] A. Washabaugh, A. V. Mamishev, Y. Du, and M. Zahn, "Dielectric measurements of semi-insulating liquids and solids," in *International Conference on Conduction and Breakdown in Dielectric Liquids*, (Rome, Italy), pp. 381–384, July 1996.

[53] A. V. Mamishev, B. C. Lesieutre, and M. Zahn, "Parameter estimation using an interdigital dielectrometry sensor with finite-element software," in *IEEE Conference on Electrical Insulation and Dielectric Phenomena*, (Minneapolis, MN), pp. 234–237, Oct. 1997.

[54] D. R. Day, D. D. Shepard, and K. J. Craven, "A microdielectric analysis of moisture diffusion in thin epoxy/amine films of varying cure state and mix ratio," *Polymer Engineering and Science*, vol. 32, pp. 524–528, Apr. 1992.

[55] W. Press, S. Teukolsky, W. Vetterling, and B. Flannery, *Numerical Recipes in C: The Art of Scientific Computing*, ch. 19. Cambridge: Cambridge University Press, 1992.

[56] J. Quarshie, "Diffusion of moisture through cellulose insulation," Master's thesis, Department of Electrical and Electronic Engineering, University of Nottingham, Oct. 1977.